# STUDIES ON CONDUCTING POLYMER-BASED NANOCOMPOSITES FOR XANTHINE DETECTION

**Thesis submitted to the Delhi Technological University
for the award of the Degree of**

## DOCTOR OF PHILOSOPHY

**by**

## DEEKSHA

**(2K18/Ph.D./AC/01)**



**DEPARTMENT OF APPLIED CHEMISTRY,
DELHI TECHNOLOGICAL UNIVERSITY,
MAIN BAWANA ROAD,
DELHI-110042
INDIA**


**JULY 2024**

# DECLARATION

I state that this Ph.D thesis titled "**Studies on Conducting Polymer-based Nanocomposites for Xanthine Detection**" was completed by me for the award of the degree of **Doctor of Philosophy** under the supervision of Prof. D. Kumar, Department of Applied Chemistry, Delhi Technological University, New Delhi and Dr. C. M. Pandey, SGT University, Gurugram, Haryana, India.

The research work reported in this thesis is original and has not been submitted either in part or full to any university or institution for the award of any degree or diploma. This thesis does not contain any personal data, propriety graphs or other information, unless specifically acknowledged.

<div align="right">

**Ms. Deeksha**
(Research Scholar)
2k18/PhD/AC/01

</div>

# CERTIFICATE

This is to certify that the thesis entitled **"Studies on Conducting Polymer-based Nanocomposites for Xanthine Detection"** submitted by **Ms**. **Deeksha** to **Delhi Technological University, New Delhi, India** for the award of the degree of "**Doctor of Philosophy**" in **Chemistry** is a record of the work carried out by her. **Ms. Deeksha** has worked under my guidance and fulfilled the requirements for the submission of this thesis.

The results contained in the thesis have not been submitted either in part or full or in any other form to any university or institution for the award of any degree or diploma.

**Supervisor**                                         Co-Supervisor
**Prof. D. Kumar**                                **Dr. Chandra Mouli Pandey**
Department of Applied Chemistry          Assistant Professor,
Delhi Technological University               Department of Chemistry
Bawana Road, Delhi-110042                   SGT University, Gurugram
                                                            Haryana-122505

**Prof. Anil Kumar**
Head, Department of Applied Chemistry
Delhi Technological University
Bawana Road, Delhi-110042

*Dedicated*
*To*
*My Family*
*Mother-in -law,*
*Father-in-law &*
*Husband*

# ACKNOWLEDGMENTS

*This work will never be possible without God's grace and compassion, who continues to look after me despite my flaws. Completion of my thesis involved a lot of hardships and challenges. Fortunately, many people contributed to this endeavor. I take this opportunity to express my sincere gratitude to the people who have been instrumental in the successful completion of the thesis for their guidance, help and constant motivation.*

*First and foremost, I would like to extend my sincere gratitude to my research supervisor **Prof. D. Kumar**, Department of Applied Chemistry, Delhi Technological University, New Delhi for his dedicated help, advice, inspiration, encouragement and continuous support throughout my Ph.D. tenure. His enthusiasm, integral view on research and expedition for providing high-quality work have made a deep impression on me. During our course of interaction over the last five years, I have learned enormously from him and Iam glad to be associated with him in my research journey.*

*I wish to express my warm and sincere thanks to the Department of Applied Chemistry, Delhi Technological University for providing the research facilities during my Ph.D. tenure. Many thanks to all academic and administrative staff of Delhi Technological University for their kind co-operation and support. I am extremely grateful to **DST-INSPIRE** for the necessary financial support. I would like to convey my thanks to co-supervisor **Dr. C.M. Pandey** for his constant support and inspiration.*

*To my friends, and labmates (**Sonal Kunwar Rao, Dr. Ritika Kubba, Dr. Owais Jalil,***

# ABSTRACT

The research work reported in the thesis focuses on the development of biosensors that provide quantitative information about Xanthine (Xn) detection by utilizing a bio-component (enzyme) in direct contact with a transducer. Xn is a purine base, derived from guanine and adenosine-3-phosphate (ATP) which is catabolized in the animal muscle tissues, and its accumulation may result in several physiological disorders. Abnormal Xn levels in human plasma and urine may contribute to deregulation of Xn metabolism, and an excess amount of Xn acquired through spoiled food with an unpleasant smell could eventually lead to physiological problems such as gout, xanthinuria, hyperuricemia, and preeclampsia. Therefore, Xn not only acts as a biomarker for the above diseases but also acts as an indicator for fish and meat spoilage and freshness determination.

The analytical methods commonly used for Xn determination are based on spectrophotometric and chromatographic techniques which contain limitations such as long time for sample preparation, requiring skilled personnel to operate highly specialized equipment, impossibility of onsite detection, complex sample pre-treatment, etc. To overcome the limitations of existing techniques, we require a new method that is authentic, possesses a low detection limit, and is cost-effective, rapid and easy to use.

Biosensors are analytical devices having biological sensing elements that are attached to a transducer and produce an electronic signal. The electrochemical-based biosensors have become increasingly popular for detecting Xn due to their on-site

convenience, low-cost instrumentation, excellent selectivity, and rapid analysis. Their sensitivity significantly depends on the efficiency of enzyme immobilization and the electron transfer rate between the enzyme and electrode surface. To address these critical factors, researchers have explored various transducers in their studies.

In recent years, conducting polymers (CPs) have been widely used as a supporting material for fabricating effective transducers. CPs contain π-electron backbone responsible for their unusual electronic properties such as electrical conductivity, low energy optical transitions, low ionization potential and high electron affinity. CPs-based biosensors are cost-effective, easy to fabricate and offer a direct electrical readout for the detection of biological analytes with high sensitivity and selectivity. Various CPs such as polypyrrole, polythiophene, polyaniline, etc. have been widely used in biosensor fabrication. Apart from the merits, pure CPs have a few shortcomings like low sensitivity and poor selectivity. Nanomaterials-based CPs nanocomposites overcome these issues. Nanomaterials have their characteristics like high conductivity, large surface area, biocompatibility and excellent catalytic activity. Metal oxides ($CuO$, $TiO_2$, $MnO_2$, $ZnO$), graphene, carbon nanotube, etc. are some widely used nanomaterials. The incorporation of these nanomaterials effectively enhances the effective specific surface area, density, and catalytic power of nanocomposite. CP nanocomposites increase electron transfer in an electrochemical reaction which further improves the sensitivity and selectivity of the biosensor.

Consequently, my research employs a variety of electrochemical biosensors to detect xanthine selectively. These biosensors demonstrated the electrical, structural, morphological, compositional, and electrochemical properties of conducting polymers

and their nanocomposites with $TiO_2$, as well as their application potential in biosensing. Fish freshness indication can now be detected using a highly sensitive label-free electrochemical biosensor. The nanocomposite, which exhibits outstanding electrochemical characteristics, and selectivity, and functions as a suitable sensing layer, was created using a sustainable method.

# CONTENTS

# LIST OF FIGURES

# LIST OF TABLES

# ABBREVIATIONS

| | |
|---|---|
| PANI | Polyaniline |
| Xn | Xanthine |
| XOs | Xanthine Oxidase |
| CV | Cyclic Voltammetry |
| CP | Conducting Polymer |
| DPV | Differential Pulse Voltammetry |
| EDAX | Energy Dispersive X-ray Spectroscopy |
| PBS | Phosphate Buffer Saline |
| ITO | Indium Tin Oxide |
| EPD | Electrophoretic Deposition |
| XRD | X-Ray Diffraction |
| FT-IR | Fourier Transforms Infrared |
| TEM | Transmission Electron Microscopy |
| SEM | Scanning Electron Microscopy |
| RSD | Relative Standard Deviation |
| LOD | Limit of Detection |
| NBT | Nitro Blue Tetrazolium |
| CE | Capillary Electrophoresis |
| NPs | Nanoparticles |
| XDH | Xanthine Dehydrogenase |
| Au | Gold |
| GCE | Glassy Carbon Electrode |
| MWCNT | Multiwalled Carbon Nanotubes |
| ICPs | Intrinsically Conducting Polymers |
| CPE | Carbon Paste Electrode |

# CHAPTER 1

# INTRODUCTION & LITERATURE REVIEW

## 1.1 Xanthine

Recently, there has been a substantial rise in demand for a valuable and beneficial dietary option, and this has created an urgent need to detect its freshness. In this regard, xanthine (Xn) is a suspect for spoilage of fish freshness [1]. Xn is a by-product of nucleotide degradation, and its concentration increases with storage, which causes a bitter taste in fish meat.

A heterocyclic molecule having the empirical formula $C_5H_4N_4O_2$, xanthine (3,7-dihydro-purine-2,6-dione) is present in the majority of biological tissues, bodily fluids, and other living things. Purine bases, also known as Xn, are heterocyclic aromatic nitrogen-containing compounds that are used to build ATPs, DNA, and RNA. Several purines include adenine, guanine, hypoxanthine (Hx), caffeine, theobromine, and isoguanine [2]. The majority of nutrition- and health-related studies have shown that foods high in purines, such as fish, meat, and several minerals, raise uric acid levels in the blood. Elevated uric acid levels can lead to hyperuricemia, a prevalent factor in conditions such as gout, diabetes, cerebral ischemia, non-alcoholic fatty liver disease, and cardiovascular diseases. Low-purine foods are a great dietary choice to lower your risk of contracting these conditions [3]. Detecting Xn as an indicator, draws significant attention to determining the freshness and shelf life of fish and meat.

## 1.2 Xanthine Metabolism

Purines are the important parts of cellular energy systems (such as NAD and ATP), and play a role in signaling (such as GTP, AMP, and GMP), along with pyrimidines, contribute to the generation of DNA and RNA.

The synthesis of purines and pyrimidines is also possible from scratch or by recycling them through a regular catabolism salvage process . Uric acid is the final by-product of the full metabolism of purines [4]. The reported data shows that the main catabolic pathway for metabolism in plants is shown in **Fig.1.1.**

According to some reports, theobromine and 7-methylxanthine are necessary for the biosynthetic process that produces caffeine. [5, 6].
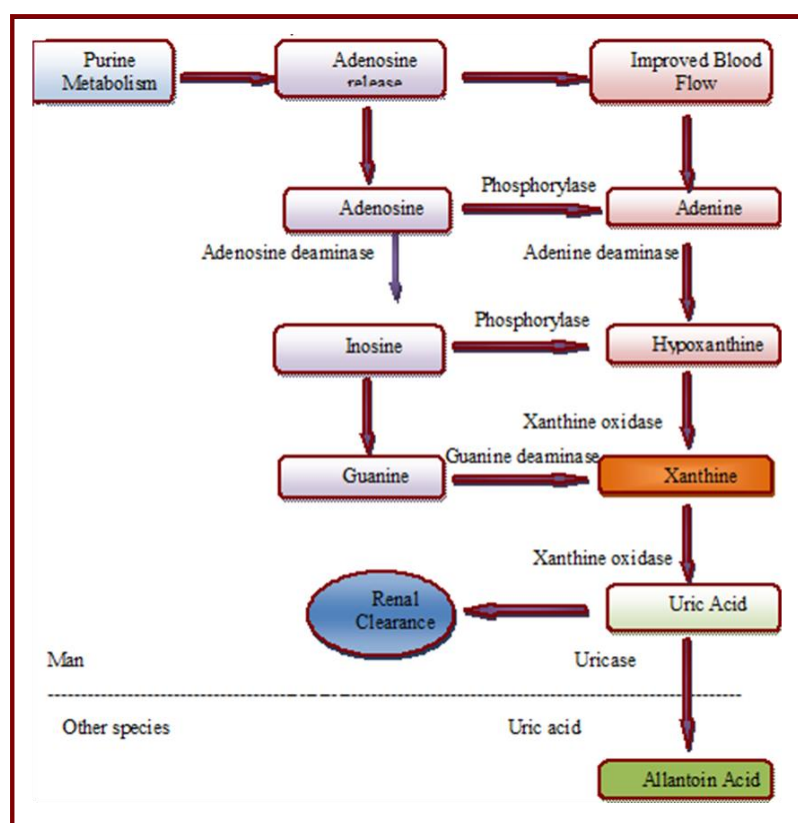


caffeine → theophylline → 3-methylxanthine → xanthine → uric acid → allantoin → allantoic acid → glyoxylic acid + urea → $NH_3$ + $CO_2$

**Fig.1.1:** Xanthine metabolism

According to Suzuki and Waller [7], the caffeine degradation process in coffee and tea also produces Xn. Several investigations using *Coffee arabica* have shown that labelled Xn is initially converted to uric acid, then allantoin, allantoic acid, urea + glyoxylic acid, $CO_2$, and ammonium [8].

## 1.3 Degradation in Xanthine

Purine produced by the metabolism of food and endogenous nucleic acid is finally converted in the human body to uric acid via xanthine oxidase (XOs). The weak acid, uric acid (5.8 pKa), found in an extracellular fluid compartment, is dispersed as sodium urate and eliminated from the plasma through glomerular filtration [9]. This filtered uric acid (90%) is reabsorbed from the proximal renal tubules, contributing to total clearance through an ATPase-dependent mechanism. Reactive oxygen species are produced by xanthine oxidoreductase or XOs. The conversion of Hx to Xn, followed by the conversion of xanthine to uric acid, is catalyzed by it. In several animals, including humans, this enzyme is crucial for the catabolism of purines.

The major portion of liver protein contains xanthine dehydrogenase (XDH) activity, albeit it can be converted to XOs through irreversible proteolytic modification or reversible sulfhydryl oxidation. Various physical and chemical approaches have been used to assess the freshness of fish, including sensory evaluation, microbiological procedures,assays of trimethylamine and total volatile basic nitrogen. The freshness index (or "K value"), which is a measure of the proportionate quantity of nucleotides produced by the adenosine triphosphate (ATP) degradative route, is regarded to be the most precise and useful indication among these methods. After death, the autolytic

mechanism described below naturally breaks down ATP in fish muscles to produce Hx and Xn:

$$ATP \longrightarrow ADP \longrightarrow AMP \longrightarrow IMP \longrightarrow HxR \longrightarrow Hx \longrightarrow Xn$$

HxR = inosine, Hx = hypoxanthine , Xn = xanthine , ADP = Adenosine diphosphate

However, after 24 h of death, the values of ATP and ADP rapidly fall and become inconsequential in some fish species. Additionally, there is a considerable decrease in (adenosine monophosphate) AMP concentration, which is now less than 1μmol/g. In contrast to these processes, (inosine monophosphate) IMP increases 5 to 25 h after death before declining when Hx and Xn concentrations rise correspondingly.

## 1.4 Clinical significance of Xanthine in fish meat

Xn serves as a pivotal metabolite in the breakdown of ATP molecules within fish meat, with its concentration steadily increasing during storage [3]. Given that the presence of Xn in fish meat is a reliable indicator of its freshness, the enzymatic conversion of Xn by XOs holds substantial significance [10]. It can go through cell membranes and build up in extracellular fluids. Numerous clinical disorders can be identified by the amount of Xn in body fluids [11]. The levels of Xn in body fluids serve as critical indicators for various medical conditions. Moreover, assessing the concentration of Xn in serum or urine samples provides essential insights, particularly regarding metabolic disorders such as arrhythmia, xanthinuria, and renal failure. Consequently, the determination of Xn holds considerable clinical and industrial significance, making it a valuable biomarker for detecting fish freshness [3, 10].

**1.4.1 Xanthinuria**

It is a rare hereditary condition caused by the deficiency of XOs, which increases the human body's xanthine level, leading to health issues like renal failure. There is no specific treatment for this disease. It is advised to the patients to avoid purine-rich foods and to maintain adequate fluid intake. There are two different types of xanthinuria :Type I is caused by mutations in the XDH gene, which regulates the activity of XOs directly, and Type II is brought on by a process failure that introduces sulfate into the active sites of XOs and aldehyde oxidase (converts allopurinol to oxypurinol). It has been suggested that XOs inhibition is a method for enhancing cardiovascular health [12]. Additionally, found in the corneal epithelium and endothelium, XOs and Xanthine oxidoreductase (XOR)  may contribute to oxidative eye damage.

**1.4.2 Gout**

A gout is a form of arthritis that may result from an excessive buildup of uric acid in the blood. Heavy consumption of foods rich in purines, high fructose intake, and impaired renal elimination can all contribute to elevated serum uric acid levels (hyperuricemia). Since urate crystallizes as calcium urate in the kidney, can cause one type of kidney stone, but owing to their radiolucency, these uric acid stones do not appear on an abdominal X-ray. Uric kidney stones can eventually develop in some gout patients. According to Nuki and Simkin [13], Gout can manifest at uric acid concentrations ranging from 6 mg/dL to as high as 9.5 mg/dL. Uric acid crystal buildup may be seen in the toe joints in **Fig.1.2**.

**Fig.1.2:** Uric acid crystal deposition

### 1.4.3 Lesch-Nyhan disorder

Elevated serum uric acid levels are related to Lesch-Nyhan syndrome, an extremely rare hereditary illness. This syndrome invokes, gouty symptoms such as spasticity, involuntary movement, and cognitive impairment are also present [14].

### 1.4.4 Cardiovascular diseases

Cardiovascular illness is frequently linked to high uric acid accumulation in serum, although it may have antioxidant properties. Elevated serum uric acid is linked to hypertension because of decreased renal blood flow and the ensuing increase in urate reabsorption. This persistent rise causes cardiovascular illnesses to progress [15].

### 1.4.5 XOs inhibitors

Any chemical that prevents XOs, an enzyme involved in purine metabolism, from functioning is known as an XOs inhibitor. Several drugs that inhibit XOs are recommended for treating gout and other related medical diseases and hyperuricemia in humans because they diminish uric acid synthesis. The use of XOs inhibitors in treating reperfusion injury is under investigation. There are two categories of XOs

inhibitors: purine analogues and others. Allopurinol, oxypurinol, and Tiso purine are examples of purine analogues **(Fig.1.3),** while Febuxostat and inositols (phytic acid and myo-inositol) are examples of others[16].
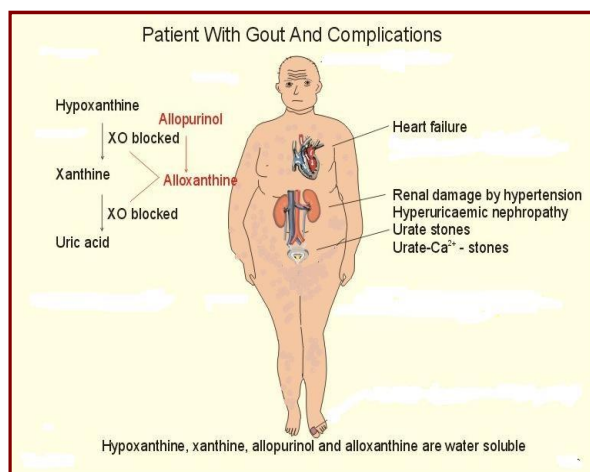


**Fig.1.3:** Allopurinol inhibitor of XOs

## 1.5 Conventional methods for Xn detection

The analytical methods commonly used for Xn determination are Enzymatic colorimetric, high-pressure liquid chromatographic (HPLC), capillary electrophoresis, column gas chromatography, fluorometric assay, and flow injection. The limitations of these techniques are time-consuming sample, equipment that needs to be operated by professional staff, inability to detect on-site, intricate sample pre-treatment, etc. Thus, the results of new analytical techniques are expected to be reusable, portable, reversible, sensitive, selective, simple, and able to monitor several parameters, simultaneously [17, 18]. The traditional analytical techniques for xanthine determination are briefly discussed below:

**1.5.1 UV spectrophotometric method**

This method is a simple, kinetic approach for evaluating serum activity that involves enzymatic coupling to XOs which also determines the rate of uric acid formation spectrophotometrically at 300 nm of absorbance. While uric acid does absorb at this wavelength at approximately 80% of its maximum absorbance at 293 nm, it's important to note that the disparity in molar absorbance between guanine and uric acid (8,400 at 300 nm vs. 9,000 at 293 nm) is comparable. The following reaction is the foundation of all enzymatic methods for determining xanthine:

$$Xn + O_2 + H_2O \xrightarrow{\text{XOs}} \text{Uric acid} + H_2O_2 \qquad (1.1)$$
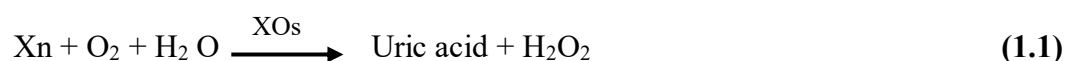
Although it is an extremely sensitive method, but also exhibits interference from hypoxanthine, has poor precision, poor efficiency, interference from background absorbance, and is expensive [19].

**1.5.2 Enzymatic colorimetric method**

An enzyme-driven colorimetric method developed by Berti et al. for quantifying phosphorus levels in bodily fluids and specifically in blood and urinary samples. In the presence of purine nucleoside phosphorylase, phosphate ions combine with inosine to produce hypoxanthine, which then oxidizes by XOs to uric acid while producing hydrogen peroxide. The chromogen (peroxidase/ 4-aminophenazone/ N-ethyl-N(-3methylpheny)-N'-acetyl ethylene diamine) has been used to determine the latter. The test had a linearity of up to 240 mg/L [20].

Aggarwal et al. established a microbial XOs generation assay employing xanthine as a substrate, with the resulting formazan generated through the reduction of nitro blue

tetrazolium (NBT) owing to hydrogen peroxide released during the xanthine-to-uric acid conversion. The basic concept was to test XOs producers by NBT using a colorimetric assay [21].

$$\text{Xanthine} + O_2 \xrightarrow{\text{XOs}} \text{Uric Acid} + \text{Hydrogen peroxide} \xrightarrow{\text{NBT}} \text{Formazan}$$

This method was easy to use and convenient, but it required expensive chemicals, took a long time, and interfered with several endogenous molecules.

### 1.5.3 Fluorimetric method

A quick and accurate fluorimetric test for inosine and adenosine involves the enzymatic conversion of one or both metabolites to Hx. The rates at which hydrogen peroxide appears following the addition of XOs are used to assess the rate of hypoxanthine formation. Inosine and adenosine were efficiently recovered from blood using uranyl acetate as a protein precipitant [22].

This technique is susceptible to environmental changes, such as pH and temperature variations, that impact the availability of electrons. Photochemical alterations can occur when UV light is employed for excitation.

### 1.5.4 Flow injection analysis (FIA)

The Flow Injection Analysis (FIA) depicted in **Fig.1.4** operates automatically. In this approach, the sample is initially introduced into an ongoing flow of carrier solution, where it subsequently merges with another continuously moving stream. And then, it reaches the detecting unit. By using FIA instead of manual injections, results are much more precise, which is advantageous over many analytical procedures. To measure XOs inhibitory activity and applying it to food samples, a flow injection

method has been devised. The examination of reagent concentrations and flow parameters was conducted to enhance the applicability of the FIA system, as cited in reference [23].

This method has various advantages, including inexpensive instrumentation costs, high sampling rates, and lower analysis costs when numerous samples need to be evaluated. However, reagents are always flowing and baseline monitoring is necessary, it is only limited to increased reagent consumption and waste.
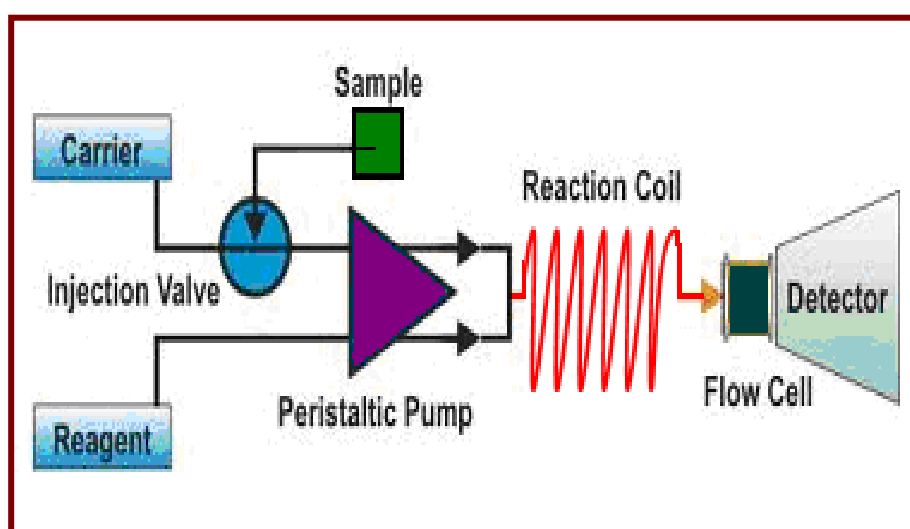


**Fig.1.4:** Schematic diagram of FIA

### 1.5.5 Gas chromatography (GC)

GC is an analytical method used to separate chemicals mostly based on their volatilities. GC offered quantitative and qualitative data for each compound present in a sample. Compounds that naturally exist as gases or that can be heated to evaporate into gaseous form travel through a GC column as gases. These compounds can be either solid or liquid (fixed phase) and gaseous (mobile phase) **(Fig.1.5)**. Compounds are capable of being separated into time and space due to the differential partitioning

into the stationary phase. The thermal degradation of barbiturates, phenolic alkaloids, and dimethylxanthines at the injection port resulted in the production of methyl derivatives, making them appropriate for quantitative gas chromatography.

Gas chromatography and isotope dilution-mass spectrometry (GC-IDMS) are two techniques that can be used to measure the amount of theophylline in human plasma or serum samples. Kress et al. utilized theobromine, paraxanthine, 1,3-dimethyl-7-(2-hydroxyethyl)xanthine and caffeine to investigate the effects of xanthine derivatives with similar substitutions, thereby confirming the method's specificity[24].
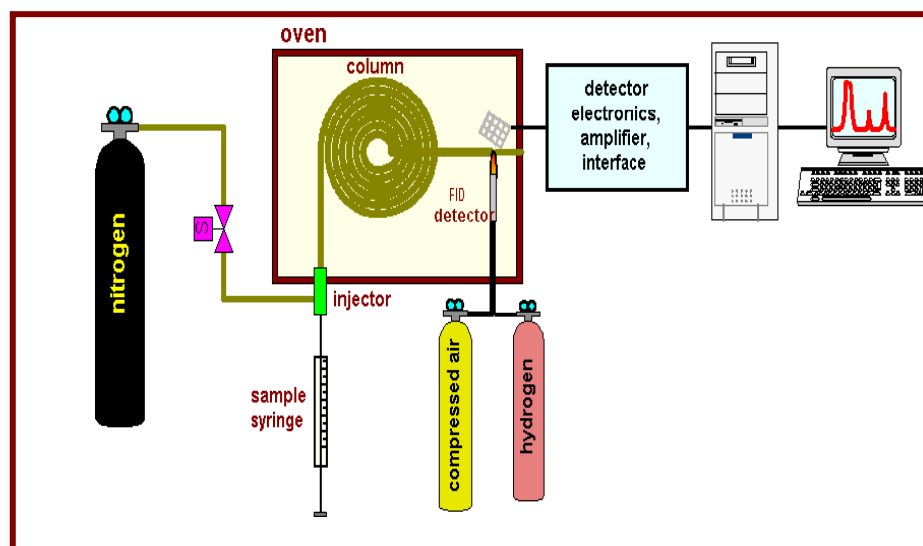


**Fig.1.5:** Determination of xanthine by GC

Although this method uses less expensive columns, faster run times, and much smaller sample sizes, it still demands expensive instrumentation, a smaller sample capacity, expert operators, and a greater signal-to-noise ratio.

## 1.5.6 High-performance liquid chromatography (HPLC)

In HPLC, diverse stationary phases, a pumping system to convey the analyte and mobile phases through the column, and a detector to determine the analyte's

characteristic retention time are utilized. **(Fig.1.6).** Integration of this system with UV/Vis spectroscopy, may provide additional information about the analyte.

A quick and selective reversed-phase HPLC method has been devised to measure hypoxanthine and xanthine in biological fluids simultaneously. This approach was used to examine how purine metabolism was affected by XOs deficiency or gout in patients. Erythrocyte samples from healthy individuals and patients taking allopurinol medication revealed plasma hypoxanthine values three to ten times higher than those reported [25].
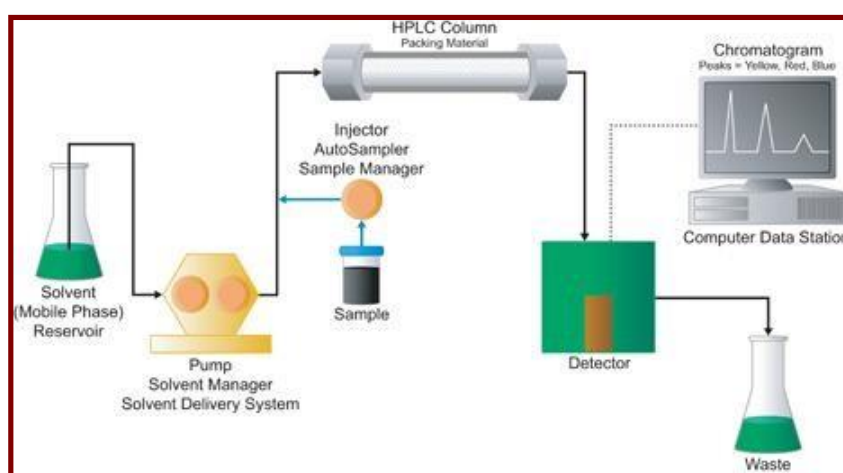


**Fig.1.6:** Determination of xanthine by HPLC

In 2002, Zhao *et al*. determined Hx and Xn in the Hippocampus by HPLC. Hx and Xn had linear ranges of 24.5-392.0 ng and 29.0-464.0 ng, respectively (R=0.99). Hx recovery was 100.73% on average, with the RSD of 1.31% (n=6) . In case of Xn, recovery was 100.54% on average, with the RSD of 1.14% (n=6). This method can be used to assess the hippocampal quality because of the accuracy of its results [26].

It offers advantages including high resolution, sensitivity, quicker run times, repeatability, accuracy, and automation, but also has some restrictions, such as the use of expensive equipment, laborious handling, and skill required.

**1.5.7 Capillary electrophoresis**

The term "capillary electrophoretic" (CE) is a group of interrelated separation methods in which fused-silica capillaries with a narrow bore are used to separate a wide variety of large and tiny molecules. Based on charge, size, and hydrophobicity variations, molecules are separated using strong electric fields. The CE technology can be divided into separation methods based on the capillary and electrolyte types used.

The CE method for measuring xanthine and hypoxanthine in urine has been developed to identify xanthinuria. The limit of quantization for the two compounds was 2µM/L, and the linearity was up to 200µM/L. The outcomes of the CE experiment were compared to those of the previously discussed HPLC approach. The results are comparable in terms of specificity, sensitivity, and repeatability, but CE was faster than HPLC. This technique results in low-cost, quick, and efficient analysis with minimal reagent usage but requires costly chemicals and expertise handling [27].

**1.6 Biosensors**

Biosensors have been seen as an attractive alternative to these conventional techniques. A biosensor refers to a self-contained integrated device with the capability to deliver precise quantitative or semi-quantitative analytical data. This is achieved using a biological recognition element (biochemical receptor) positioned in direct spatial contact with a transducer.[28].

Biosensors **(Fig.1.7)** mainly consist of two parts, i.e., the biological recognition element and the transducer. The biological recognition element can be a biomolecule

such as an enzyme, antibody, DNA/RNA, or whole cells/tissues, which binds to or reacts with the target analyte, initiating a biochemical reaction. The transducer converts the biochemical or biophysical signal resulting from the interaction between the biological recognition element and the target analyte into a measurable signal [29].
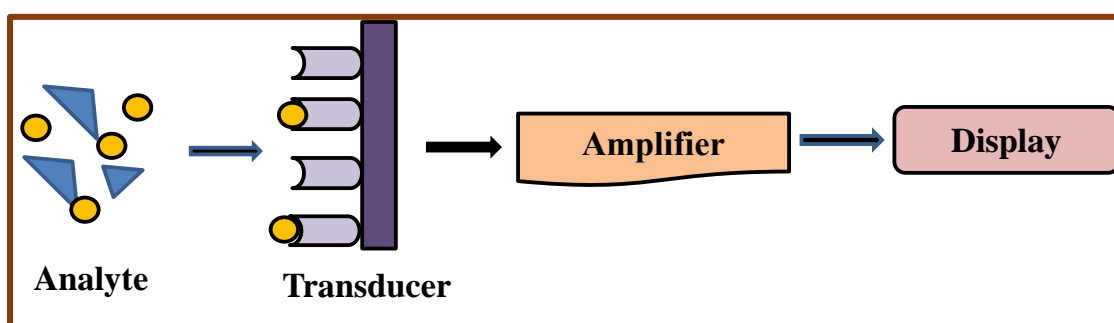


**Fig.1.7:** Schematic Diagram of Biosensor

Different types of transducers are used based on the sensing mechanism employed, such as optical, electrochemical, piezoelectric, or thermal transducers. Among all of these types of biosensors, electrochemical biosensors have been frequently used for biosensor applications.

**1.6.1 Electrochemical biosensors**

The fundamental principle of electrochemical biosensors is that various biochemical reactions either produce or utilize ions or electrons, resulting in changes in the electrical properties of the reaction solution. These changes can be detected to serve as measurement parameters [30]. The electrochemical reactions involved at the electrode interface are as follows:

$$\text{Xanthine} + O_2 + H_2O \xrightarrow{\text{XOs}} \text{Uric acid} + H_2O_2 \qquad \textbf{(1.2)}$$

14

$$H_2O_2 \longrightarrow 2H^+ + O_2 + 2e^- \tag{1.3}$$

$$2e^- \longrightarrow \text{Working electrode} \tag{1.4}$$
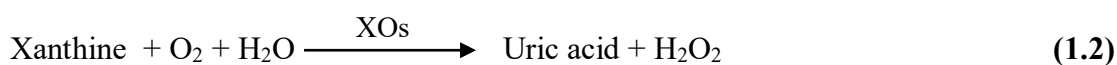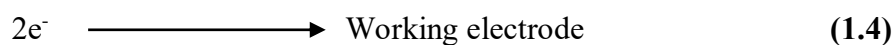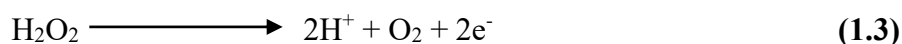
The electrochemical reactions taking place in the xanthine sensors when XDH is used are as follows:

XDH (ox) + Xanthine $\longrightarrow$ XDH (red) + Uric acid

Mediator (ox) + XDH (red) $\longrightarrow$ Mediator (red)+ XDH (ox) Mediator (red)

Mediator (ox) e $^{+\ -}$ $\longrightarrow$ Working electrode
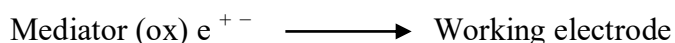
### 1.6.1.1 Amperometric biosensors

Amperometric biosensors are widely utilized and detect changes in current at a constant voltage resulting from a redox reaction. Their simplicity, ease of manufacture, and inexpensive cost, makes then popular among all types of biosensors. These sensors detect electron mobility, which can change the rate of mass transfer to the electrode surface and hence produce signals [31]. The enzyme needs to be close to the transducer to reduce the diffusion path of the observable reaction product. Wang et al. [32] developed an amperometry biosensor to evaluate the freshness of chilled squid and gigantic yellow croaker by successfully immobilizing XOs on copper-based metal-organic (Cu-MOF) film. With a linear range of 0.01–10 μM, the suggested electrochemical biosensor for xanthine and hypoxanthine showed good sensitivity. It also has a low LOD for hypoxanthine and xanthine of 0.0023 and 0.0064 μM, respectively.

An amperometric Xn biosensor was proposed by Joon et al. [33] to assess the freshness of fish meat. The fabrication of the biosensor was made easier by the use of

xanthine oxidase nanoparticles (XOsNPs), which were mounted directly onto polycrystalline Au electrodes via covalent coupling. The newly created biosensor exhibited a limit of detection (LOD) of 0.01 µM and a linear range spanning from 0.01 to 1.0 µM.

### 1.6.1.2 Potentiometric biosensors

These measure changes in charge distribution that result in generating an electrical potential, measured in volts. For the detection of Xn in fish and meat samples, Khan et al. devised a matrix of glassy carbon electrodes with PEDOT:PSS functionalized with gold nanoparticles (GCE/PEDOT: PSS-AuNPs). The fabricated biosensor demonstrated a range of linearity from 0.05 to 10 µM and a limit of detection (LOD) of 0.03 µM [34]. In a study by Yazdanparast et al., XOs immobilized nano-bio composite of poly (L-aspartic acid) film and multi-walled carbon nanotubes (MWCNT) was used as a matrix. The biosensor successfully detects Xn in fish meat, showcasing an impressive limit of detection (LOD) as low as 0.35 nM. Furthermore, it encompasses a linear range from 1 to 4 nM, and is further extended from 5 to $50 \times 10^3$ nM [35]. Ion-selective electrodes (ISE) and ion-sensitive field effect transistors (ISFET) are the foundations of potentiometric biosensors. Ions accumulating at the ion-selective membrane interface may be responsible for the major output signal.

### 1.7 Xanthine biosensors

Xn-based biosensors are widely employed for the rapid determination of Xn levels in real samples. XOs is present abundantly in mammalian tissue and plays a critical role as an enzyme in purine metabolism. After the animal death, Xn, a byproduct of

adenine nucleotide breakdowns in animal tissues, increases its level and is therefore useful as a freshness indicator in the food industry [36].

XOs has been immobilized on various supports, including polypyrrole film [18], Nafion membrane [37], self-assembled phospholipids membrane [38], silk membrane [39], PVC membrane [40], silk fibroin membrane [41], theophylline coated nylon mesh [42, 43], and cellulose acetate membrane [44].

However, these support materials (films/membranes) have several drawbacks, such as poor stability, slow electron transmission, and brittle, non-conducting, non-elastic membranes with limited absorption capabilities. XOs plays a critical role in the xanthine biosensor, and its optimal effectiveness is realized when it is combined with an appropriate immobilization matrix. So, the immobilization matrix plays an important role in the fabrication of Xn-based biosensors to overcome above stated limitations.

## 1.8 Conducting Polymer

Recently, there has been a great deal of interest in synthesizing conducting polymers (CPs) and their nanocomposites with distinct features [45]. The utilization of different CPs in sensors and biosensors, enhances sensitivity, lowers detection limits, broadens the linear detection range, improves electron transport efficiency, and enhances overall stability. Incorporating innovative polymers with nanoparticles, offering unique electrical and catalytic properties, greatly promotes their efficient utilization in sensors and biosensors [46].

CPs are the combination of two properties, the mechanical strength of polymers and the ability to conduct electricity like metals. Hence, CPs find applications in a diverse array

of fields such as optoelectronics, energy storage systems, medical devices, and biosensors [47]. The biocompatibility, sensitivity, improved signal transmission, porosity, and mechanical flexibility of CPs make them a particularly promising material. The electrical structure of CPs is sensitive to modifications in the environment and conformation of polymer chains, such as those brought on by biological recognition.
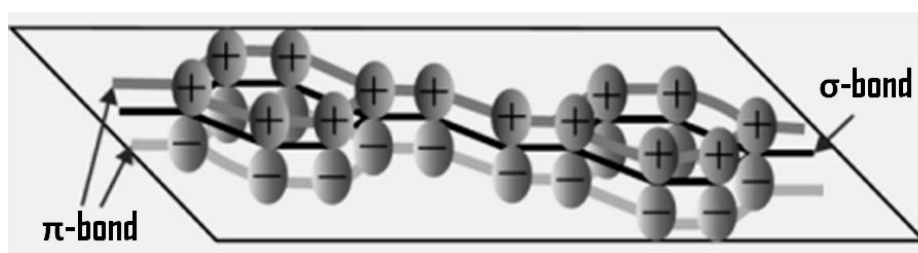


**Fig.1.8:** Conjugation in the conducting polymer

Doping/dedoping methods can also be utilized to modify the electrical and optoelectronic properties of CPs, reversibly. Another feature of CPs is that they have a dual conductivity mechanism. CPs are capable of carrying both electronic and ionic charges, which allows them to effectively transform an ionic signal into a solid-state electronic signal.

For recognition elements, CPs provide a variety of immobilization methods. Physical adsorption represents the fundamental technique for immobilization, wherein biomolecules adhere to the surface through weak interactions such as van der Waals forces, hydrogen bonding, or hydrophobic interactions [48, 49].

Covalent immobilization is also a successful approach for improving biosensors' stability, activity, binding effectiveness, sensitivity, and preventing molecular recognition element leaching [50] .
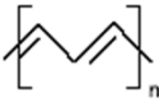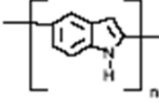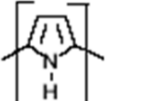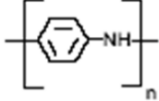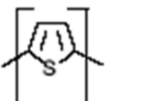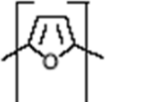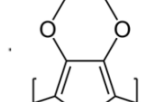
| Polymer | Structure | Polymer | Structure |
|---------|-----------|---------|-----------|
| Polyacetylene | | Polyindole | |
| Polypyrrole | | Polyaniline | |
| Polythiophene | | Polyazulene | |
| Polyfuran | | Poly (3,4-ethylenedioxythiophene) | |

**Fig.1.9:** Various types of conducting polymers

The stability in various environmental conditions, flexibility, and desirable electrochemical and electrochromic properties of conjugated polymers and copolymers distinguish them significantly from other conventional polymers [51]. Following is a list of some significant and well-studied conducting polymers, along with their chemical structure **(Fig.1.9).**

Biocompatible conjugated polymers have proven to be highly effective matrices for entrapping or immobilizing biomolecules, including enzymes, antigens, antibodies, and cells. Furthermore, CP provides various technological solutions for developing sensors, biosensors, and biofuel cells.

Additionally, flexible biosensors can be built using CPs' mechanical capabilities, which is essential for the development of wearable or in vivo devices [52]. For example: Dolmaci et al. invented an amperometric biosensor using pyrrole and polyvinyl sulphonate to immobilize XOs on the surface of a Pt electrode, for Hx detection in fish [61]. On the electrode surface at + 0.3 V, uric acid was released during an enzymatic reaction, and this acid was then oxidized to determine Xn. The discussed biosensor provided a simple and fast approach for determining Hx in fish meat, with a linear range of 0.0001 - 1mM and a LOD of 10 μM [18].

According to Khan et al. [53], Xn was measured on GCE modified with poly(3,4-ethylenedioxythiophene)/polystyrene sulfonate (PEDOT: PSS) polymer that included AuNPs. This biosensor possesses wide linearity ranges from 0.5 nM to 0.1μM, with a LOD of 30 nM. Even though Hx and uric acid were present as interferences, the sensor showed good outcomes in fish and meat samples.

Different conducting polymers have also been investigated as electrode materials for capacitors and rechargeable batteries. Even drug delivery techniques for neurotransmitters in the brain have recently used polymeric films and nanoparticles [54]. Devices like diodes and capacitors have been developed due to promising applications for conducting polymers in non-linear optics, electronics, and photonics. For example, Hitachi-Maxell uses polyaniline (PANI) to coat their 4 MB barium ferrite floppy disks with an anti-static layer [55].

In analytical chemistry, selectivity is crucial, particularly when dealing with low analyte concentrations and interfering compounds. Analysis tools have become more potent as a result of the development of highly selective and user-friendly sensors.

Developing diverse sensor types has a great deal of promise with CPs. However, CPs show significant variations in electrical conductivity in response to environmental changes in pH and redox potential.

CPs are copolymerized with a range of nanomaterials, including graphene, carbon, and metal nanoparticles (NPs), to fabricate nanocomposites. This strategy leverages the combined properties of each component, resulting in enhanced detection capabilities for both electrochemical and biosensing applications [56].

### 1.8.1 Nanomaterials

Nanomaterials are materials with unique characteristics and structures at the nanoscale, commonly ranging in size from 1 to 100 nm. Because of their small size, great surface area-to-volume ratio, and quantum effects, these materials exhibit new features and behaviours when compared to their bulk counterparts. Nanomaterials have been used in various industries, including electronics, medicine, energy, and materials science [57].

Nanostructured metal oxides are recognized for their exceptional capacity to accelerate electron transfer kinetics between the electrode and the active site of the specific enzyme. Nanomaterial-based biosensors provide a sensitive and dependable method for detecting xanthine, allowing for rapid and precise analysis in complicated biological samples. Nanomaterials with distinctive features such as high surface area, superior conductivity, and tunable optical qualities include nanoparticles (such as gold nanoparticles and quantum dots), nanowires, nanotubes, and graphene-based materials. These characteristics enable improved biomolecule immobilization and signal transduction. The incorporation of biomolecules into nanomaterials, such as

enzymes, antibodies, or aptamers, improves sensor selectivity and affinity for Xn molecules [58].

In the context of stability and catalytic reduction, Xn biosensors based on NPs have numerous advantages. The electrode is known for its ability to prevent interfering species from oxidizing. The unique attributes of nanoparticles, such as exceptional mechanical strength, oxygen ion conductivity, biocompatibility, and preservation of biological activities, have captivated the attention of numerous researchers [59]. Because NPs have an electroactive electrode surface, electron transport between the electrolyte medium and the electrode is improved. Large surface areas, excellent conductivity, and catalytic properties of metal NPs ($TiO_2$, ZnO, Au, Ag, Pt, and Cu etc.), make them an ideal carrier for encapsulating enzymes and active compounds to build efficient modified electrodes. Because of their superior biocompatibility and enzymatic activity preservation, AuNPs have been routinely employed to encapsulate enzymes [60].

Due to the amplification effects of nanomaterials and the high specificity of recognition elements, nanomaterial-based biosensors exhibit extraordinary sensitivity and selectivity. These biosensors are capable of detecting Xn concentrations over a wide dynamic range, allowing for exact quantification in complicated biological matrices [35, 61].

Thandavan et al. reported a biosensor that could determine the concentration of Xn in the 0.4 to 2.4 nM range using mediator-free iron oxide ($Fe_3O_4$) nanoparticles-based biosensor for Xn determination to indicate fish freshness. Due to the improved electron transfer channel offered by the $XOD/Fe_3O_4/Au$-modified electrode, the value of LOD was 0.4 nM with a 2s of response time [62].

Yazdanparast et al. [35] designed an enzyme-based ultrasensitive electrochemical biosensor for Xn detection utilizing a poly(L-aspartic acid)/MWCNT bio-nanocomposite to ensure meat's freshness. The MWCNT and poly(L-aspartic acid) layers were used to immobilize XOs on a GCE. The produced sensor showed linear ranges of 1-4 nM and 5 to $50 \times 10^3$ nM with a detection limit of $3.5 \times 10^{-4}$ μM, when it was employed to identify Xn in fish meat

### 1.8.2 CP-based Nanocomposites

Apart from their traditional use as electrical insulators, polymers have become increasingly popular as appropriate semiconductors or conductors in the last decade **(Fig.1.10)**. Conductive polymers, often referred to as intrinsically conducting polymers (ICPs), are a class of organic polymers characterized by their capability to conduct electricity. ICPs are now being coupled with graphene or metal-based matrices to create composites with exceptional conducting characteristics [63]. These nanocomposites have applications ranging from EMI shielding to Biosensors. With improved electrical and physical properties, lower prices and processability, these materials are quickly gaining interest in newer application areas. The unique nanostructured forms of conducting polymers, particularly with their increased surface area, are inexpensive, have a sufficiently high specific capacitance, and are environmentally friendly [64].

Conjugated polymers, synthesizable through both chemical and electrochemical means, allow for straightforward adjustment of a broad spectrum of properties. These properties encompass film thickness, conductivity, functionalization, utilization of various supporting electrolytes, and the capability to function as an electrochemical

transducer. One more benefit of using CPs is that they can deposit the material along with the enzyme in a single-step process. A new amperometric biosensor for Xn assessment was developed by immobilizing XOs on a carbon paste electrode (CPE) that was enhanced through modification with a hybrid nanocomposite film [65]. With a LOD of 0.1 µM, and a linear range of 0.2 to 36.0 µM, the developed biosensor successfully determines the freshness of fish meat.
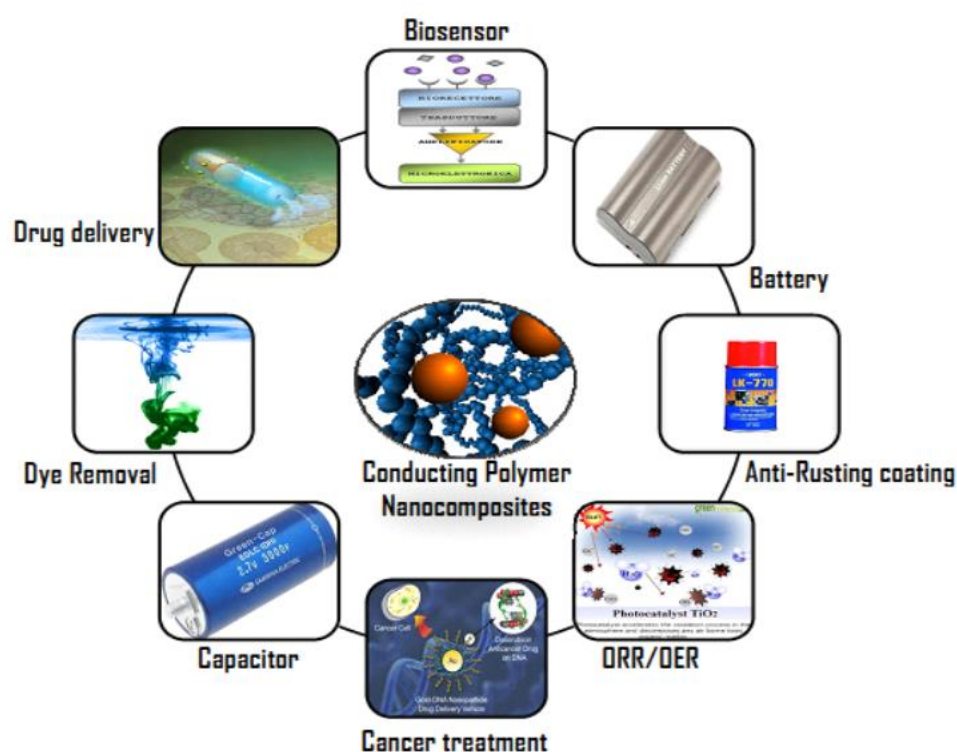


**Fig.1.10** Application of Conducting Polymer Nanocomposites

CP-modified nanomaterials show excellent physiochemical and electrical properties, cost-effectiveness and efficient electron transfer ability, high sensitivity and selectivity. They have improved functional and structural properties such as a high aspect ratio, increased mechanical strength, and electrical properties.

## 1.9 CP-based Nanocomposites for Xn Detection

Since the last decade, the application of various conducting polymer-based nanocomposite biosensors for hypoxanthine or xanthine detection has gained interest due to their superior physiochemical and electrical properties that can potentially be customizable. Some of them are Polypyrrole-polyvinyl sulphonate (PPy-PTS) films [66], polypyrrole-para-toluene-sulfonate (PPy-pTS) [67, 68], disposable amperometric biosensor with a screen-printed electrode, gold-nanoparticles with single-walled carbon nano-horn (GNPs/SWCNH), polymeric mediator/multi-walled carbon nanotubes (MWCNT) [69], reduced graphene oxide/iron oxide bio-nanocomposite interface [70] and polymerized 10-[4 *H*-dithieno (3,2-*b*: *2′,3′-d*) pyrrole-4-yl] decane-1-amine film etc [71]. Nevertheless, these biosensors have limitations, including slow electron transfer, limited stability, lack of reusability, fragility, and poor absorption capacity. These factors contribute to higher limits of detection and a constrained linear detection range. Therefore, it is crucial to implement a faster electron transfer system with a lower detection limit [72, 73].

Determining Xn is essential for clinical analysis and monitoring food quality. As a result, a sensitive enzymatic amperometric sensor based on CP nanocomposites is needed for xanthine detection. **Table 1** summarizes recent developments in the analytical performance of electrochemical biosensors for meat freshness detection.

**Table 1:** Recent developments in the analytical performance of electrochemical biosensors for meat freshness detection.

| Electrode Material | Enzyme | Analyte | Method | Sample | Linear Range | LOD | Ref. |
|---|---|---|---|---|---|---|---|
| $Fe_3O_4$ NP/Au | XOs | Xn | Amperometry | Fish | 0.4–2.4nM | 0.4 nm | [62] |

| | | | | | | | |
|---|---|---|---|---|---|---|---|
| ZnO-NPs/PPy/Pt | XOs | Xn | Amperometry | Fish | 0.8–40 μM | 0.8 μM | [74] |
| c-MWCNTs/PANI/Pt | XOs | Xn | Amperometry | Fish | 0.6–58 μM | 0.6μM | [75] |
| ZnO-NP/Chitosan/c-MWCNTs/PANI/Pt | XOs | Xn | Amperometry | Fish | 0.1-100 μM | 0.1 μM | [76] |
| Au-colloids/PPy/Pt | XOs | Xn | Amperometry | Fish, chicken, pork, beef | 0.4-100 μM | 0.4 μM | [77] |
| AgNPs/l-Cys/Au | XOs | Xn | Amperometry | Fish, chicken, pork, beef | 2 -16 μM | 0.15μM | [78] |
| Poly(GMA-co-VFc)/MWCNTs/PGE | XOs | Xn | Amperometry | Fish | 2–28μM, 28–46μM, 46–86μM | 0.12μM | [79] |
| Poly(GMA-co-VFc)/ REGOFe$_3$O$_4$/PGE | XOs | Xn | Amperometry | Fish | 2-36 μM | 0.17μM | [80] |
| DTP-alkyl-NH$_2$/PGE | XOs | Xn | Amperometry | Chicken | 0.3-25 μM | 0.074 μM | [81] |
| Chitosan/Ppy/Au-NPs/GCE | XOs | Xn | Amperometry | Fish, chicken, beef | 1-100 μM | 0.25μM | [82] |
| TiO$_2$/MWCNTs/Au | XOs | Xn | Amperometry | Fish | 0.5-500 μM | 0.5 μM | [83] |
| Poly(l-Asp)/MWCNTs/GCE | XOs | Xn | DPV | Fish | 0.001-0.004μM, 0.005–50.0μM | $3.5 \times 10^{-4}$ M | [35] |
| PEDOT:PSS/AuNPs/GCE | XOs | Xn | DPV | Fish, meat | 0.05-10 μM | $3.0 \times 10^{-8}$ M | [34] |
| Cu-MOF/GCE | XOs | Hx, Xn | DPV | Fish, squid | 0.01-10 μM | 0.0023 μM 0.0064 μM | [32] |
| GLAD-NiO | XOs | Xn | Conductometry | Fish | 0.1-5 μM | 37nm | [84] |
| Au/PEDOT/ fMWCNT/GCE | XOs | UA, Xn, Hx | Conductometry | Fish, meat | 0.1–800 μM 0.05–175 μM 0.1–150 μM | 199.3 nM 24.1 nM 90.5 nM | [85] |
| ZnIn$_2$S$_4$/UiO-66-NH$_2$/GCE | XOs | Hx Xn | Amperometry | Large yellow croaker | 0.3–40 μM 0.025–40 μM | 0.1 μM 0.0083 μM | [86] |
| EPPGE | Non-enzymatic | Hx Xn UA | Amperometry | Fish | 0.1-50 μM 0.1-50 μM 0.1-25 μM | 0.08 μM 0.06 | [87] |

| | | | | | | | |
|---|---|---|---|---|---|---|---|
| | | | | | | µM 0.03 µM | |
| NPs/Au | XOs | Xn | DPV | Fish, meat | 0.01-1.0 µM | 0.01 µM | [33] |
| AuNPs/c-MWCNT/SPCE | XOs | Xn | Amperometry | Fish Chicken meat | 2388.88µA/cm$^2$/nM | 1.14nM | [88] |
| Ag–ZnO NPs/PPy/PGE | XOs | Xn | CV | Sea bass fish | 0.06-0.6 µM | 0.07 µM | [89] |
| MFPP/FPP/PtNPs | XOs | Xn | Amperometry | Fish | 0.1-1.4mM | 48nM | [90] |
| SnO$_2$@CeO$_2$-Co | Non-enzymatic | Xn | DPV | Chicken | 25nM-55 µM | 58nM | [91] |
| rGO/Chitosan/Cr$_2$O$_3$/GCE | Non-enzymatic | DA, UA, Xn, Hx | Amperometry | Fish | 5-160 µM 10-500 µM 10-400 µM 2-300 µM | 0.65 µM 0.80 µM 1.20 µM 0.85 µM | [92] |
| Co(TMA)MOF/CNF | Non-enzymatic | Xn, UA | Amperometry | Fish | 25-700 µM | 96.2 nM 103.5 nM | [93] |
| Ag/AgCl(4BPGE) | Non-enzymatic | Hx, Xn, UA | Amperometry | Fish | 6-30 µM, 8-36 µM 3-21µM | 1.09 µM 0.40 µM 0.17 µM | [94] |

## 1.10 Objectives

The main objective of the proposed research work is to fabricate an electrochemical biosensor based on CP-based nanocomposites for Xn detection. To accomplish this goal, the following steps were taken:

➤ Synthesis, functionalization and characterization of CPs and their nanocomposites with various metal oxides ($TiO_2$, ZnO, CeO, and MgO)

➤ Deposition of nanostructured CP and its nanocomposites onto ITO electrode surface using electrophoretic /electrochemical deposition techniques.

➤ Immobilization of enzyme onto the fabricated electrode and characterization of the fabricated electrode using various spectroscopic and morphological techniques.

➤ Electrochemical response studies of Xn using the fabricated bioelectrode and studies on biosensors' specificity, reproducibility and shelf life.

➤ Validation of biosensors with real samples obtained from fish, mutton, chicken meat etc.

## 1.11 Thesis organization

In the present thesis, efforts have been made to fabricate an electrochemical fish freshness biosensor using immobilized xanthine oxidase (XOs) on CPs and its nanocomposites for quantitative estimation of Xanthine (Xn). **This thesis is ordered as follows:**

**Chapter 1** presents a descriptive literature review on Xn, its clinical significance, and various conventional techniques and highlights the detailed description of CPs and its nanocomposites-based biosensors for specific detection of Xn.

**Chapter 2** outlines the various experimental methods that have been used to characterize the CP-based electrodes and bioelectrodes that have been modified with nanocomposite materials. Efforts have been made to characterize the performance of the nanohybrid biosensor based on conjugated polymers (CPs) for Xn detection, along with a detailed discussion of the employed processes and techniques

**Chapter 3** details the development of an electrochemical enzymatic biosensor for Xn detection based on PANI@TiO$_2$ nanohybrid. The synthesized nanostructured PANI@TiO$_2$ nanohybrid proved to be an efficient conducting platform for biosensing due to its redox behaviour and the ability to mediate the reactive site and electrode surface via biomolecule. The developed XOs/PANI@TiO$_2$/ITO electrode exhibited enhanced electron transfer kinetics. Validation using a real sample from Rohu fish confirmed its ability to detect Xn in fish meat. The biosensor accurately detected micromolar levels of xanthine in the fish samples, providing a direct assessment of fish meat freshness.

In **Chapter 4**, the research findings of the fabrication of a stable binary nanocomposite, PoPD@g-C$_3$N$_4$, using a straightforward oxidative polymerization method, are presented and discussed. The synthesis of PoPD@g-C$_3$N$_4$ has been verified using a variety of spectroscopic and morphological approaches. An increase in electron transfer values for PoPD@g-C$_3$N$_4$ electrodes compared to bare PoPD and g-C$_3$N$_4$ makes it a promising material for immobilizing XOs. The PoPD@g-C$_3$N$_4$ nanocomposite-based biosensor, thus demonstrates to be a suitable platform for Xn monitoring.

**Chapter 5** describes the development of electrochemical biosensors based on g-$C_3N_4$@PoPD-$TiO_2$ nanocomposite. Different ratios of $TiO_2$ nanoparticles have been used to synthesize the g-$C_3N_4$@PoPD-$TiO_2$ nanocomposite. To create an ultrasensitive electrochemical immunosensor for Xn detection in fish meat, we electrophoretically deposited the g-$C_3N_4$@PoPD-$TiO_2$ nanocomposite onto an ITO-coated glass substrate. Electrochemical investigations indicate that the deposition of g-$C_3N_4$@PoPD-$TiO_2$ nanocomposite with 1% $TiO_2$ content offers an excellent charge transfer coefficient. The biosensor was highly stable and reproducible and has been validated to determine Xn in real fish samples.

The investigations on applications of CP-based nanocomposite biosensors for Xn detection are summarized in **Chapter 6**. This chapter also discusses the prospects and depth of CP-based nanocomposite for additional applications.

## References

1.  Kamil Reza, K., M.K. Singh, S.K. Yadav, J. Singh, V.V. Aggarwal, and B.D. Malhotra, *Quantum dots based platform for application to fish freshness biosensor.* Sensors and Actuators B: Chemical, 2013. **177**: p. 627-633.

2.  Sahyar, B.Y., M. Kaplan, M. Ozsoz, E.Selik, and S.Otles, *Electrochemical xanthine detection by enzymatic method based on Ag doped ZnO nanoparticles by using polypyrrole.* Bioelectrochemistry, 2019. **130**: p. 107327.

3.  Devi, R., S. Yadav, and C.S. Pundir, *Electrochemical detection of xanthine in fish meat by xanthine oxidase immobilized on carboxylated multiwalled carbon nanotubes/polyaniline composite film.* Biochemical Engineering Journal, 2011. **58-59**: p. 148-153.

4.  Moffatt, B.A. and H. Ashihara, *Purine and pyrimidine nucleotide synthesis and metabolism.* Arabidopsis Book, 2002. **1**: p. e0018.

5.  Silvarolla, M.B., P. Mazzafera, and L.C. Fazuoli, *A naturally decaffeinated arabica coffee.* Plant biochemistry, 2004. **429**(6994): p. 826-826.

6.  Yamaoka-Yano, D.M. and P. Mazzafera, *Catabolism of caffeine and purification of a xanthine oxidase responsible for methyluric acids production in Pseudomonas putida L.* Revista de microbiologia, 1999. **30**: p. 62-70.

7.  Suzuki, T., and G.R. Waller, *Biosynthesis and biodegradation of caffeine, theobromine, and theophylline in Coffea arabica L. fruits.* Journal of Agricultural and Food Chemistry, 1984. **32**(4): p. 845-848.

8.  Suzuki, T. and E. Takahashi, *Biosynthesis of caffeine by tea-leaf extracts. Enzymic formation of theobromine from 7-methylxanthine and of caffeine from theobromine.* Biochemical Journal, 1975. **146**(1): p. 87-96.

9.  Chen, C., J.M. Lü, and Q. Yao, *Hyperuricemia-Related Diseases and Xanthine Oxidoreductase (XOR) Inhibitors: An Overview.* Med Sci Monit, 2016. **22**: p. 2501-12.

10. Albelda, J.A.V.,  A. Uzunoglu, G.N.C. Santos, and L.A. Stanciu, *Graphene-titanium dioxide nanocomposite based hypoxanthine sensor for assessment of meat freshness.* Biosensors and Bioelectronics, 2017. **89**: p. 518-524.

11. Devi, R., S. Yadav, and C.S. Pundir, *Amperometric determination of xanthine in fish meat by zinc oxide nanoparticle/chitosan/multiwalled carbon nanotube/polyaniline composite film bound xanthine oxidase.* Analyst, 2012. **137**(3): p. 754-759.

12. Berry, C.E. and J.M. Hare, *Xanthine oxidoreductase and cardiovascular disease: molecular mechanisms and pathophysiological implications.* J Physiol, 2004. **555**(Pt 3): p. 589-606.

13. Nuki, G., and P.A. Simkin,  *A concise history of gout and hyperuricemia and their treatment.* Arthritis Research & Therapy, 2006. **8**(1): p. 1-5.

14. Jinnah, H.A., I.C.-Picot, R.J. Torres, J.E. Vesser, D.J. Schretlen, A. Verdu, L.E. Laróvere, C.J. Chen, A. Cossu, C.H. Wu, R. Sampat, S.J. Cheng, R.D. de Kremer, W. Nyhan, J.C. Harris, and S.G. Reich, *Attenuated variants of Lesch-Nyhan disease.* Brain, 2010. **133**(Pt 3): p. 671-89.

15. Grassi, D., L. Ferri, G. Desideri, P.D. Giosia, P. Cheli, R.D. Pinto, G. Properzi, and C. Ferri, *Chronic hyperuricemia, uric acid deposit and cardiovascular risk.* Curr Pharm Des, 2013. **19**(13): p. 2432-8.

16. Becker, M.A., H.R. Schumacher, R.L. Wortmann, P.A. MacDonald, D. Eustace, W.A. Palo, J. Streit, and N.J.-Ridge, *Febuxostat compared with allopurinol in patients with hyperuricemia and gout.* N Engl J Med, 2005. **353**(23): p. 2450-61.

17. Dolmaci, N., S.Çete, F. Arslan and A. Yaşar, *An amperometric biosensor for fish freshness detection from xanthine oxidase immobilized in polypyrrole-polyvinylsulphonate film.* Artificial Cells, Blood Substituts and Biotechnology, 2012. **40**(4): p. 275-9.

18. Dolmacı, N., S. Çete, F. Arslan and A. Yaşar,  *An amperometric biosensor for fish freshness detection from xanthine oxidase immobilized in polypyrrole-*

*polyvinylsulphonate film.* Artificial Cells, Blood Substitutes, and Biotechnology, 2012. **40**(4): p. 275-279.

19.    Yasmineh, W.G., *Simple ultraviolet spectrophotometric method for the determination of serum guanase activity.* Clinical Biochemistry, 1988. **21**(4): p. 239-243.

20.    Berti, G., P. Fossati, G. Tarenghi, C. Musitelli, and G.V. Melzi d'Eril, *Enzymatic Colorimetric Method for the Determination of Inorganic Phosphorus in Serum and Urine.* Clinical Chemistry and Laboratory Medicine, 1988. **26**(6): p. 399-404.

21.    Agarwal, A. and U. Banerjee, *Screening of Xanthine Oxidase Producing Microorganisms Using Nitroblue Tetrazolium Based Colometric Assay Method.* The Open Biotechnology Journal, 2009. **3**: p. 46-49.

22.    Helenius, M., S. Jalkanen, and G. Yegutkin, *Enzyme-coupled assays for simultaneous detection of nanomolar ATP, ADP, AMP, adenosine, inosine and pyrophosphate concentrations in extracellular fluids.* Biochimica et biophysica acta, 2012. **1823**: p. 1967-75.

23.    Buitrago, L.E., S. Marhenke, J. Lamle, P.M. Manns, and, A. Vogel, *Rapamycin prevents proliferation of hepatocytes independently of p21 and sustains apoptosis sensitivity during chronic liver damage*. in *HEPATOLOGY*. 2006. JOHN WILEY & SONS INC 111 RIVER ST, HOBOKEN, NJ 07030 USA.

24.    Kress, M., D. Meissner, P. Kaiser, R Hanke, and W.G. Wood, *The measurement of theophylline in human serum or plasma using gas chromatography and isotope dilution-mass spectrometry (GC-IDMS) taking other substituted xanthines into consideration.* Clinical laboratory, 2002. **48**: p. 535-40.

25.    Boulieu, R., C. Bory, P. Baltassat, and C. Gonnet, *High-performance liquid chromatographic determination of hypoxanthine and xanthine in biological fluids.* Journal of Chromatography B: Biomedical Sciences and Applications, 1982. **233**(1): p. 131-140.

26.  Zhao, X., X. Cui, L. Di, and W. Li, *Determination of hypoxanthine and xanthine in hippocampus by HPLC method.* Journal of Chinese Medicinal Materials, 2002. **25**(10): p. 716-7.

27.  Bory, C., C. Chanting, and R. Boulieu, *Comparison of capillary electrophoretic and liquid chromatographic determination of hypoxanthine and xanthine for the diagnosis of xanthinuria.* Journal of Chromatography A, 1996. **730**(1): p. 329-331.

28.  Xu, Z., X. Chen, and S. Dong, *Electrochemical biosensors based on advanced bioimmobilization matrices.* TrAC Trends in Analytical Chemistry, 2006. **25**(9): p. 899-908.

29.  Dzyadevych, S.V., V.N. Arkhypova, A.P. Soldatkin, A.V. El'skaya, C. Martelet, and N.J.-Renault, *Amperometric enzyme biosensors: Past, present and future.* IRBM, 2008. **29**(2): p. 171-180.

30.  Shanbhag, M.M., G. Manasa, R.J. Mascarenhas, K. Mondal, and N.P. Shetti, *Fundamentals of bio-electrochemical sensing.* Chemical Engineering Journal Advances, 2023. **16**: p. 100516.

31.  Baranwal, J., B. Barse, G. Gatto, G. Broncova, and A. Kumar, *Electrochemical Sensors and Their Applications: A Review.* Chemosensors, 2022. **10**, DOI: 10.3390/chemosensors10090363.

32.  Wang, Z., B. Ma, C. Shen, O.-M. Lai, C.-P. Tan, and L.-Z Cheong, *Electrochemical biosensing of chilled seafood freshness by xanthine oxidase immobilized on copper-based metal–organic framework nanofiber film.* Food Analytical Methods, 2019. **12**: p. 1715-1724.

33.  Joon, A., J. Ahlawat, V. Aggarwal, R. Jaiwal, and C.S. Pudir, *An improved amperometric determination of xanthine with xanthine oxidase nanoparticles for testing of fish meat freshness.* Sensing and Bio-Sensing Research, 2021. **33**: p. 100437.

34. Khan, M., M. Ahommed, and M. Daizy, *Detection of xanthine in food samples with an electrochemical biosensor based on PEDOT: PSS and functionalized gold nanoparticles.*RSC Advances, 2020. **10**(59): p. 36147-36154.

35. Yazdanparast, S., A. Benvidi, S. Abbasi, and M. Rezaeinasab, *Enzyme-based ultrasensitive electrochemical biosensor using poly (l-aspartic acid)/MWCNT bio-nanocomposite for xanthine detection: A meat freshness marker.* Microchemical Journal, 2019. **149**: p. 104000.

36. Mao, L. and K. Yamamoto, *Amperometric on-line sensor for continuous measurement of hypoxanthine based on osmium-polyvinylpyridine gel polymer and xanthine oxidase bienzyme modified glassy carbon electrode.* Analytica Chimica Acta, 2000. **415**(1): p. 143-150.

37. Nakatani, H.S., L.V. dos Santos, C.P. Pelegrine, S.T.M. Gomes, M. Matushita, N.E.de Souza, and J.V. Visentainer, *Biosensor based on xanthine oxidase for monitoring hypoxanthine in fish meat.* American Journal of Biochemistry and Biotechnology, 2005. **1**(2): p. 85-89.

38. Rehák, M., M. Šnejdárková, and M. Otto, *Application of biotin-streptavidin technology in developing a xanthine biosensor based on a self-assembled phospholipid membrane.* Biosensors and Bioelectronics, 1994. **9**(4-5): p. 337-341.

39. Mao, L., F. Xu, Q. Xu, and L. Jin, *Miniaturized amperometric biosensor based on xanthine oxidase for monitoring hypoxanthine in cell culture media.* Analytical Biochemistry, 2001. **292**(1): p. 94-101.

40. Pundir, C., R. Devi, J. Narang, S. Singh, J. Nehra, and S. Chaudhry, *Fabrication of an amperometric xanthine biosensor based on polyvinylchloride membrane.* Journal of Food Biochemistry, 2012. **36**(1): p. 21-27.

41. Mulchandani, A., J.H.T. Luong, and K.B. Male, *Development and application of a biosensor for hypoxanthine in fish extract.* Analytica Chimica Acta, 1989. **221**: p. 215-222.

42. Moody, G.J., G.S. Sanghera, and J.D.R. Thomas, *Chemically immobilised bi-enzyme electrodes in the redox mediated mode for the flow injection analysis of glucose and hypoxanthine.* Analyst, 1987. **112**(1): p. 65-70.

43. Mao, L., J. Jin, L. Song, K. Yamamoto, and L. Jin, *Electrochemical Microsensor for In Vivo Measurements of Oxygen Based on Nafion and Methylviologen Modified Carbon Fiber Microelectrode.* Electroanalysis, 1999. **11**(7): p. 499-504.

44. Basu, A.K., P. Chattopadhyay, UR. Choudhury, and R. Chakraborty, *Development of an amperometric hypoxanthine biosensor for determination of hypoxanthine in fish and meat tissue.* 2005.

45. Spychalska, K., D. Zając, S. Baluta, K. Halicka, and J. Cabaj, *Functional polymers structures for (Bio) sensing application—A review.* Polymers, 2020. **12**(5): p. 1154.

46. Lee, K.M., K.H. Kim, H. Yoon, and H. Kim, *Chemical design of functional polymer structures for biosensors: From nanoscale to macroscale.* Polymers, 2018. **10**(5): p. 551.

47. Ramanaviciene, A. and I. Plikusiene, *Polymers in Sensor and Biosensor Design.* Polymers (Basel), 2021. **13**(6).

48. Aydemir, N., J. Malmström, and J. Travas-Sejdic, *Conducting polymer based electrochemical biosensors.* Physical Chemistry Chemical Physics, 2016. **18**(12): p. 8264-8277.

49. Prajapati, D.G. and B. Kandasubramanian, *Progress in the Development of Intrinsically Conducting Polymer Composites as Biosensors.* 2019. **220**(10): p. 1800561.

50. Uzun, S.D., N.A. Unlu, M. Sendur, F.E. Kanik, S. Timur, and L. Toppare, *A novel promising biomolecule immobilization matrix: Synthesis of functional benzimidazole containing conducting polymer and its biosensor applications.* Colloids and Surfaces B: Biointerfaces, 2013. **112**: p. 74-80.

51. Celiesiute, R., A. Ramanaviciene, M. Gicevicius, and A. Ramanavicius, *Electrochromic sensors based on conducting polymers, metal oxides, and coordination complexes.* Critical Reviews in Analytical Chemistry, 2019. **49**(3): p. 195-208.

52. German, N., A. Ramanaviciene, and A.J.P. Ramanavicius, *Formation and electrochemical evaluation of polyaniline and polypyrrole nanocomposites based on glucose oxidase and gold nanostructures.* Polymers, 2020. **12**(12): p. 3026.

53. Khan, M.Z.H., M.S. Ahommed, and M. Daizy, *Detection of xanthine in food samples with an electrochemical biosensor based on PEDOT:PSS and functionalized gold nanoparticles.* RSC Advances, 2020. **10**(59): p. 36147-36154.

54. Zinger, B. and L.L. Miller, *Timed release of chemicals from polypyrrole films.* Journal of the American Chemical Society, 1984. **106**(22): p. 6861-6863.

55. Friend, M., M. Reising, and L. Cook, *Co-Teaching: An Overview of the Past, a Glimpse at the Present, and Considerations for the Future.* Preventing School Failure: Alternative Education for Children and Youth, 1993. **37**(4): p. 6-10.

56. Kaur, G., A. Kaur, and H. Kaur, *Review on nanomaterials/conducting polymer based nanocomposites for the development of biosensors and electrochemical sensors.* Polymer-Plastics Technology and Materials, 2020. **60**: p. 1-18.

57. Laurent, S., D. Forge, M. Port, A. Roch, C. Robic, L.V. Elst, and R.N. Muller, *Magnetic iron oxide nanoparticles: synthesis, stabilization, vectorization, physicochemical characterizations, and biological applications.* Chemical reviews, 2008. **108**(6): p. 2064-2110.

58. Barrak, H., T. Saied, P. Chevallier, G. Laroche, A. M'nif, and, A.H. Hamzaoui, *Synthesis, characterization, and functionalization of ZnO nanoparticles by N-(trimethoxysilylpropyl) ethylenediamine triacetic acid (TMSEDTA): Investigation of the interactions between Phloroglucinol and ZnO@ TMSEDTA.* Arabian Journal of Chemistry, 2019. **12**(8): p. 4340-4347.

59. Kumar, S.G. and L.G. Devi, *Review on modified TiO₂ photocatalysis under UV/visible light: selected results and related mechanisms on interfacial charge carrier transfer dynamics.* The Journal of physical chemistry A, 2011. **115**(46): p. 13211-13241.

60. Naseem, T. and T. Durrani, *The role of some important metal oxide nanoparticles for wastewater and antibacterial applications: A review.* Environmental Chemistry and Ecotoxicology, 2021. **3**: p. 59-75.

61. Cavalcante, F.T.T., IR de A. Falcão, JE da S. Souza, TG Rocha, IG de Sousa, ALG. Cavalcante, A.L.B. de Oliveira, M.C.M. de Sousa, and J.C.S. dos Santos, *Designing of Nanomaterials-Based Enzymatic Biosensors: Synthesis, Properties, and Applications.* Electrochem, 2021. **2**(1): p. 149-184.

62. Thandavan, K., S. Gandhi, S. Seturamam, J.B.B. Rayappan, and U.M. Krishnan, *Development of electrochemical biosensor with nano-interface for xanthine sensing–A novel approach for fish freshness estimation.* Food Chemistry, 2013. **139**(1-4): p. 963-969.

63. Sharma, S., P. Sudhakara, A.A.B Omran, J. Singh, and R.A. IIyas, *Recent Trends and Developments in Conducting Polymer Nanocomposites for Multifunctional Applications.* Polymers (Basel), 2021. **13**(17).

64. Omana, L., A. Chandran, R.E. John, R. Wilson, K.C. George, N.V. Unnikrishnan, S.S. Varghese, G. George, S.M. Simon, and I. Paul, *Recent Advances in Polymer Nanocomposites for Electromagnetic Interference Shielding: A Review.* ACS Omega, 2022. **7**(30): p. 25921-25947.

65. Sadeghi, S., E. Fooladi, and M. Malekaneh, *A nanocomposite/crude extract enzyme-based xanthine biosensor.* Analytical biochemistry, 2014. **464**: p. 51-59.

66. Dervisevic, M., E. Dervisevic, E. Çevik, and M. Şenel, *Novel electrochemical xanthine biosensor based on chitosan–polypyrrole–gold nanoparticles hybrid bio-nanocomposite platform.* Journal of Food and Drug Analysis, 2017. **25**(3): p. 510-519.

67. Dolmacı, N., S. Çete, F. Arslan and A. Yaşar, *An amperometric biosensor for fish freshness detection from xanthine oxidase immobilized in polypyrrole-polyvinylsulphonate film.* Artificial Cells, Blood Substitutes, and Biotechnology, 2012. **40**(4): p. 275-279.

68. Erol, E., E. Yildirim, and S. Cete, *Construction of biosensor for hypoxanthine determination by immobilization of xanthine oxidase and uricase in polypyrrole-paratoluenesulfonate film.* Journal of Solid State Electrochemistry, 2020. **24**(7): p. 1695-1707.

69. Dervisevic, M., E. Custiuc, E. Çevik, and M. Şenel, *Construction of novel xanthine biosensor by using polymeric mediator/MWCNT nanocomposite layer for fish freshness detection.* Food Chemistry, 2015. **181**: p. 277-283.

70. Dervisevic, M., E.Custiuc, E. Çevik, Z. Durmus, M. Şenel, and A. Durmus, *Electrochemical biosensor based on REGO/Fe₃O₄ bionanocomposite interface for xanthine detection in fish sample.* Food Control, 2015. **57**: p. 402-410.

71. Dervisevic, M., E. Dervisevic, H. Azak, E. Çevik, M. Şenel, and H.B. Yildiz, *Novel amperometric xanthine biosensor based on xanthine oxidase immobilized on electrochemically polymerized 10-[4H-dithieno(3,2-b:2',3'-d)pyrrole-4-yl]decane-1-amine film.* Sensors and Actuators B: Chemical, 2016. **225**: p. 181-187.

72. Joon, A., J. Ahlawat, V. Aggarwal, R. Jaiwal, and C.S. Pundir, *An improved amperometric determination of xanthine with xanthine oxidase nanoparticles for testing of fish meat freshness.* Sensing and Bio-Sensing Research, 2021. **33**: p. 100437.

73. Rahman, M.A., M.-S. Won, and Y.-B. Shim, *Xanthine Sensors Based on Anodic and Cathodic Detection of Enzymatically Generated Hydrogen Peroxide.* Electroanalysis, 2007. **19**: p. 631-637.

74. Devi, R., M. Thakur, and C.S. Pundir, *Construction and application of an amperometric xanthine biosensor based on zinc oxide nanoparticles–polypyrrole composite film.* Biosensors and Bioelectronics, 2011. **26**(8): p. 3420-3426.

75. Devi, R., S. Yadav, and C.S. Pundir, *Electrochemical detection of xanthine in fish meat by xanthine oxidase immobilized on carboxylated multiwalled carbon nanotubes/polyaniline composite film.* Biochemical Engineering Journal, 2011. **58**: p. 148-153.

76. Devi, R., S. Yadav, and C.S. Pundir, *Amperometric determination of xanthine in fish meat by zinc oxide nanoparticle/chitosan/multiwalled carbon nanotube/polyaniline composite film bound xanthine oxidase.* Analyst, 2012. **137**(3): p. 754-759.

77. Devi, R., S. Yadav, and C.S. Pundir, *Au-colloids–polypyrrole nanocomposite film based xanthine biosensor.* 2012. Colloids and Surfaces A: Physiochemical and Engineering Aspects, **394**: p. 38-45.

78. Devi, R., B. Batra, S. Lata, S. Yadav, and C.S. Pundir, *A method for determination of xanthine in meat by amperometric biosensor based on silver nanoparticles/cysteine modified Au electrode.* Process Biochemistry, 2013. **48**(2): p. 242-249.

79. Dervisevic, M., E. Custiuc, E. Çevik, and M. Şenel, *Construction of novel xanthine biosensor by using polymeric mediator/MWCNT nanocomposite layer for fish freshness detection.* Food Chemistry, 2015. **181**: p. 277-283.

80. Dervisevic, M., E.Custiuc, E. Çevik, Z. Durmus, M. Şenel, and A. Durmus,, *Electrochemical biosensor based on REGO/Fe3O4 bionanocomposite interface for xanthine detection in fish sample.* Food Control, 2015. **57**: p. 402-410.

81. Dervisevic, M., E. Dervisevic, H. Azak, E. Çevik, M. Şenel, and H.B. Yildiz, *Novel amperometric xanthine biosensor based on xanthine oxidase immobilized on electrochemically polymerized 10-[4H-dithieno (3, 2-b: 2', 3'-d) pyrrole-4-yl] decane-1-amine film.* Sensors and Actuators B: Chemical , 2016. **225**: p. 181-187.

82. Dervisevic, M., E. Dervisevic, E. Çevik, and M. Şenel, *Novel electrochemical xanthine biosensor based on chitosan–polypyrrole–gold nanoparticles hybrid bio-nanocomposite platform.* Journal of Food and Drug Analysis, 2017. **25**(3): p. 510-519.

83. Narang, J., N. Malhotra, C. Singhal, and C.S. Pundir, *Evaluation of freshness of fishes using MWCNT/TiO$_2$ nanobiocomposites based biosensor.* 2017. **10**: p. 522-528.

84. Tripathi, A., AL. Elias, AB. Jemere, and K.D. Harris, *Amperometric Determination of Xanthine Using Nanostructured NiO Electrodes Loaded with Xanthine Oxidase.* ACS Food Science & Technology, 2022. **2**(8): p. 1307-1317.

85. Sen, S. and P. Sarkar, *A simple electrochemical approach to fabricate functionalized MWCNT-nanogold decorated PEDOT nanohybrid for simultaneous quantification of uric acid, xanthine and hypoxanthine.* Analytica Chimica Acta, 2020. **1114**: p. 15-28.

86. Song, D., Q. Chen, C. Zhai, H. Tao, L. Zang, T. Jia, Z. Lu, W. Sun, P. Yuan, and B. Zhu, *Label-Free ZnIn$_2$S$_4$/UiO-66-NH$_2$ Modified Glassy Carbon Electrode for Electrochemically Assessing Fish Freshness by Monitoring Xanthine and Hypoxanthine.* Chemosensors, 2022. **10**(5): p. 158.

87. Pierini, G.D., S.N. Robeldo, M.A. Zon, M.S. Di Nezio, A.M. Granero, and H. Fernandez, *Development of an electroanalytical method to control quality in fish samples based on an edge plane pyrolytic graphite electrode. Simultaneous determination of hypoxanthine, xanthine and uric acid.* Microchemical Journal, 2018. **138**: p. 58-64.

88. Sharma, N.K., M., A. Kaushal, S. Thakur, N. Thakur, S., D. Kumar, and T.C. Bhalla, *Nanohybrid electrochemical enzyme sensor for xanthine determination in fish samples.* 3 Biotech, 2021. **11**: p. 1-7.

89. Sahyar, B.Y., M. Kaplan, M. Ozsos, E. Celik, and S, Otles, *Electrochemical xanthine detection by enzymatic method based on Ag doped ZnO nanoparticles by using polypyrrole.* Bioelectrochemistry, 2019. **130**: p. 107327.

90. Boluda, A., C.M Casado, B. Alonso, and M.P.G. Armada, *Efficient Oxidase Biosensors Based on Bioelectrocatalytic Surfaces of Electrodeposited*

*Ferrocenyl Polycyclosiloxanes—Pt Nanoparticles.* Chemosensors, 2021. **9**(4): p. 81.

91. Malhotra, D., P.K.L Tran, D.T. Tran, N.H. Kim, and J.H. Lee, *Cobalt-doped cerium oxide nanocrystals shelled 1D SnO₂ structures for highly sensitive and selective xanthine detection in biofluids.* Journal of Colloid and Interface Science, 2021. **600**: p. 299-309.

92. Ghanbari, K. and F. Nejabati, *Ternary nanocomposite-based reduced graphene oxide/chitosan/Cr₂O₃ for the simultaneous determination of dopamine, uric acid, xanthine, and hypoxanthine in fish meat.* Analytical Methods, 2020. **12**(12): p. 1650-1661.

93. Ahmad, M.W., B. Dey, G. Sarkhel, D.J. Yang, and A. Choudhury, *Sea-urchin-like cobalt-MOF on electrospun carbon nanofiber mat as a self-supporting electrode for sensing of xanthine and uric acid.* Journal of Electroanalytical Chemistry, 2022. **920**: p. 116646.

94. Vishnu, N., M. Gandhi, D. Rajagopal, and A.S. Kumar, *Pencil graphite as an elegant electrochemical sensor for separation-free and simultaneous sensing of hypoxanthine, xanthine and uric acid in fish samples.* Analytical Methods, 2017. **9**(15): p. 2265-2274.

# CHAPTER 2

# EXPERIMENTATION

## 2. Introduction

This chapter discusses the various experimental techniques used to prepare and modify CPs and their nanocomposites. Additionally, several analytical approaches have also been used to characterize the CPs and different CP-based nanocomposites. Furthermore, a concise rationale for the selection of a specific Xn and enzyme to assess the selectivity and specificity of the developed biosensors has been included. It has also been attempted to discuss the methods and approaches used to calculate several metrics associated with the efficiency of CP-based nanocomposite for Xn detection.

## 2.1 Materials

The following list of materials was used to conduct several experiments:

## 2.1.1 Chemicals

1,2-Phenylenediamine (o-PD, 99.5%), Xanthine Oxidase (XOs, ≥7 units/mg protein), Glutaraldehyde and Xanthine (≥99.5%) all are purchased from Sigma-Aldrich, USA. Hydrochloric acid (HCl, 0.5 M), Aniline (99.5% pure), Titanium tetrachloride (TiCl$_4$), and ammonium persulphate (APS, ≥98% pure) were taken from Fisher-Scientific, India. Melamine (97.5%) was purchased from Central Drug House, Pvt. Ltd. India, Ferric chloride (Anhydrous, 96% FeCl$_3$) was procured from Rankem, India and indium tin oxide (ITO) coated glass was purchased from Techinstro. All glassware

was autoclaved before use, and double-distilled water (Milli-Q, Millipore, 18.2 MU) was used to make the solutions.

### 2.1.2 Solutions and Buffers

➢ Phosphate buffer saline (PBS) 100 mM, pH 7.4, NaCl (0.9%)

➢ 5 mM $[Fe(CN)_6]^{3-}$ / $[Fe(CN)_6]^{4-}$ in PBS as redox indicator

## 2.2 Techniques for characterization

The work covered in this thesis includes (i) the preparation of CP and their nanocomposites, followed by the deposition of their films onto ITO-coated glass plates, and (ii) the immobilization of an enzyme (Xanthine oxidase) onto CP-based nanocomposites-based electrodes to study their potential applications for Xn detection. These fabricated electrodes/bioelectrodes have been characterized at various stages of preparation using a variety of techniques, including X-ray diffraction (XRD), Fourier transform infrared (FT-IR), UV-Visible (UV-Vis) spectroscopy, Scanning electron microscopy (SEM), Transmission electron microscopy (TEM) and Electrochemical techniques (Electrochemical impedance spectroscopy (EIS), Cyclic voltammetry (CV) and Differential pulse voltammetry (DPV)).

### 2.2.1. X-Ray Diffraction (XRD)

It is a characterization method frequently employed to identify any unidentified crystalline substance [1]. This technique determines the macromolecules in the sample's atomic structure. For very small-scale materials, however, it determines the sample's composition as well as its crystallinity, strain, grain size, and crystal structure

[2]. The polycrystalline sample orientation, crystallite size, and crystallographic structure can all be determined using this method [3]. This technique is based on Bragg's law, which explains how an X-ray beam hitting a sample's crystal lattice will reflect at precise angles, revealing information about the sample's structure and composition [4].

The XRD patterns are recorded with an X-ray diffractometer. **Fig. 2.1** depicts the X-ray diffractometer's schematic diagram. The most significant diffraction peaks are used to measure the average peak broadening and obtain peak broadening data. The structural characteristics of the material can then be examined via this data [5].

In this thesis, the Debye-Scherrer equation **(Eq. 2.1)** is used to determine the average particle size of all synthesized materials:

$$D = K\lambda / \beta\cos\Theta \tag{2.1}$$

where, K= shape factor its value is 0.9, $\lambda$ = X-ray wave length, $\Theta$ = Braggs angle in degree and $\beta$ is the line broadening at full-width half maxima [1, 2].
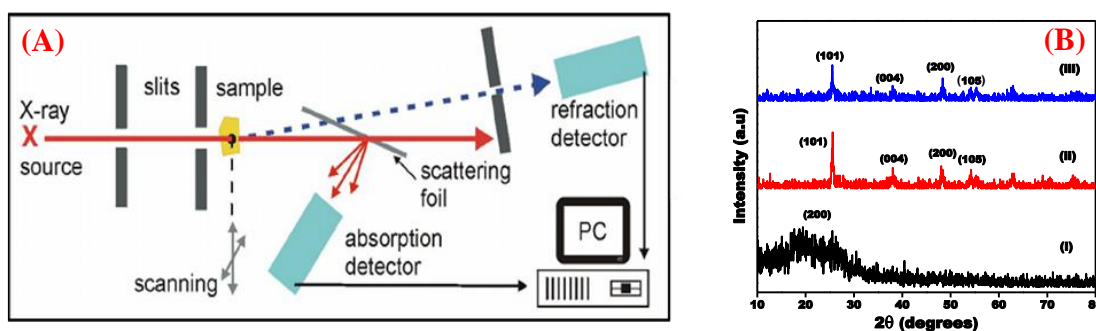


**Fig. 2.1 (A)** Schematic diagram of XRD, **(B)** XRD pattern of (i) PANI, (ii) $TiO_2$ and (iii) PANI@$TiO_2$ nanohybrid

In this thesis, structural characterization involving X-ray diffraction of all prepared materials, including CP-based composites and nanomaterials, was conducted using a Bruker D-8 Advance X-ray diffractometer having diffraction angle ($2\Theta$ = 10-80°) having monochromatic radiation of 1.5406 Å and speed of temperature controller is 2°/min.

**2.2.2 Fourier Transform Infrared (FT-IR) Spectroscopy**

FT-IR is based on infrared radiation to study the interaction of infrared electromagnetic radiation with the material. Due to its excellent accuracy, quick analysis, straightforward handling procedure, and improved sensitivity, it is widely utilized for structural assessment. This eco-friendly method can be used to examine samples of any kind. The atomic vibration of molecules, which absorbs particular energy and frequencies of infrared radiation, is the basis of FTIR. The electromagnetic radiations from the laser beam at each wavelength are absorbed by the material or chemical substance, which results in a variety of spectral lines and further reveals the chemical composition of any material or chemical substance [6].

The Michelson interferometer [7] is employed in FTIR spectroscopy to ascertain the chemical composition of any substance. Its basic construction consists of four parts: (a) the light source (filament); (b) the beam splitter; (c) the two mirrors as shown in **Fig. 2.2 (A)**; and (d) the detector. The source emits infrared radiation and passes through the beam splitter. And then this infrared radiation is separated into two portions by the beam-splitter [8].
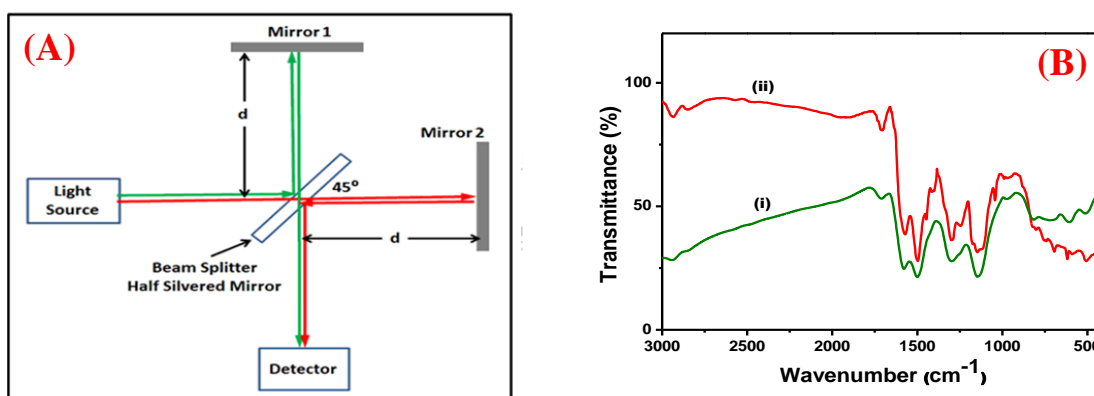
**Fig. 2.2 (A)** Schematic diagram of Michelson interferometer, **(B)** FT-IR of i) PANI and (ii)

PANI@TiO$_2$ nanohybrid

The two distinct light beams continue moving along two different paths until they reflect off mirrors after each path. These distinct beams join again after being reflected, causing interference, which the detector examines. FTIR is a potent characterization method that offers many benefits over dispersive measurements, such as a wider spectrum range, higher sensitivity, quicker data acquisition, a need for fewer samples, more spectral resolution, better signal-to-noise ratio, etc [9]. In this work, FTIR Nicolet TM iS10 at a frequency band of 4000–400 cm$^{-1}$ is used to investigate the functional groups present in all synthetic materials (CPs and their composites).

### 2.2.3 Scanning Electron Microscopy (SEM)

SEM is used to study the surface morphology of the sample. Instead of using light to view the sample's image, the SEM uses electrons. SEM is better than other microscopes because it provides a deeper field of view, making it possible to access more specimens simultaneously. Additionally, specimens are focused to provide greater magnification, indicating a higher SEM resolution[10, 11].
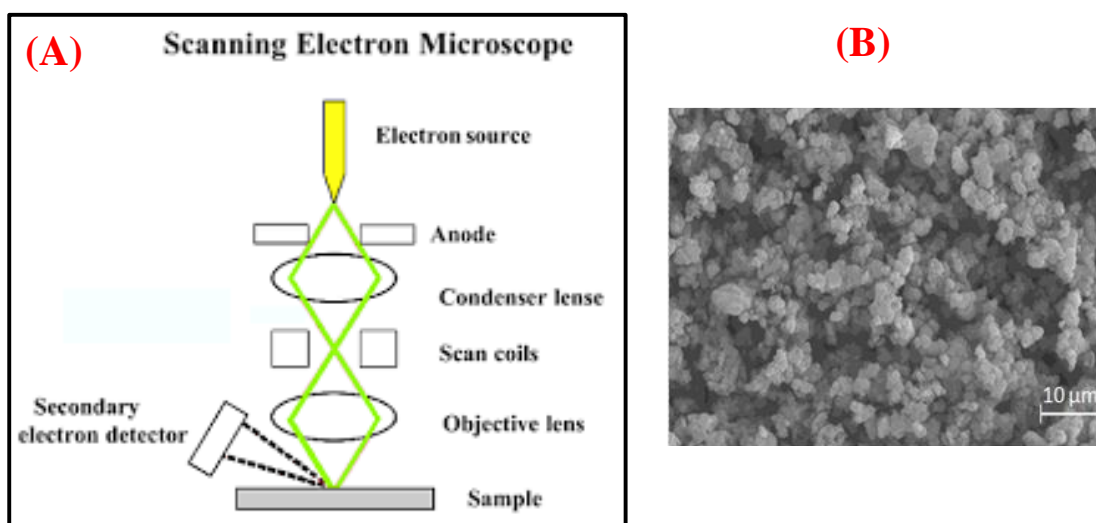
**Fig. 2.3 (A)** Scanning electron microscope **(B)** SEM image of $TiO_2$

The essential parts of a scanning electron microscope (SEM) are an electron source, a column through which an electron beam is directed by an electron detector, electromagnetic lenses, a computer, a specimen chamber and a display unit to see the images. A concentrated stream of highly energetic electrons from the SEM is utilized to produce significant signals at the surface of solid objects, according to the SEM scheme given in **Fig. 2.3 (A)**.

The high-energy electrons are produced at the top of the column and accelerate downward before passing through several lenses and impacting the specimen's surface in a concentrated beam [12]. Additionally, SEM uses a combination of pumps to create vacuum conditions in the specimen chamber to produce images of the specimen. Signals are created as an outcome of the interaction between the specimen and the electron, which are subsequently picked up by detectors [13]. The morphology of synthesized nanoparticles and the constructed electrode surface before and after enzyme immobilization were examined using SEM in the current work.

**2.2.4 Transmission Electron Microscopy (TEM)**

A Transmission Electron Microscope (TEM) is also a microscope that is used to study the image of the smallest structure in matter. Under this microscope, high-energy electrons are used to provide morphological, compositional, and crystallographic information on the samples [14] . TEM can visualize the detailing of the specimen's nanometre range and magnify it up to a million times.

Compared to other microscopes, TEM uses an electron beam of a very short wavelength, compared with visible light, which leads to an increase in the resolution of this microscope. This is the reason for the immense significance of TEM in the biological and medical fields. The image visualization in TEM follows a slightly similar pathway to SEM's. A high-energy electron beam from the electron gun placed at the top of the TEM unit emits electrons traveling through the microscope's vacuum tube.
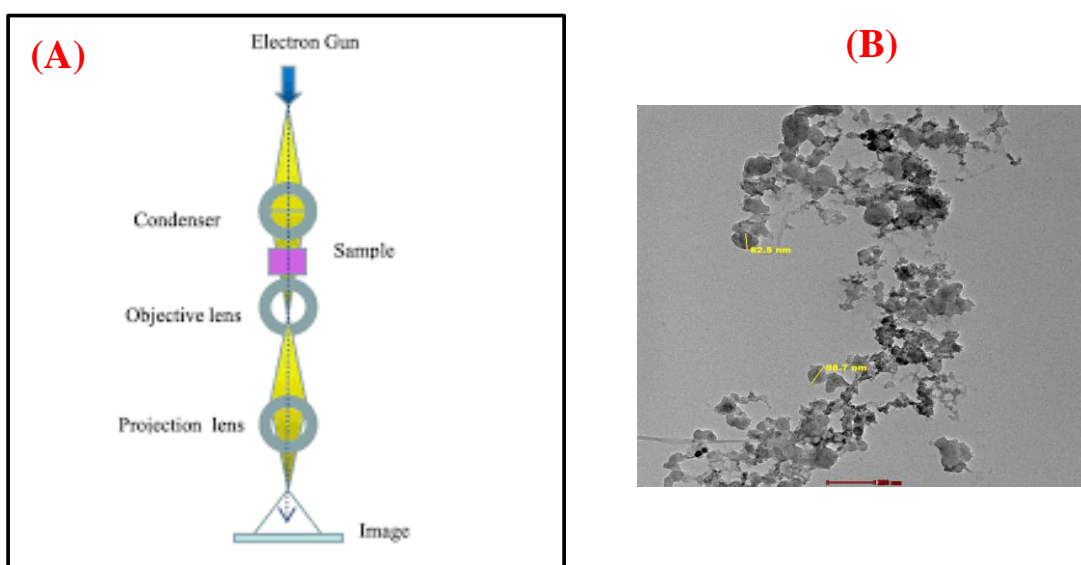


**Fig. 2.4 (A)** Transmission Electron Microscope **(B)** TEM image of  g-C$_3$N$_4$

An electromagnetic lens placed in between focuses the electrons traveling through the tube in a fine beam, which then strikes at the thin specimen. This led to either scattering electrons or hitting the electrons on a fluorescent screen at the bottom of the microscope [15]. After that, the image of the specimen is reflected on the display unit. The image comprises shades of assorted parts of the specimens depending upon the specimen's density on the screen **(Fig. 2.4 (A)) .**

### 2.2.5 Energy Dispersive X-ray Analysis (EDAX)

By analyzing items that are near the surface and estimating the amount of each element at different places, this procedure provides an overall mapping of the sample. EDAX's fundamental idea is applied in conjunction with SEM [16]. Depending on the material being investigated, the conducting sample can generate X-rays when an electron beam with an energy of 10–20 keV hits its surface [17]. EDAX is not categorized as a surface science approach due to X-rays being generated in a zone that penetrates only up to 2 microns deep **(Fig. 2.5 (A)) .**
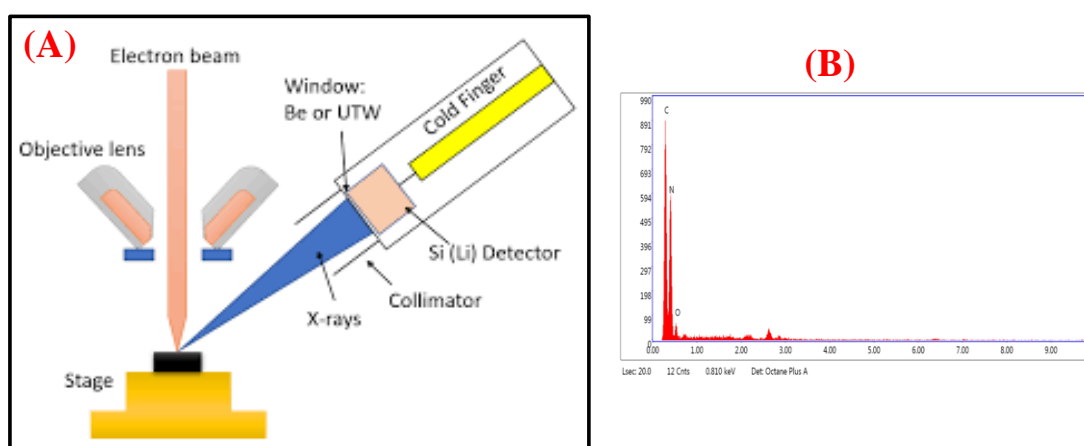


**Fig. 2.5 (A)** Energy Dispersive X-ray **(B)** EDAX plot of PoPD/ITO

During an EDAX assessment, an image of the sample's elements is created by moving the electron beam across the sample. While it is challenging for EDAX to identify elements with atomic numbers below 11, it is possible to measure the composition and quantity of heavy metal ions in nanoparticles that are located near or at the surface of a sample. Each element may be seen individually by moving the electron beam over the sample. As the X-ray intensity is relatively low, obtaining images typically takes numerous hours. If the nanoparticles contain some heavy metal ions, the EDAX can be used to determine their composition when they are close to or at the surface. EDAX, for instance, makes it simple to spot surface-bound nanoparticles of silver, gold, and palladium [18].

## 2.2.6 Thermogravimetric analysis (TGA)

A quantitative evaluation by weight is gravimetric analysis, a branch of science that deals with separating and weighing an element or specific molecule in its purest state. By regulating the sample's temperature in a controlled environment, thermogravimetry (TG) measures a sample's mass as a function of time or temperature. The apparatus's large isothermal zone enables high-temperature repeatability[19].

Along with these quick furnace cooling systems, integrated forced air and running water are also used. The nitrogen ($N_2$) gas was expelled from the TGA to maintain a consistent inert environment. Subsequently, the change in the sample's weight is measured using a microbalance [20].
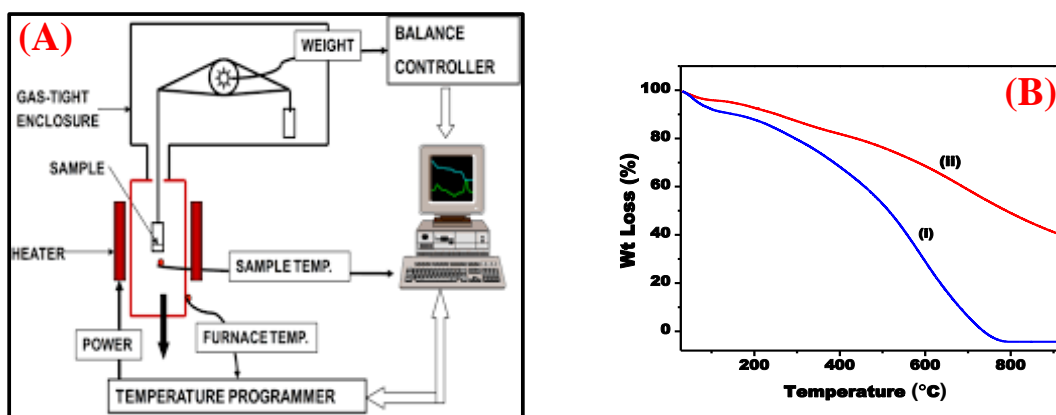
**Fig. 2.6: (A)** Thermogravimetric analysis **(B)** Thermogram of **(i)** PANI and **(ii)** PANI@TiO$_2$ nanohybrid

Only transitions in which gases are absorbed by or evolved from a condensed phase material are suitable for the approach. Most TG equipment is set up to operate in a vacuum or under changing atmospheric conditions. The balances surrounding TG are the most fragile. TG specifies the decomposition temperature and the weight loss that goes along with it. TGA is used to examine the thermal stability, thermal breakdown, and/or absorbed or crystallized water dehydration of materials.

### 2.2.7 Electrochemical techniques

This method of analysis is used to monitor potential, charge, or current and use the information to calculate an analyte's concentration or chemical reactivity. The electrochemical approach's primary objective is to investigate the processes that occur in a system when an electric potential is applied. The reference electrode (RE), the working electrode (WE) and the counter (or auxiliary) electrode (CE) are the three electrodes that make up the majority of electrochemical method cell assemblies. The voltage of the working electrode and related current is regulated by the potentiostat which is connected to the electrodes. When performing an electrochemical experiment, a potential is applied to the working electrode, and the resulting current

response is plotted against time. In different cases, the consequent current is plotted against applied potential which is linearly modulated.

$$E = E° + \frac{RT}{nF} \ln \frac{C_{oxi}}{C_{red}}$$

Nernst's equation **(Eq. 2.2)** states that if a voltage is directed to the working electrode, the redox system will modify the ratios of its concentrations [21].

where, $E°$ is the equilibrium and F the Faraday's constant, $C_{red}$ and $C_{oxi}$ are the concentrations of reduction and oxidation domains

All electrochemical characterization (Cyclic voltammetry, Differential pulse voltammetry) in this thesis was performed using an Autolab (Eco Chemie, Netherlands) Potentiostat/Galvanostat apparatus. The reference electrode was an Ag/AgCl electrode (E = +0.197 V), while the auxiliary electrode was platinum. DC power source is used to obtain precise, regulated, and stable potential using the Potentiostat to produce an even fraction of current at a constant voltage.

## 2.2.7.1 Cyclic Voltammetric (CV) measurements

To describe the electro-catalytical and electrochemical properties, this electro-analytical technique is used. In CV , the working electrode's voltage is varied over time. When the working electrode potential reaches the pre-set point, it will sweep the other way and then reset to its original point. When electroactive species with a known reduction-oxidation potential are involved in electrochemical reactions, information about those reactions is obtained via cyclic voltammetry. The current at the working electrode is monitored during potential scans against a pre-set reference electrode potential. This setup ensures that the electricity is transferred from the signal

source to the working electrode through the counter electrode [22]. In the redox process, the electrolytic solution serves the purpose of supplying ions to the electrodes.

The obtained peak current during CV studies can be used to calculate several physical parameters that predict the efficiency of the electrode.

Based on Laviron's theory,

$$E_{pa} = 2.303RT/(1-\alpha)nF \text{ and } E_{pc} = -2.303RT/\alpha \, n \, F \qquad (2.3)$$

$$\Delta E_p = E_{pa} - E_{pc} \qquad (2.4)$$

$$\ln K_s = \alpha \ln (1-\alpha) + (1-\alpha) \ln \alpha - \ln (R \, T/n \, F \, \upsilon) - \alpha (1-\alpha) \, n \, F \, \Delta E_p / R \, T \qquad (2.5)$$

where $E_{pa}$ is anodic and $E_{pc}$ is cathodic peak potentials respectively [19], $\alpha$ is the charge transfer coefficient, R is the universal gas constant, F is Faraday's constant, $K_{\alpha}$ is heterogeneous electron transfer rate constant, $\upsilon$ is scan rate [17].

Several other parameters can be calculated using the Randles–Ševčík equation [20]:

$$I_p = (2.69 \times 10^5) \, n^{3/2} \, AcD^{1/2} \upsilon^{1/2} \qquad (2.6)$$

$$I_p = n^2F^2A\Gamma\upsilon/ \, 4RT \qquad (2.7)$$

where $I_p$ is anodic peak current, n is electron per molecule oxidized or reduced, c is the molar concentration of $[Fe(CN)_6]^{3-/4-}$ in $mol/cm^3$, $\upsilon$ is scan rate (mV/sec), $D^{1/2}$ is diffusion coefficient, $\Gamma$ is the surface concentration of modified material on ITO electrode [21].

In this thesis work, CV studies ranging from a scan rate of 10 mV/s to 300 mV/s has been performed in the potential window: -0.6V to 0.6V in Chapters 3, 4 and 5 to study the different electrochemical properties of the fabricated electrodes and bioelectrodes. The Autolab potentiostat/galvanostat (Eco-Chemie, Nether-lands) having a three-electrode system was used to perform electrochemical experiments with ITO as a working electrode, platinum as an auxiliary electrode and Ag/AgCl as a reference electrode in phosphate buffer (PBS, 100 mM, pH 7.4, 0.9% NaCl) containing 5 mM $[Fe(CN)_6]^{3-/4-}$.
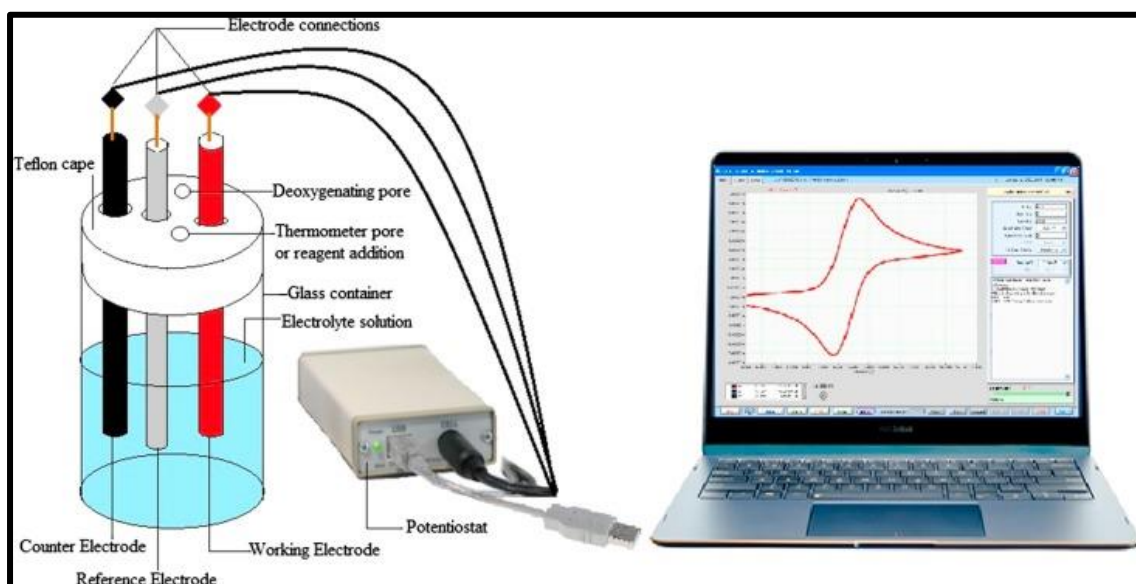


**Fig. 2.7** Working scheme of potentiostat

## 2.2.7.2 Differential Pulse Voltammetry (DPV)

The detection limits of DPV are higher than CV's, making it possible to resolve electrode processes that are positioned together. Here, a ramp that ascends linearly is used to apply the voltage versus time program to the electrode. The current between a raised baseline voltage and a series of pulses with small amplitudes is then monitored. The current for each pulse is measured at two different places. The initial point

55

happens right before the pulse is delivered, and the latter point happens after the pulse has been delivered. These peak positions are picked so that the non-faradic (charging) current may disappear. The fluctuation of the measured currents at these places to the base potential is recorded for each pulse. DPV presents a greater detection limit than CV and other voltammetric techniques due to improved discriminating between charging current and impurity Faradic currents [22,23].

### 2.2.7.3 Electrochemical Impedance Spectroscopic (EIS) measurements

EIS is used to examine the interfaces between conducting electrodes and the electrical characteristics of materials. The Ohm's law specifies the maximum current a circuit component may resist. The most common method for determining an electrochemical impedance involves supplying AC voltage to an electrochemical cell and monitoring its current flow. Most likely, a sinusoidal potential stimulation was used, leading to the generation of an AC signal. A small excitation pulse is commonly used to measure electrochemical impedance and get a pseudo-linear response from the electrochemical cell [24].

A sinusoidal waveform with the same frequency is present in the matching current regardless of the phase shift. Current responses are sinusoidal in linear systems. It is possible to ascertain physically significant properties of the electrochemical system by modelling the impedance data as, $R_{ct}$ (charge transfer resistance), $R_s$ (solution resistance) and $C_{dl}$ (double layer capacitance). The cell's diffusion or mass transport impedance is also shown using $Z_w$ (Warburg element). For electrochemical cells, the equivalent circuit model EIS data is represented using the Nyquist plot, where the

imaginary impedance, symbolizes the capacitive and inductive properties of the electrochemical cell [25].

This thesis employs EIS to compute $R_{ct}$ from the acquired EIS spectra. The impedance spectra are fitted using an equivalent Randles and Ershler circuit model to derive the necessary parameters. Based on the obtained $R_{ct}$ values, the exchange current per geometric unit area ($i_o$) and heterogeneous electron transfer rate constant ($k_{app}$) of the different electrodes are calculated by equations **(2.8)** and **(2.9)**:

$i_o = nRT/R_{ct}F$ **(2.8)**

$k_{app} = RT/n^2F^2AR_{ct}C$ **(2.9)**

where R is the universal gas constant, F is Faraday's constant, n is the number of electrons transferred, A is the geometrical area of electrodes, T is the temperature in Kelvin and C is the concentration of the electro-active redox probe

## 2.3 Immobilization of enzyme to the CP-based matrix

In order to prevent denaturation, it is essential to use the appropriate method for an enzyme attachment while immobilizing it to the matrix. This method should not affect the antibody's reactive groups or chemical composition. Covalent immobilization is a widely explored technique. In this technique, a biomolecule and a support matrix create covalent bonds. Nucleophilic functional groups (-SH, -NH$_2$, -OH) that can form covalent bonds or that can be activated to form groups that can form bonds with biomolecules can be employed. Due to the extraordinarily strong binding force between an enzyme and matrix, no enzyme leakage is feasible in this instance of

covalent immobilization, regardless of the presence of substrate or a solution with high ionic strength. Because this immobilization technology is strong and selective and the synthesized PANI and its derivatives-based matrix contain $NH_2$ groups, we applied the glutaraldehyde process. The $NH_2$ group of the aminated enzyme and the amide bond are formed during this immobilization process [26].

## 2.4 Extraction of Xn for real sample analysis

DPV was employed to assess the biosensor's suitability for analysing real fish meat samples. The extraction of Xn from Rohu (*Labeo rohita*) fish and the preparation of the Xn solution were conducted following a method proposed by Watanabe et al. In summary, fresh Rohu fish was chopped and centrifuged at 4000 rpm in 15 mL of distilled water. The resulting mixture was then filtered and diluted by a factor of 100 to achieve the desired concentration for the experiments [27].

## 2.5 Kinetic parameters of CP-based nanocomposites biosensor

### 2.5.1. Detection range, Sensitivity and LOD

The detection range is defined as the concentration range for which the biosensor response changes linearly with concentration. The slope of the linearity curve has been used to evaluate the sensitivity. Furthermore, **Eq. 2.10** has been used to establish the limit of detection (LOD).

$LOD= 3\sigma_b /Sensitivity$ **(2.10)**

where $\sigma_b$ is the standard deviation

**2.5.2 Stability and reproducibility**

The primary factors that affect the stability of bioelectrodes are the material utilized, the shape of the film that is generated, and the method of biomolecule immobilization. A sensor's shelf life or stability refers to how long it is deemed appropriate for use and how long it may continue to function. While the reproducibility keeps track of how many times the bioelectrode can be used, the shelf-life of the devices is calculated by checking their current response at regular intervals.

# References

1.    Ali, A., Y.W. Chiang, and R.M. Santos, *X-ray Diffraction Techniques for Mineral Characterization: A Review for Engineers of the Fundamentals, Applications, and Research Directions.* 2022. **12**(2): p. 205.

2.    Jacob, R., H.G. Nair, and J. Isac, *Structural and morphological studies of nano-crystalline ceramic BaSr$_{0.9}$ Fe$_{0.1}$ TiO$_4$.* International Letters of Chemistry, Physics and Astronomy, 2015. **41**: p. 100-117.

3.    Barman, B. and K.C. Sarma, *Structural characterization of PVA capped ZnS nanostructured thin films.* Indian JournaL of Physics, 2012. **86**: p. 703-707.

4.    Sivia, D.S., *Elementary scattering theory: for X-ray and neutron users.* 2011: Oxford University Press.

5.    West, A.R., *Solid state chemistry and its applications.* 2022: John Wiley & Sons.

6.    Stuart, B.H., *Infrared spectroscopy: fundamentals and applications.* 2004: John Wiley & Sons.

7.    Chai, J., K. Zhang, Y. Xue, W. Liu, T. Chen, Y. Lu, and G. Zhao, *Review of MEMS based Fourier transform spectrometers.* Micromachines, 2020. **11**(2): p. 214.

8.    Ni, Z., Q. Lu, X. Yu, and H. Huo, *Intensity Simulation of a Fourier Transform Infrared Spectrometer.* Sensors, 2020. **20**(7): p. 1833.

9.    Griffiths, P.R., *Fourier transform infrared spectrometry.* 1983. **222**(4621): p. 297-302.

10.   Goldstein, J., *Practical scanning electron microscopy: electron and ion microprobe analysis.* 2012: Springer Science & Business Media.

11.   Hafner, B.J.C.F., University of Minnesota-Twin Cities, *Scanning electron microscopy primer.* 2007: p. 1-29.

12. Erdman, N., D.C. Bell, and R. Reichelt, *Scanning Electron Microscopy*, in *Springer Handbook of Microscopy*, P.W. Hawkes and J.C.H. Spence, Editors. 2019, Springer International Publishing: Cham. p. 229-318.

13. Robinson, V., *The Development of Variable Pressure Scanning Electron Microscopy.* Microscopy and Analysis, 2016. **30**: p. 17-21.

14. Fultz, B. and J.M. Howe, *Transmission electron microscopy and diffractometry of materials*. 2012: Springer Science & Business Media.

15. Franken, L.E., K. Grünewald, E.J. Boekema, and M.C.A Stuart, *A Technical Introduction to Transmission Electron Microscopy for Soft-Matter: Imaging, Possibilities, Choices, and Technical Developments.* Small, 2020. **16**(14): p. 1906198.

16. Martín-Viveros, J.I. and A. Ollé, *Using 3D digital microscopy and SEM-EDX for in-situ residue analysis: A multi-analytical contextual approach on experimental stone tools.* Quaternary International, 2020. **569-570**: p. 228-262.

17. Morgan, A.J., *X-ray microanalysis in electron microscopy for biologists.* Royal Microscopical Society Microscopy Handbook, 1985. **5**: p. 1-79.

18. Scimeca, M., S. Bischetti, H.K. Lamsira, R. Bonfiglio, and E. Bonanno, *Energy Dispersive X-ray (EDX) microanalysis: A powerful tool in biomedical research and diagnosis.* European Journal of Histochemistry, 2018. **62**(1): p. 2841.

19. Teh, J.S., Y.H. Teoh, H.G. How, and F. Sher, *Thermal Analysis Technologies for Biomass Feedstocks: A State-of-the-Art Review.* Processes, 2021. **9**(9): p. 1610.

20. Saadatkhah, N., A.C. Garcia, S. Ackermann, P. Leclerc, M. Latifi, S. Samih, G.S. Patience, and J. Chaouki, *Experimental Methods in Chemical Engineering: Thermogravimetric Analysis—TGA.* The Canadian Journal of Chemical Engineering, 2019. **98**.

21. Grieshaber, D., R. MacKenzie, J. Vörös, and E. Reimhult, *Electrochemical Biosensors - Sensor Principles and Architectures.* Sensors (Basel), 2008. **8**(3): p. 1400-1458.

22. Elgrishi, N., K.J. Rountree, B.D. McCarthy, E.S. Rountree, T.T. Eisenhart, and J.L. Dempsey, *A Practical Beginner's Guide to Cyclic Voltammetry.* Journal of Chemical Education, 2018. **95**(2): p. 197-206.

23. Aikens, D.A., *Electrochemical methods, fundamentals and applications.* Journal of Chemical Education, 1983. **60**(1): p. A25.

24. Zhang, N., M. Halali, and C. de Lannoy, *Detection of Fouling on Electrically Conductive Membranes by Electrical Impedance Spectroscopy.* Separation and Purification Technology, 2020. **242**: p. 116823.

25. Schmid, A. and K. Birke, *Potential of Capacitive Effects in Lithium-ion Cells.* Modern Battery Engineering, 2019. p. 187-222.

26. Thakur, D., C.M. Pandey, and D. Kumar, *Highly Sensitive Enzymatic Biosensor Based on Polyaniline-Wrapped Titanium Dioxide Nanohybrid for Fish Freshness Detection.* Applied Biochemistry and Biotechnology, 2022. **194**.

27. Dolmacı, N., S. Çete, F. Arslan, and A. Yaşar, *An amperometric biosensor for fish freshness detection from xanthine oxidase immobilized in polypyrrole-polyvinylsulphonate film.* Artificial Cells, Blood Substitutes, and Biotechnology, 2012. **40**(4): p. 275-279.

# CHAPTER 3

# PANI@TIO₂-BASED BIOSENSOR FOR XANTHINE DETECTION

## 3. Introduction

This study discusses a highly sensitive and efficient electrochemical biosensor for xanthine detection using titanium oxide ($TiO_2$) nanoparticles reinforced polyaniline (PANI) nanocomposite. The PANI@TiO₂ nanohybrid demonstrates a significant increase in electro-active surface area, electron kinetics, and catalytic activity, electrochemical performance [1]. The fabricated biosensor showed high sensitivity (0.415 µA M$^{-1}$), a low limit of detection (0.1 µM), and good selectivity for xanthine detection to evaluate fish freshness.
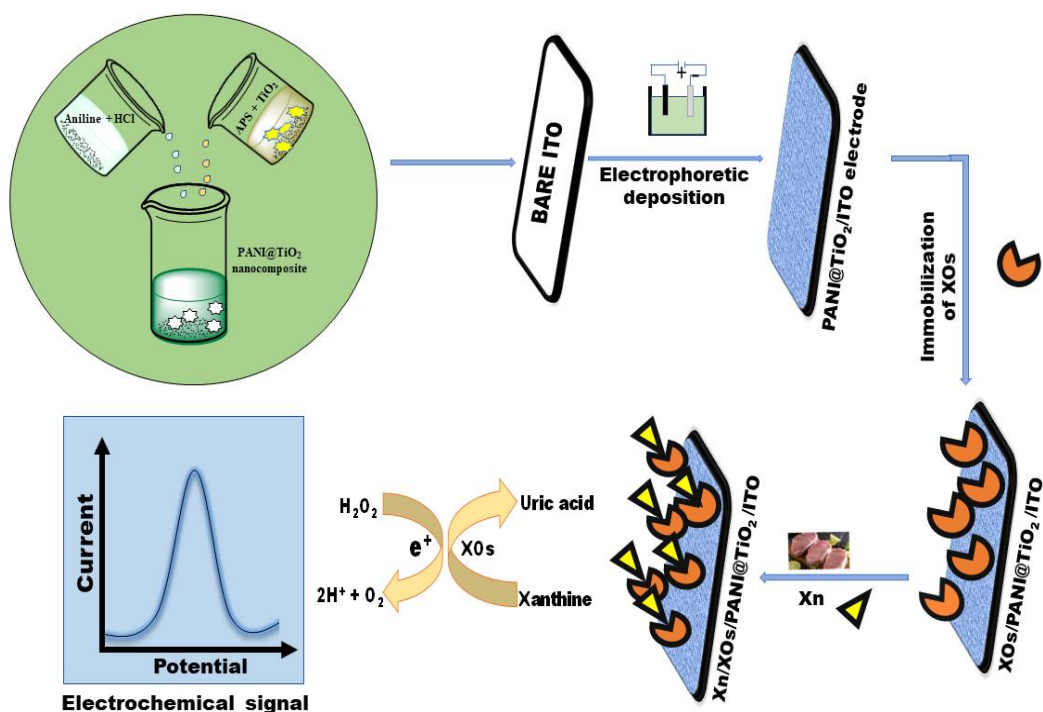


**Fig. 3.1:** Schematic illustration for the fabrication of PANI@TiO₂ nanohybrid-based biosensor

## 3.1. Experimentation

### 3.1.1. Synthesis of TiO₂ nanoparticles

TiO$_2$ has been synthesized using the reported method with slight modification [2, 3]**.** In brief, TiCl$_4$ (1mL) was added to a diluted H$_2$SO$_4$ solution (10%) in an ice bath (0°C) under constant stirring. Due to the hydrolysis of TiCl$_4$, the solution turned grey, which was then heated at 60°C till a clear solution was obtained, followed by aging (1h) at room temperature. Dropwise additions of conc. NH$_4$OH (40 mL) was made until the solution's pH reached to 7.0 and the mixture converted to white colour. The mixture was then left to cool, filtered, and rinsed with DI. The obtained precipitate was dried using a vacuum oven, followed by calcination at 400°C.

### 3.1.2. Synthesis of PANI@TiO₂ nanohybrid

The PANI@TiO$_2$ nanohybrid was chemically synthesized, where aniline and ammonium persulphate (APS) were used as a monomer and oxidant, respectively. Distilled aniline (1mL) was dissolved in HCl (0.5M) in a beaker, under continuous stirring for 10 h in an ice bath (-2˚C to -4˚C). APS (1mL) and synthesized TiO$_2$ (0.2mg) were added to the above solution followed by sonication for 2h and left undisturbed at 4˚C for 24 h. The obtained precipitate was filtered and washed using HCl (2M) and then vacuum dried at 60˚C for 24 h [4].

### 3.1.3. Electrophoretic deposition (EPD) of PANI@TiO₂ nanohybrid

A two-electrode setup was used for the EPD of a synthesized PANI@TiO$_2$ nanohybrid onto a freshly cleaned ITO. The colloidal solution of the above nanohybrid undergoes sonication in DI water before deposition until a homogeneous solution is obtained. Following this step, a sonicated solution of 10 mL was diluted with 5 mL of ethanol,

and Electrophoretic Deposition (EPD) was carried out for 25s under a DC potential of 10 V.

### 3.1.4. Immobilization of XOs on PANI@TiO$_2$ nanohybrid-based biosensor

To fabricate the XOs/PANI@TiO$_2$/ITO electrode, 0.1% glutaraldehyde was drop-cast to the electrode and left in a humid chamber for 1h at room temperature. The electrode was then rinsed with PBS (pH 7.4,100 mM, 0.9% NaCl), covalently immobilized with XOs (20µL), and left overnight in a humid chamber at 4°C.

## 3.2. Results & Discussion

### 3.2.1. Structural and morphological studies

**Fig 3.2 (A)** shows the XRD pattern of PANI, TiO$_2$, and PANI@TiO$_2$ nanohybrid. The broad diffraction peak around $2\theta = 20 - 25°$ indicates the partially crystalline nature of PANI **(curve (i)).** But the typical peaks are at $2\theta = 25.5°$, $38.14°$, and $48.09°$, corresponding to the (101), (004), and (200) diffraction planes, respectively, which shows that the TiO$_2$ nanoparticles in the PANI matrix are present. **(curve (iii)).** As a result, TiO$_2$'s extremely crystalline structure, overpowered the distinctive low-intensity peaks of PANI, leading to the same diffraction pattern of the synthesized PANI@TiO$_2$ nanohybrid and TiO$_2$ **(curve (ii))** and does not exhibit any peak for PANI. The strong and sharp peaks designate good crystallinity [5].

**Fig 3.2 (B)** represents the FTIR spectra of PANI and PANI@TiO$_2$ nanohybrid, respectively.   In curve (i); at 3490 cm$^{-1}$, there was a wider peak with a modest transition percentage, corresponding to the N–H stretching vibration of the amino group of PANI. The strong peaks around 1504 and 1592 cm$^{-1}$ are associated with the

benzenoid and quinonoid ring stretching vibrations. The asymmetric and symmetric stretching vibration modes of methyl groups are attributed to the absorption band at 2927 cm$^{-1}$. The peak at 1296 cm$^{-1}$ corresponds to the C–N stretching of secondary aromatic amines. The C=N stretching vibration is attributed to the characteristic and absorption bands in-plane bending vibration of the C–H mode at 1145 and 1117 cm$^{-1}$, respectively. The peaks found in the curve (ii) revealed the presence of Ti-O vibrations, which closely resemble PANI with minor intensity shifts excluding the absorption band in the region of 400–800 cm$^{-1}$. The PANI@TiO$_2$ nanohybrid also exhibits two additional peaks at 618 and 569 cm$^{-1}$ (are there in curve (iii)) that are attributed to Ti-O stretching vibrations, indicating the effective incorporation of TiO$_2$ into the PANI matrix. [6, 7].
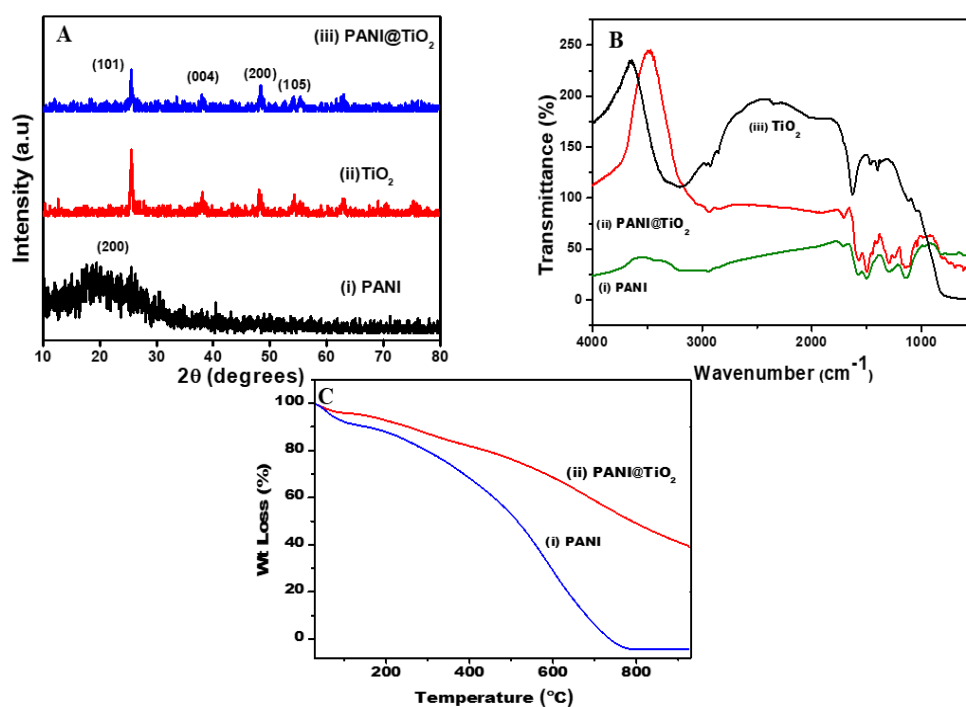


**Fig 3.2: (A)** XRD of (i) PANI (ii) TiO$_2$ nanoparticles, and (iii) PANI@TiO$_2$ nanohybrid **(B)** FT-IR spectra of (i) PANI (ii) PANI@TiO$_2$ nanohybrid and (iii) TiO$_2$ nanoparticles; **(C)** TGA curve of (i) PANI and (ii) PANI@TiO$_2$ nanohybrid

The thermal stability of PANI & PANI@TiO$_2$ nanohybrid is shown in **Fig 3.2 (C).** Initially, the weight loss occurs due to the evaporation of the H$_2$O molecules present in the material. Due to the breaking of dopant bonds, PANI's weight (10%) rapidly decreases at a temperature of 280˚C **(curve i)**. The mass then gradually decreases between 280˚-600˚C. The PANI@TiO$_2$ nanohybrid, however, possesses good thermal stability with just a 4% weight loss from 100˚ to 400˚C, and the degradation accelerates after 400˚C **(curve ii)**. Compared to the bare PANI, the PANI@TiO$_2$ nanohybrid showed better thermal stability, as seen by its lower weight loss at 600 °C [8].

**Figure 3.2 (C)** illustrates the thermal stability of PANI and PANI@TiO$_2$ nanohybrid. Initially, the weight loss is attributed to the evaporation of water molecules within the substance. PANI experiences a 10% weight loss at 280˚C due to dopant bond breakage **(curve i),** with a gradual decrease in mass between 280˚C and 600˚C. The results indicate that PANI@TiO$_2$ nanohybrid exhibits favourable thermal stability, with only a 4% weight loss within the 100˚C to 400˚C temperature range. However, degradation accelerates beyond 400˚C **(curve ii)**. Compared to pure PANI, the PANI@TiO$_2$ nanohybrid demonstrates enhanced thermal stability, as evidenced by its reduced weight loss at 600°C.

The SEM image of PANI@TiO$_2$/ITO **((Fig 3.3 (C))** shows that the TiO$_2$ (**Fig 3.3 (B)**) nanoparticles of size ≤50 nm are finely distributed over the PANI surface (**Fig 3.3 (A))**. The morphology changed after XOs were immobilized on the PANI@TiO$_2$/ITO electrode, indicating that the enzyme has been evenly distributed across the surface **((Fig 3.3 (D)).**
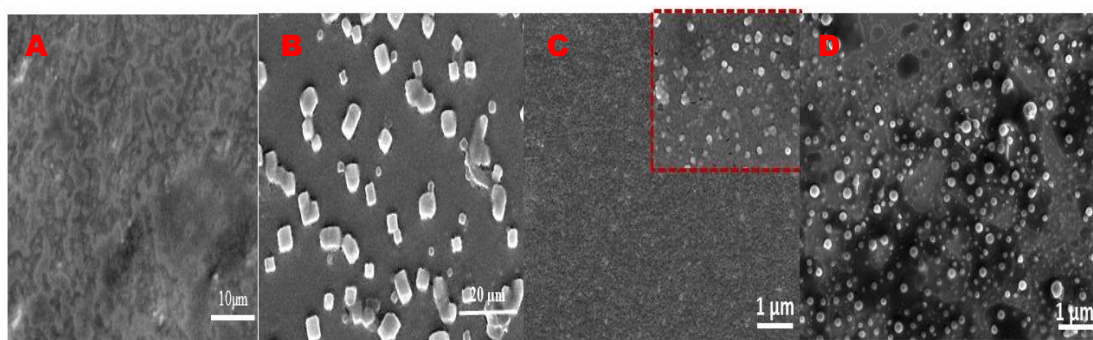
**Fig 3.3:** SEM images of **(A)** PANI ; **(B)** TiO$_2$ ; **(C)** PANI@TiO$_2$/ITO and **(D)** XOs/PANI @TiO$_2$/ITO electrodes

## 3.2.2. Electrochemical Characterization

Cyclic voltammetric studies have been used for the electrochemical studies of different modified electrodes (PANI/ITO, PANI@TiO$_2$/ITO, and XOs/PANI @TiO$_2$/ITO) in PBS (pH 7.5, 5 mM [Fe (CN)$_6$]$^{3-/4-}$ ) **(Fig 3.4 (B)).** It has been observed that the PANI@TiO$_2$/ITO electrode has a higher redox peak current (0.49mA; **curve (ii)**) than that of the PANI/ITO electrode **(curve i)** [9]. After XOs immobilization on PANI@TiO$_2$/ITO, the redox peaks become increase (2.02 mA; **curve (iii)**). This suggests the electron was transferred directly from the XO's active site to the electrode. In addition, more enzymes are interacting with the redox couple, which causes the rise in the ferro-ferri oxidation signal [10]. EIS of bare ITO, PANI/ITO electrodes and PANI@TiO$_2$/ITO electrodes have been investigated using EIS (PBS 5mM of [Fe(CN)$_6$]$^{3-/4-}$) in the frequency range of 0.01–10$^5$ Hz Fig 3.4 (A)). The Nyquist plot exhibits a linear region at lower frequencies, indicating a diffusion-controlled electron transfer resistance process. Conversely, the electron transfer resistance-limited process is characterized by a semicircular region [11]. The higher the semicircle diameter, the higher the electron resistance (R$_{ct}$), which can be

quantitatively deduced from the equivalent circuit model **(Fig 3.4 (A) (inset))** proposed

by Randles and Ershler.
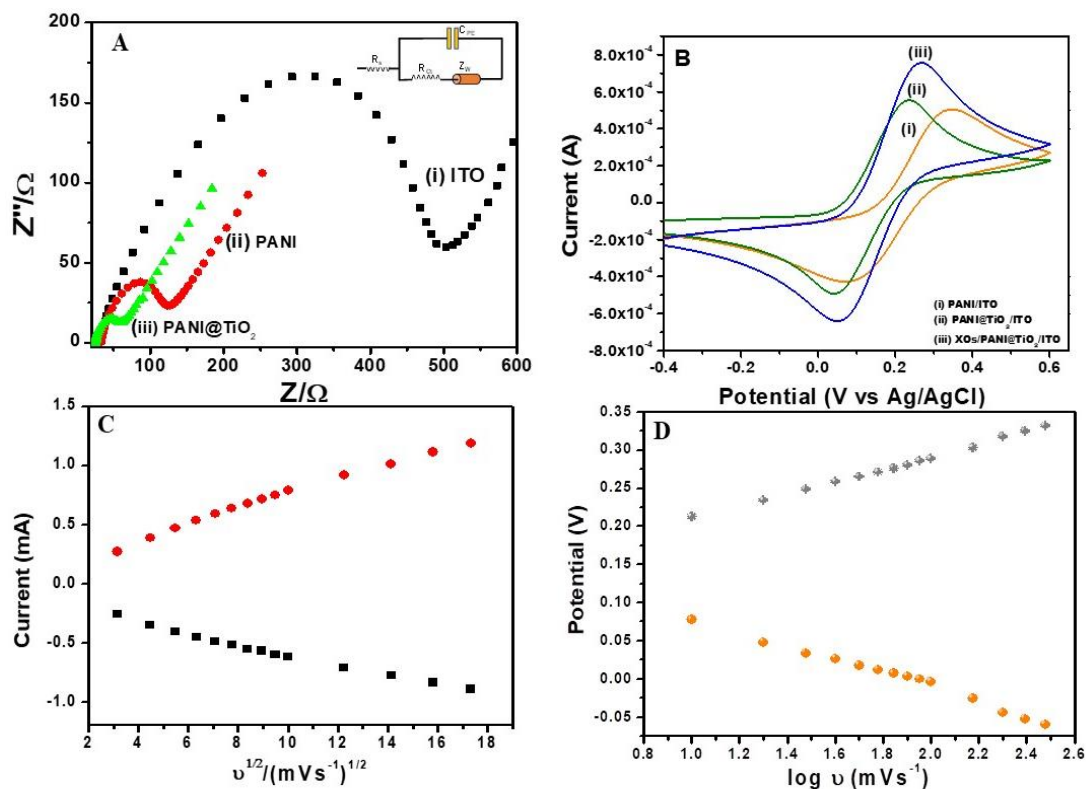


**Fig. 3.4: (A)** EIS of (i) ITO, (ii) PANI/ITO, and (iii) PANI@TiO$_2$/ITO; **(B)** Cyclic voltammetry analysis of (i) PANI/ITO, (ii) PANI@TiO$_2$/ITO and (iii) XOs/PANI@TiO$_2$/ITO electrodes. The plots of **(C)** I$_{pa}$, I$_{pc}$ vs. square root of scan rate and **(D)** potential with log of scan rate at varying scan rate (10–300 mV) for PANI@TiO$_2$/ITO electrode.

The R$_{ct}$ values for the ITO, PANI/ITO and PANI@TiO$_2$/ITO were determined to be

500.5 Ω **(curve (i)),** 123.9 Ω **(curve (ii))** and 60.09 Ω **(curve (iii))**, respectively. The

PANI@TiO$_2$/ITO electrode has a lower R$_{ct}$ value than the PANI electrode because of the

synergistic interaction between PANI and TiO$_2$ which provides a route for charge transfer

[12]. The PANI/ITO electrode and the PANI@TiO$_2$/ITO electrode were found to have an exchange current per geometric unit area (i$_o$) of 20.72×10$^{-5}$Acm$^{-2}$ and 42.73×10$^{-5}$ Acm$^{-2}$, respectively. Similarly, the apparent electron transfer rate constants (K$_{app}$) for the PANI/ITO and PANI@TiO$_2$/ITO electrodes were determined to be 1.705×10$^{-6}$ cms$^{-1}$ and 3.515×10$^{-6}$ cms$^{-1}$, respectively.

The PANI@TiO$_2$/ITO electrode shows greater values for i$_o$ and K$_{app}$ than the PANI/ITO electrode, which clearly explains that the redox couple is diffusing in a controlled manner. The performance of the PANI@TiO$_2$/ITO electrode was examined by altering the scan rate (10 to 300 mV/s). The oxidation peak current has been observed to increase linearly in response to an increase in peak potential. Both the anodic peak (I$_{pa}$), and cathodic peak (I$_{pc}$) currents increase linearly with increasing scan rate and follow the equations (3.1) & (3.2) showing surface adsorption-controlled process kinetics for PANI@TiO$_2$/ITO electrode **(Fig 3.4 (C))**.

$$Ipa\ (\mu A) = \ 1.284 \times 10^{-4} \ + \ 6.310 \times 10^{-5} \ \sqrt{v}\left(\frac{mV}{s}\right); \ R = \ 0.9957 \qquad \textbf{(3.1)}$$

$$Ipc\ (\mu A) = \ -1.710 \times 10^{-4} - 4.297 \times 10^{-5} \ \sqrt{v}\left(\frac{mV}{s}\right); \ R = \ 0.9929 \qquad \textbf{(3.2)}$$

Similar to this, a linear relationship between the anodic peak potential (E$_{pa}$) and cathodic peak potential (E$_{pc}$) was seen with the natural logarithm of scan rate (ln $v$). Eqs (3) & (4) represent the corresponding linear regression equations illustrating the same **(Fig. 3.4 (D))**.

$$Epa\ (V) = \ 0.133\ln(v) + 0.079\,; R \ = \ 0.9755 \qquad \textbf{(3.3)}$$

$$Epc(V) = \ 0.174\,ln(v) - 0.093\,; R \ = \ 0.9868 \qquad \textbf{(3.4)}$$

The heterogeneous electron transfer coefficient ($K_s$) and the charge transfer coefficient

($\alpha$) for PANI@TiO$_2$/ITO were determined to be 1.5446 s$^{-1}$ and 0.9010s$^{-1}$, respectively,

using Laviron's equation **(Eq.2.5),** at a scan rate (v) of 50 mV/s. Based on the linearity

curves and Randles Sevick equation **(Eq.2.6),** the diffusion coefficient (D) calculated

for the PANI@TiO$_2$/ITO electrode is 5.48×10 $^{-11}$ cm$^2$ s$^{-1}$. **Table 3.1** presents different

kinetic parameters calculated for both the PANI@TiO$_2$/ITO and

XOs/PANI@TiO$_2$/ITO electrodes. These values demonstrate that the PANI@TiO$_2$

nanohybrid exhibits superior conductivity compared to pristine PANI. This enhanced

conductivity accelerates the rate of charge transfer and provides a singular channel for

interaction with the enzyme.

**Table 3.1:** Kinetic parameters of *PANI@TiO$_2$/ITO* and *XOs/PANI@TiO$_2$/ITO* electrodes

| S.No. | Name of the electrode | Electron transfer coefficient, $\alpha$ | Charge transfer rate constant, $K_s$/s | Effective surface area, $A_{eff}$/mm$^2$ | Average surface coverage, mol cm$^{-1}$ | Diffusion coefficient, D/cm$^2$s$^{-1}$ |
|---|---|---|---|---|---|---|
| 1. | PANI@TiO$_2$/ITO | 0.9010 | 1.544 | 0.24 | 5.001 x10$^{-8}$ | 5.48 x 10$^{-11}$ |
| 2. | XOs/PANI@TiO$_2$/ITO | 0.9040 | 1.682 | 0.25 | 6.459x10$^{-8}$ | 9.11 x 10$^{-11}$ |

### 3.2.3. Electrochemical biosensing studies

Biosensing studies were conducted using the XOs/PANI@TiO$_2$/ITO electrode,

examining a range of Xn concentrations (1-100µM) in PBS (7.5) containing 5 mM

[Fe (CN)$_6$]$^{3-/4-}$ **(Fig 3.5 (A)).** It was noted that there was a linear rise in the peak

current response as the Xn concentration increased.

This linear relation between the current response and concentration of Xn, explains the presence of direct electron transfer between the Xn and the XOs/PANI@TiO$_2$/ITO electrode **(Fig. 3.5 (B))**.
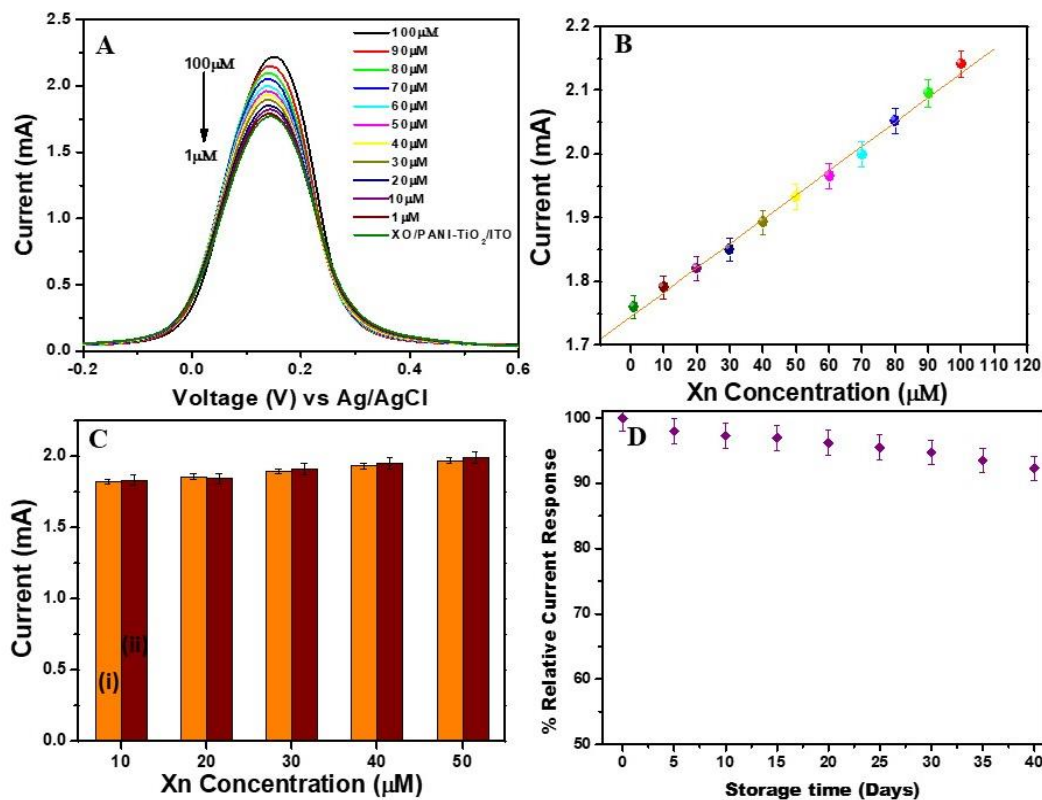


**Fig. 3.5.** Electrochemical response study of the **(A)** XOs/PANI@TiO$_2$/ITO as a function of Xn concentration (1–100 μM); **(B)** Linearity plot between the concentration of Xn and current recorded on XOs/PANI@TiO$_2$/ITO; **(C)** Analysis of real sample with (i) buffer sample and (ii) real fish sample; and **(D)** stability study of XOs/PANI@TiO$_2$/ITO electrode over 40 days

The sensitivity of the fabricated biosensor was found to be 0.415 μA M$^{-1}$ with R$^2$ =0.9942. The limit of detection (LOD) calculated using the equation 3σ/Sensitivity for

the developed biosensor was 0.1µM, where σ is the standard deviation of the bioelectrode.

### 3.2.4. Validation of biosensor with real sample

DPV was used to assess the viability of the developed PANI@TiO$_2$/ITO biosensor to analyze fish meat samples [13]. DPV results show that peak current constantly increases as Xn concentration (10-50 µM) rises, and the outcomes are comparable to those of synthetic Xn samples **(Fig 3.5 (C))** [14].

### 3.2.5. Reproducibility and Stability

Voltametric studies have also been used to assess the repeatability of the developed biosensor. For the XOs/PANI@TiO$_2$/ITO electrode, the value of percent recoveries is varied from 96 to 99%, with a RSD value of less than 4% (n=4) which suggests that the developed biosensor had good reproducibility.

The stability test of the XOs/PANI@TiO$_2$/ITO electrode was performed by storing it at 4°C in a dry environment and tracking its response to Xn (10µM) every five days. The biosensor lost about 8% of its initial activity after 45 days of use, proving that it may be kept stable for up to 40 days when kept dry and stored at 4°C **(Fig 3.5 (D)).**

### 3.3. Conclusion

An enzymatic sensor has been fabricated using PANI@TiO$_2$ nanohybrid for Xn detection specifically. Synthesized nanostructured PANI@TiO$_2$ nanohybrid proved to be an efficient conducting platform for biosensing due to its redox behaviour and the ability to mediate the reactive site and electrode surface via biomolecule. The fabricated biosensor exhibits enhanced electrochemical properties, quick response

time, and reasonable detection limit. The performance of the developed biosensor was validated with a real sample obtained from Rohu fish, and the findings show that it is capable of detecting Xn in fish meat with high reproducibility and stability.

## References

1.  El-Said, W.A., M. Abdelshakour, J.H. Choi, and J.W. Choi, *Application of Conducting Polymer Nanostructures to Electrochemical Biosensors.* Molecules, 2020. **25**(2).

2.  Rab, N., F.K. Chong, H.I. Mohamed, and W.H. Lim, *Preparation of TiO$_2$ nanoparticles by hydrolysis of TiCl$_4$ using water and glycerol solvent system.* Journal of Physics: Conference Series, 2018. **1123**: p. 012065.

3.  Paul, G., S. Verma, O. Jalil, D. Thakur, C.M. Pandey, and D. Kumar, *PEDOT: PSS-grafted graphene oxide-titanium dioxide nanohybrid-based conducting paper for glucose detection.* Polymers for Advanced Technologies, 2021. **32**(4): p. 1774-1782.

4.  Elakkiya, S., G. Arthanareeswaran, A.F. Ismail, D.B. Das, and R. Suganya, *Polyaniline coated sulfonated TiO$_2$ nanoparticles for effective application in proton conductive polymer membrane fuel cell.* European Polymer Journal, 2019. **112**: p. 696-703.

5.  Yu, H., K. Jang, I. Chung, and H. Ahn, *Fabrication and Electrochemical Characterization of Polyaniline/Titanium Oxide Nanoweb Composite Electrode for Supercapacitor Application.* Journal of Nanoscience and Nanotechnology, 2016. **16**(3): p. 2937-43.

6.  Ahmad, P.R. and P. Mondal, *Adsorption and Photodegradation of Methylene Blue by Using PAni/TiO$_2$ Nanocomposite.* Journal of Dispersion Science and Technology - J DISPER SCI TECH, 2012. **33**: p. 380-386.

7.  Rajendran, A., *MOJ Polymer Science Synthesis, Characterization and Electrical Properties of Nano Metal and Metal-Oxide Doped with Conducting Polymer Composites by in-Situ Chemical Polymerization Abbreviations: FESEM: Field Emission Scanning Electron.* MOJ Polymer Science, 2017. **1**.

8.  Emran, K., *The Electrocatalytic Activity of Polyaniline/TiO₂ Nanocomposite for Congo Red Degradation in Aqueous Solutions.* International journal of electrochemical science, 2018. **13**.

9.  Majumdar, S. and D. Mahanta, *Deposition of an ultra-thin polyaniline coating on a TiO₂ surface by vapor phase polymerization for electrochemical glucose sensing and photocatalytic degradation.* RSC Advances, 2020. **10**(30): p. 17387-17395.

10. Elgrishi, N., K.J. Rountree, B.D. McCarthy, E.S. Rountree, T.T. Eisenhart, and J.L. Dempsey, *A Practical Beginner's Guide to Cyclic Voltammetry.* Journal of Chemical Education, 2018. **95**(2): p. 197-206.

11. Abaci, S., B. Nessark, and F. Riahi, *Preparation and characterization of polyaniline+TiO2 composite films.* Ionics, 2014. **20**(12): p. 1693-1702.

12. Reddy, R., K.V. Karthik, S.B.B. Prasad, S.K. Soni, H.M. Jeong, and A.V. Raghu, *Enhanced photocatalytic activity of nanostructured titanium dioxide/polyaniline hybrid photocatalysts.* Polyhedron, 2016.

13. Dolmacı, N., S. Çete, F. Arslan, and A. Yaşar, *An amperometric biosensor for fish freshness detection from xanthine oxidase immobilized in polypyrrole-polyvinylsulphonate film.* Artificial Cells, Blood Substitutes, and Biotechnology, 2012. **40**(4): p. 275-279.

14. Narang, J., N. Malhotra, C. Singhal, and C.S. Pundir, *Impedimetric And Voltammetry Sensing Of Xanthine Using Nanocomposites.* Advanced Materials Letters, 2016. **7**: p. 555-560.

# CHAPTER 4

# POPD@g-C₃N₄-BASED BIOSENSOR FOR XANTHINE DETECTION

## 4. Introduction

This study employed a simple oxidative polymerization procedure to develop a PoPD@g-C₃N₄ nanocomposite-based metal-free biosensor. PoPD@g-C₃N₄ nanocomposite possesses robust electroactivity, high stability, huge surface area, ease of preparation, quick electron transfer-conjugation, and an interference-rejecting layer, which offers good selectivity and specificity that are highly beneficial as a substrate for XOs immobilization. The newly developed nanocomposite has successfully been utilized for accurate, metal-free sensors, enhancing signals for Xn detection. This developed material shows enhanced biosensing characteristics and provides an innovative means to evaluate the quality and freshness of fish products.
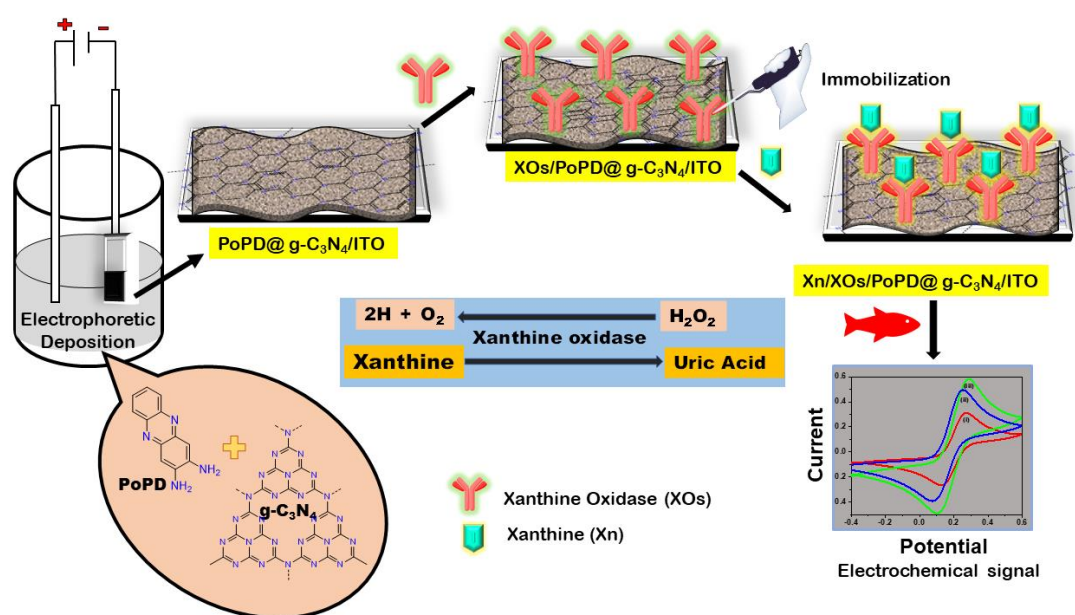


**Fig. 4.1** Scheme showing the fabrication of PoPD@g-C₃N₄ nanohybrid-based biosensor

## 4.1 Experimentation

### 4.1.1. Synthesis of g-C$_3$N$_4$

Graphitic carbon nitride (g-C$_3$N$_4$) was synthesized through the thermal condensation of melamine. Specifically, 10 g of melamine was placed in a crucible with a cover lid, and the crucible was then positioned in a muffle furnace. The temperature was raised gradually over 4 h at a rate of 5°C per minute until it reached 550°C. The resulting product after heating was collected, ground into a fine powder, and allowed to cool to room temperature.

### 4.1.2. Synthesis of PoPD

5g of the 1,2-phenylenediamine (o-PD) monomer were added to a 100 mL conical flask. Further, 25 mL of ethanol and equal water (1:1 v/v) were added to the mixture, followed by an oxidizing agent, 4 g of FeCl$_3$. Notably, the monomer underwent rapid polymerization as the solution changed from being transparent to a deep colour. The flask was then subjected to 2h of sonication at 30°C. The synthetic PoPD was extracted and repeatedly rinsed with distilled water and ethanol. The synthesized material was dried in a vacuum oven for 72 h at 70 °C to remove contaminants.

### 4.1.3. One-pot synthesis of PoPD@g-C$_3$N$_4$ nanohybrid

To synthesize the PoPD@g-C$_3$N$_4$ nanocomposite, 2.5 g of o-phenylenediamine (OPD) was dissolved by using 50 mL of DI water. The mixture was then ultrasonically treated for 30 minutes with 1.5 g of g-C$_3$N$_4$. Further, the mixture was treated with 1.75 g FeCl$_3$ and heated for 24 h at 60 °C. After cooling, ethanol and DI water were used to wash the mixture. The filtrate was vacuum dehydrated at 400 °C, forming a light brown powder.

### 4.1.4. EPD of PoPD@g-C₃N₄ nanohybrid

The PoPD@g-C$_3$N$_4$ nanohybrid was electrophoretically deposited onto a hydrolysed ITO electrode utilizing a two-electrode system, with the electrodes positioned 0.5 cm apart. Prior to deposition, the PoPD@g-C$_3$N$_4$ nanohybrid was dispersed in DI water and sonicated until the solution achieved clarity. The film was deposited at 12 V for a duration of 15 seconds.

### 4.1.5. Fabrication of PoPD@g-C₃N₄ nanohybrid-based biosensor

To fabricate the PoPD@g-C$_3$N$_4$/ITO electrode, 0.1% of glutaraldehyde was drop cast on the electrode surface and kept at room temperature for 2 h. The electrode was then covalently immobilized with XOs after being rinsed using PBS (100 mM, pH 7.4). **Fig.4.1** depicts the procedure for the synthesis of PoPD@g-C$_3$N$_4$ nanohybrid and subsequent biosensor fabrication.

## 4.2. Results and discussion

### 4.2.1. Structural and morphological studies

XRD of **(Fig.4.2 (A))** PoPD showed distinct peaks in the 2θ = 10°–30° range, demonstrating the crystalline behaviour. The peak broadness at 2θ = 26.5° shows the local crystallinity of the polymer chain [1].

Peaks at 2θ = 10.8 °, 16.5 °, 18.6 °, and 28.7° show the well-aligned morphology of the synthesized PoPD **(curve i)**. The XRD diffraction pattern of the sheets of g-C$_3$N$_4$ demonstrates a slightly intense peak at 2θ = 27.7° corresponding to the 002 plane **(curve iii)**. The two same diffraction peaks at 2θ = 27.7° were observed in the XRD pattern of g-C$_3$N$_4$ and PoPD@g-C$_3$N$_4$ and could be due to the interlayer stacking of

the g-C$_3$N$_4$. No distinct PoPD diffraction peaks are observed in the PoPD@ g-C$_3$N$_4$ sample due to the weak crystallinity and lesser content of PoPD **(curve ii)** [2].
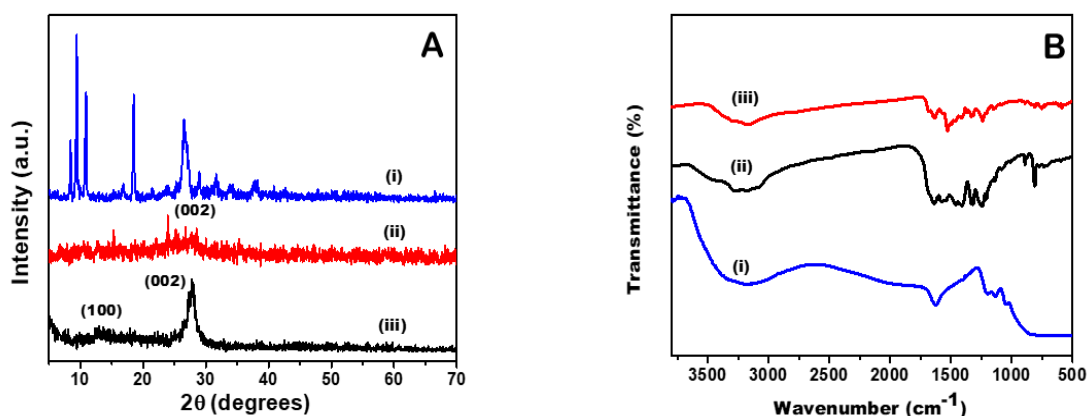


**Fig.4.2: (A)** XRD of (i) PoPD, (ii) PoPD@g-C$_3$N$_4$ nanohybrid and (iii) g-C$_3$N$_4$ nanosheets and **(B)** FT-IR spectra of (i) PoPD, (ii) g-C$_3$N$_4$ nanosheets and (iii) PoPD@g-C$_3$N$_4$ nanohybrid

FTIR of the g-C$_3$N$_4$ nanosheet **(curve ii)** exhibits a broad peak at 3164 cm$^{-1}$ **(Fig.4.2B).** Terminal NH$_2$ or NH group, peaks were observed at 1575 and 1642 cm$^{-1,}$ respectively. C = N stretching peaks for aromatic C-N stretching at 1245, 1324, and 1404 cm$^{-1}$, as well as a strong peak at 808 cm$^{-1}$ caused by the vibration of tri-s-triazine units [3, 4]. The homopolymer PoPD IR spectrum **(curve i)** showed a C=C stretching vibration peak at 1626 cm$^{-1}$, a peak for N-H stretching vibrations at 3143 cm$^{-1}$, and peaks at 1397 and 1206 cm$^{-1}$, respectively, for the quinoid and benzenoid rings C-N stretching vibrations [1, 5]. The IR spectra of PoPD@g-C$_3$N$_4$ nanocomposite **(curve iii)** are somewhat displaced to a higher or lower wavenumber than PoPD. The stretching vibration of g-C$_3$N$_4$ is assigned quite a few distinctive solid peaks in the 1700-1200 cm$^{-1}$ range. The characteristic peaks for the triazine units were seen at 820

80

and 884 cm$^{-1}$ [6]. Most of the distinct vibrational peaks of pure g-C$_3$N$_4$ are observed in PoPD@g-C$_3$N$_4$, indicating the existence of g-C$_3$N$_4$ nanosheet in the composite.

**Fig.4.3** shows the SEM image of g-C$_3$N$_4$, PoPD and PoPD@g-C$_3$N$_4$. As shown in the microscopic images of g-C$_3$N$_4$ **(Fig.4.3 (a)**), the layered morphology of g-C$_3$N$_4$ and rod-like morphology of PoPD were consistent in the PoPD@g-C$_3$N$_4$ nanocomposite **(Fig.4.3 (c))**. This observation confirms the random distribution of PoPD particles on the g-C$_3$N$_4$ sheets, providing additional evidence for the successful formation of the PoPD@g-C$_3$N$_4$ nanocomposite.
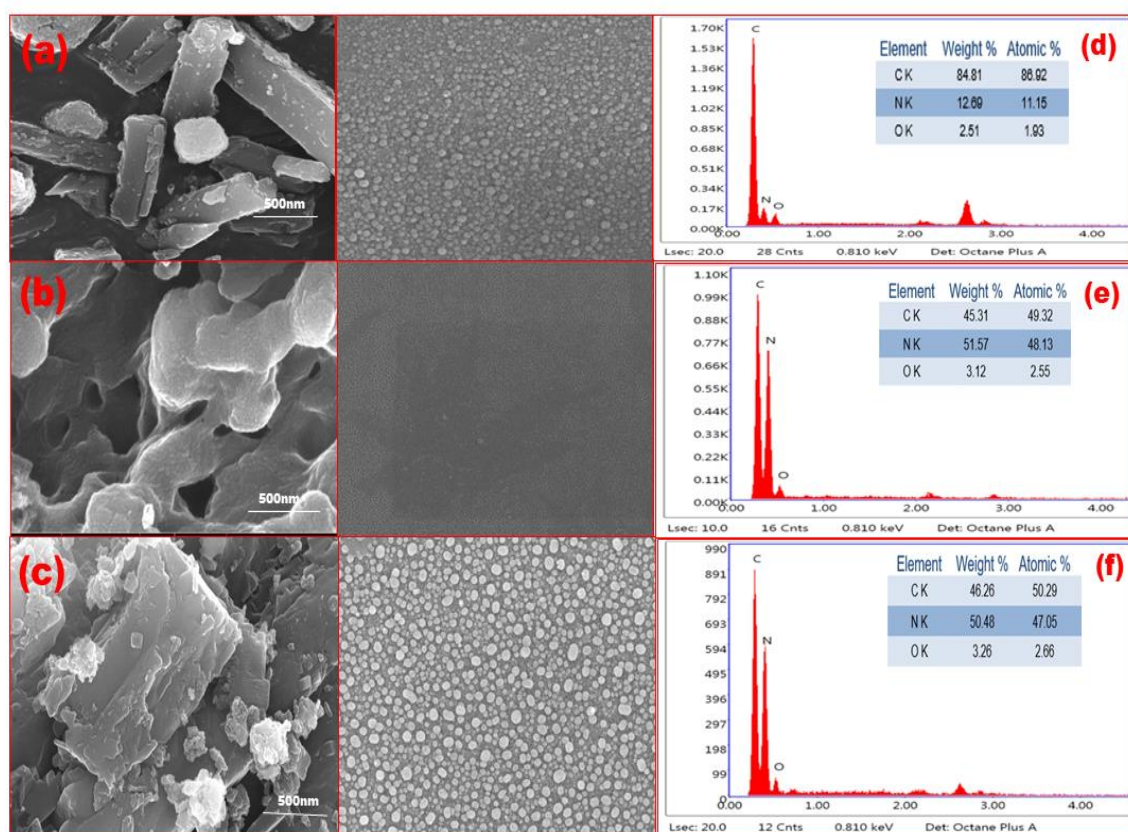


**Fig.4.3:** FESEM images (a to c) and EDAX images (d to f) for (a) g-C$_3$N$_4$, (b) PoPD and (c) PoPD@g-C$_3$N$_4$ nanohybrid

The EDAX spectra validated the loading of g-C$_3$N$_4$ in the PoPD@g-C$_3$N$_4$ framework displayed in **Fig.4.3 (d to f)**; the wt% of nitrogen content (50.58%) is higher than PoPD (12.69%) in the case of PoPD@g-C$_3$N$_4$, indicating the successful inclusion of g-C$_3$N$_4$ in PoPD

Additionally, the FESEM photographs, before and after immobilization of XOs on PoPD@g-C$_3$N$_4$/ITO, further validate the morphology change of the developed electrode **(Fig.4.4).**
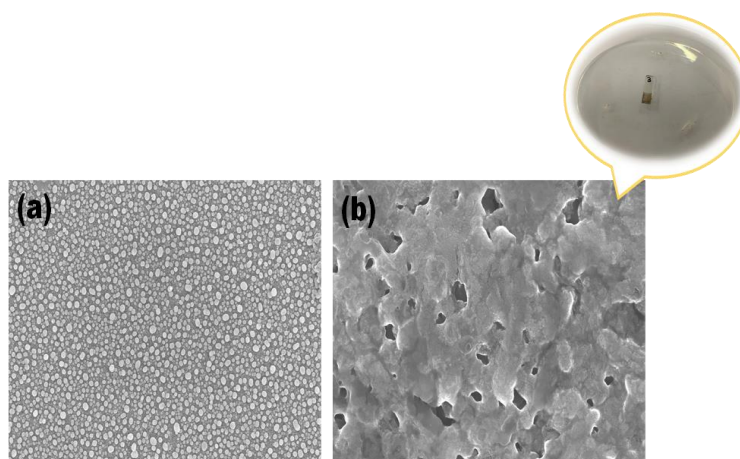


**Fig.4.4**: FESEM image of the (a) PoPD@g-C$_3$N$_4$/ITO (b) XOs/PoPD@g-C$_3$N$_4$/ITO

electrode with the real image of the fabricated electrode

**4.2.2 Electrochemical studies of the fabricated electrodes**

EIS studies **(Fig.4.5 (A))** were carried out for bare ITO, g-C$_3$N$_4$/ITO, PoPD/ITO, and PoPD@g-C$_3$N$_4$/ITO electrodes in ferro-ferri buffer. R$_{ct}$ was found to be 1081.5 Ω for the ITO electrode **(curve (i)),** while it was found to be 554.43 Ω **(curve (ii))** for the g-C$_3$N$_4$/ITO, 315.7 Ω **(curve (iii))** for the PoPD/ITO, and 285.08 Ω **(curve (iv))** for the PoPD@ g-C$_3$N$_4$/ITO electrodes. The difference in the R$_{ct}$ indicates the reduced resistance to electron transfer and the increased transfer of inter-electron charges of

PoPD@g-C$_3$N$_4$/ITO. The result shows that PoPD is compatible with the PoPD@g-C$_3$N$_4$/ITO system which benefits the g-C$_3$N$_4$ from the separation and transfer of charge carriers, generated by photons [7].

Compared to g-C$_3$N$_4$/ITO ($4.631\times10^{-5}$ A cm$^{-2}$), the PoPD@g-C$_3$N$_4$/ITO electrode has a greater $i_o$ value ($9.007\times10^{-5}$ A cm$^{-2}$). Additionally, for the PoPD@g-C$_3$N$_4$/ITO and g-C$_3$N$_4$/ITO electrodes, the values of $K_{app}$ were $0.669\times10^{-6}$ cm s$^{-1}$ and $0.381\times10^{-6}$ cm/s, respectively. Due to the synergistic interaction between PoPD and g-C$_3$N$_4$ nanosheets, which improves conductivity and electron transfer, the values of $i_o$ and $K_{app}$ **(Eq.2.8 and 2.9)** for the PoPD@g-C$_3$N$_4$/ITO electrode have increased.

**Fig.4.5 (B)** displays cyclic voltammetric results for the g-C$_3$N$_4$/ITO, PoPD/ITO, PoPD@g-C$_3$N$_4$/ITO, and XOs/PoPD@g-C$_3$N$_4$/ITO electrodes in PBS buffer. With a more significant peak current visible on the PoPD@g-C$_3$N$_4$/ITO electrode **(curve (iv); 0.58 mA)**, compared to other electrodes, (PoPD/ITO; 0.41 mA, g-C$_3$N$_4$/ITO; 0.31 mA and XOs/PoPD@g-C$_3$N$_4$/ITO; 0.49 mA), resulting in improved electron transport. Following the effective immobilization of the enzyme (XOs) on PoPD@g-C$_3$N$_4$/ITO, a clearly defined redox peak shows that the enzyme oxidation-reduction reaction at the electrode **(curve (iii)).** Based on the Randles-Sevcik equation **(Eq. 2.6)** the PoPD@g-C$_3$N$_4$/ITO electrode possesses the largest active surface area, with 0.997 cm$^2$, compared to g-C$_3$N$_4$/ITO's and PoPD/ITO's surface area, 0.930 cm$^2$ and 0.988 cm$^2$, respectively.
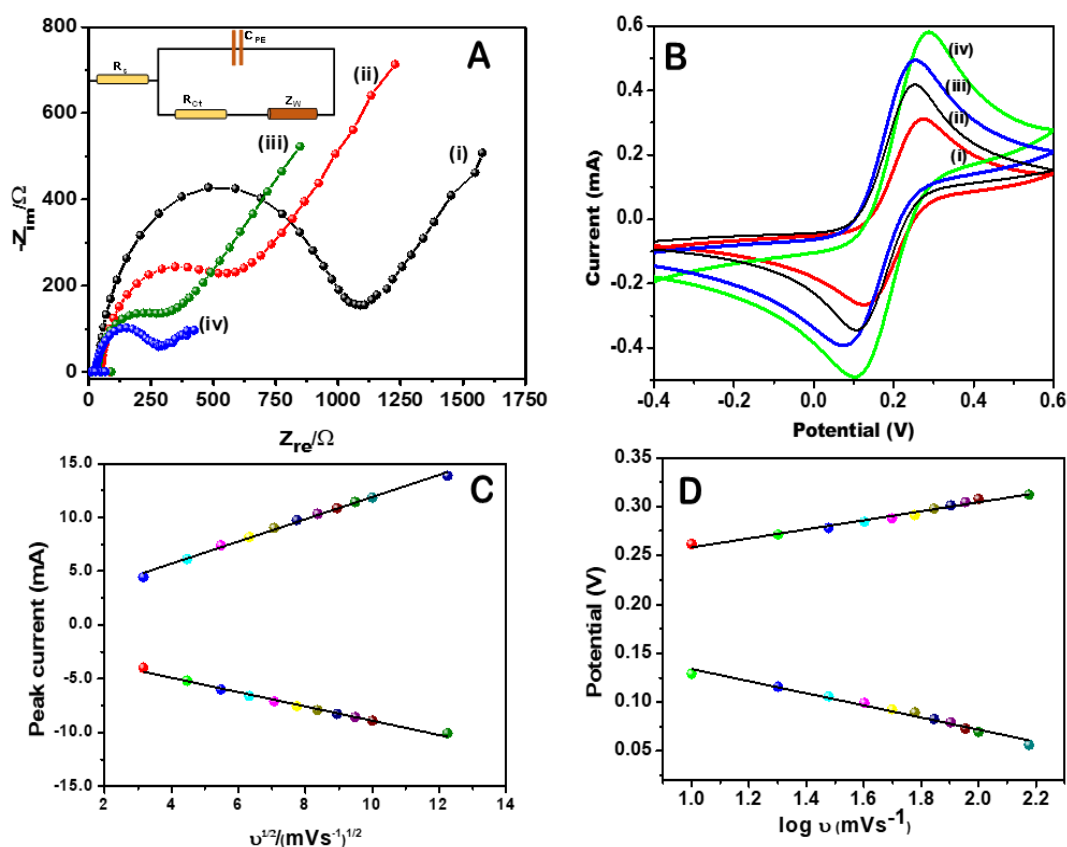
**Fig.4.5: (A)** Nyquist diagram for (i) ITO, (ii) g-C$_3$N$_4$/ITO electrode, (iii) PoPD/ITO and (iv) PoPD@g-C$_3$N$_4$/ITO electrode; **(B)** CV studies of (i) g-C$_3$N$_4$/ITO, (ii) PoPD/ITO, (iii) XOs/PoPD@g-C$_3$N$_4$/ITO and (iv) PoPD@g-C$_3$N$_4$/ITO electrode. The plots of **(C)** I$_{pa}$, I$_{pc}$ vs. square root of scan rate and **(D)** potential with log of scan rate at varying scan rate (10–150 mV) for PoPD@g-C$_3$N$_4$/ITO electrode.

The electrochemical performance of the PoPD@g-C$_3$N$_4$/ITO electrode **(Fig.4.5 C)** was studied by changing the scan rate (10 to 150 mV/s). The oxidation peak current has been observed to increase linearly in response to an increase in peak potential. With increasing scan rate, both the anodic peak current (I$_{pa}$) and the cathodic peak current (I$_{pc}$) increase linearly, as shown by equations **(4.1) and (4.2),** which illustrate

the surface adsorption-controlled process kinetics for the PoPD@g-C$_3$N$_4$/ITO electrode [8, 9].

$$Ipa(\mu A) = 1.5 \times 10^{-3} + 1.0 \times 10^{-3} \sqrt{v}\left(\frac{mV}{s}\right); \ R = 0.9973 \quad\quad (4.1)$$

$$Ipc(\mu A) = -2.25 \times 10^{-3} - 6.653 \times 10^{-4} \sqrt{v}\left(\frac{mV}{s}\right); R = 0.9941 \quad\quad (4.2)$$

In a similar manner, a linear correlation was observed between the anodic peak potential (E$_{pa}$) and cathodic peak potential (E$_{pc}$) with the natural logarithm of the scan rate (ln υ). Eqs (**4.3) & (4.4)** represent the corresponding linear regression equations illustrating the same **(Fig. 4.5 (D)).**

$$Epa(V) = 0.212 \ln(v) + 0.046 \ ; R = 0.9896 \quad\quad (4.3)$$

$$Epc(V) = 0.196 \ ln(v) - 0.062 \ ; R = 0.9903 \quad\quad (4.4)$$

At a scan rate (v) of 50 mV/s, the heterogeneous electron transfer coefficient (K$_s$) and charge transfer coefficient ($\alpha$) for the PoPD@g-C$_3$N$_4$/ITO electrode calculated were to be, 2.3859 s$^{-1}$ and 0.9105 using Laviron's equation **(Eq.2.5)** [8].
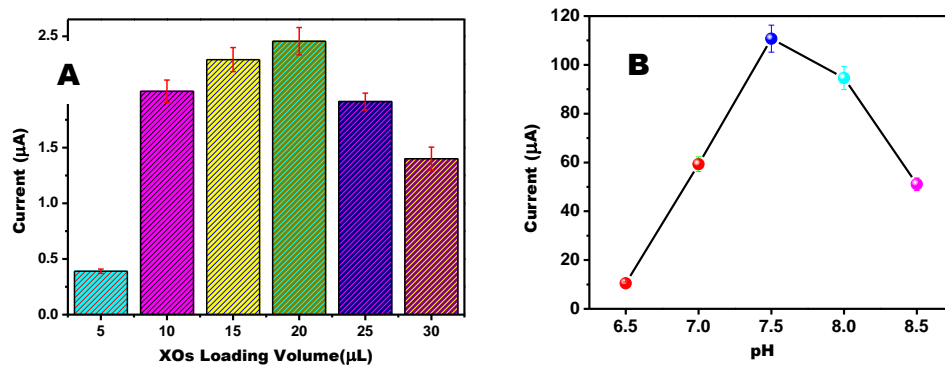


**Fig. 4.6 (A)** Optimization of the loading volume of the enzyme (XOs) on PoPD@g-C$_3$N$_4$/ITO and **(B)** Optimization of the pH condition for efficient detection of Xn

**Fig. 4.6 (A)** illustrates the relationship between the current response of Xn (0.1 μL) and the loading volume of XOs (5 μL to 30 μL). Initially, the peak current was increased to 20 μL, but as the volume of XOs was further loaded, the current response was reduced. Thus, 20 μL of XOs as loading volume was taken for further experiments.

In **Fig.4.6 (B)**, various electrolytic solutions having a 6.5 to 8.5 pH range have been taken to investigate the performance of the Xn/XOs/PoPD@g-C$_3$N$_4$/ITO electrode**.** In particular, the maximal current response was measured in PBS buffer with 5mM of Fe[CN$_6$]$^{3-/4-}$ at a pH of 7.5. Therefore, the optimal pH for the electrochemical detection of Xn has been determined to be pH 7.5.

## 4.2.3 Electrochemical biosensing response of XOs/PoPD@g-C$_3$N$_4$/ITO electrode

**Fig.4.7 (A)** shows the variable Xn concentrations (0.001–1μM) for the electrochemical biosensing response of the XOs/PoPD@g–C$_3$N$_4$/ITO electrode. **Fig. 4.7 (B),** the current response was linearly increased from 0.001 to 1μM, supporting the efficient functioning and strong electrocatalytic properties of the PoPD@g-C$_3$N$_4$ nanocomposite for Xn detection. The regression equation: y = 48.403×10$^{-6}$ x + 0.5798×10$^{-6}$ (y = peak current and x = concentration of Xn) has sensitivity around 0.5798 μAM$^{-1}$, having $R^2$ = 0.9217. The LOD was determined to be 1 nM for the developed PoPD@g-C$_3$N$_4$ nanocomposite-based sensor.
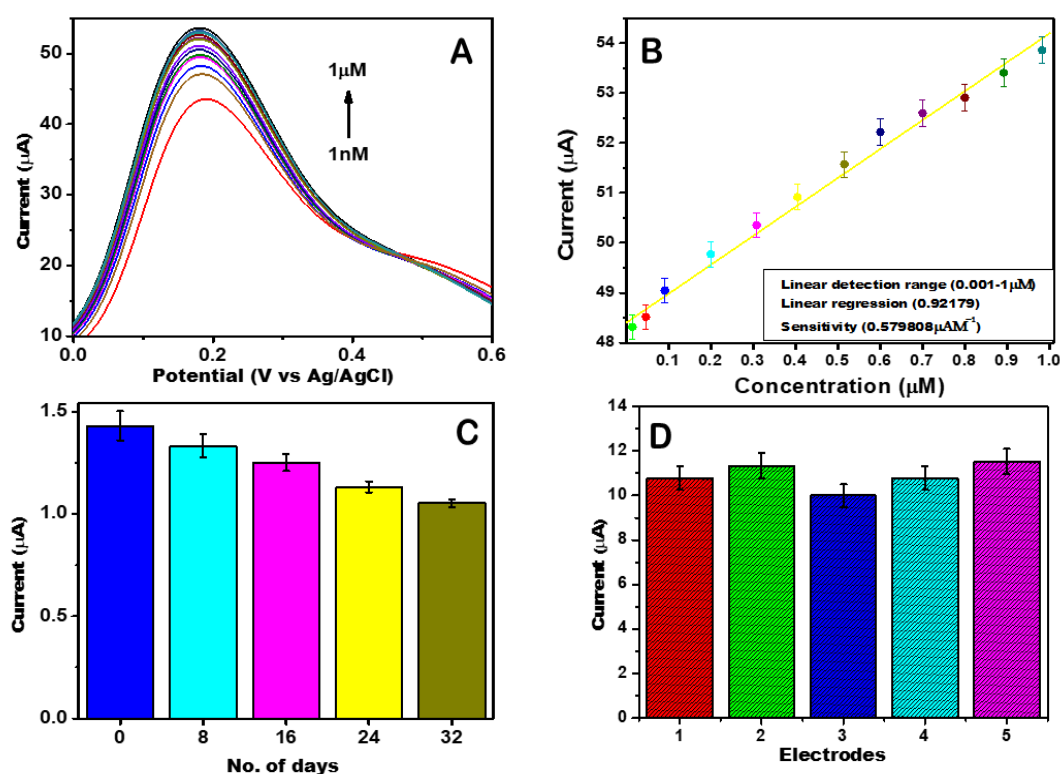
**Fig.4.7 (A)** DPV studies indicating the XOs/PoPD@g-C$_3$N$_4$/ITO electrode's response to Xn concentrations ranging from 0.001-1µM; **(B)** Calibration plot demonstrating a linear relationship between Xn concentration and the magnitudes of recorded current; **(C)** Test of the shelf life for the sensor lasting upto 4 weeks and **(D)** Five-electrode reproducibility study

### 4.2.3. Validating the biosensor with real samples

The Differential Pulse Voltammetry (DPV) analysis of the XOs/PoPD@g-C$_3$N$_4$-based biosensor revealed a consistent increase in peak current with the rise in Xn concentration within the range of 0.001-1 µM. These findings demonstrated a remarkable similarity to the synthetic Xn samples. Xn samples and show that the developed biosensor has the lowest LOD for detecting Xn in real fish meat samples.

### 4.2.4. Shelf life and reproducibility

To monitor the shelf life of XOs/PoPD@g-C$_3$N$_4$/ITO against Xn (1 µM), five similar electrodes were prepared. The electrochemical result shows that the biosensor is stable at 4°C in a dry state for at least 4 weeks. Compared to the initial electrode's current response, it only lost 0.4 µA current (**Fig. 4.7 (C))**.

Five parallel electrodes were also prepared to examine the resulting electrochemical sensor's repeatability. The newly constructed electrochemical sensor has good repeatability, as evidenced by the 5.9% relative standard deviation that was found using **Fig.4.7 (D))**.

### 4.2.5 Storage, Specificity and Selectivity

**Fig.4.8 (A)** shows the assessment of the level of Xn in fish extract stored for a specific amount of time (0 to 5 days) at RT, and it shows 32 times increased current response compared to day one.

The biosensor's interference test was carried out by exposing the XOs/PoPD@g-C$_3$N$_4$/ITO electrode to a range of interfering analytes having 10 folds greater concentration than Xn, including urea, glucose, ascorbic acid, uric acid, and sodium benzoate. And, the presence of a selective current response was observed for each analyte, demonstrating that the biosensor is selective for Xn detection. The specificity analysis was also conducted, and we noticed that Xn kept its specificity even when mixed with different analytes, so we tested the biosensor for 10 times excess of the concentration of all the analytes **(Fig.4.8 (B))**.
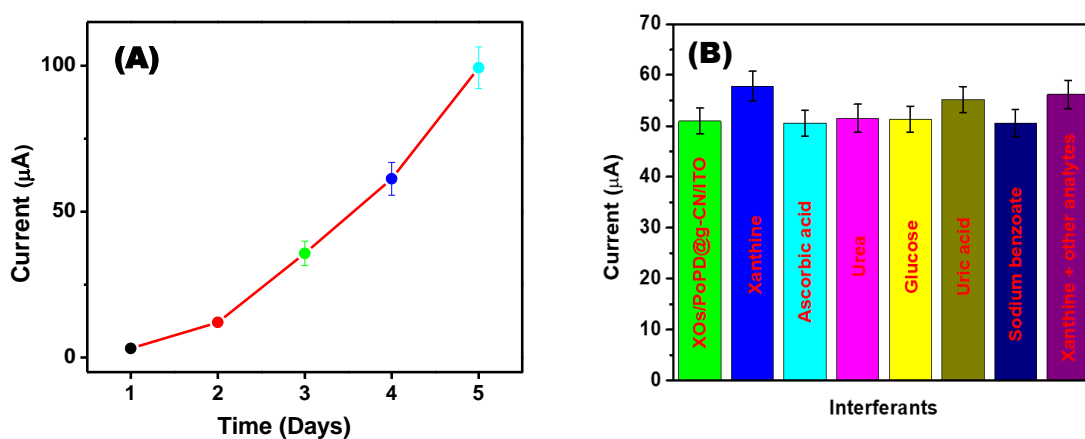
**Fig.4.8: (A)** Increase in xanthine concentration as a function of days measured using fabricated biosensor and **(B)** Interference studies of the PoPD@g-C₃N₄/ITO electrodes with other plausible interfering species

The responses to uric acid and urea were slightly higher than before. In contrast, the response patterns to sodium benzoate, glucose and ascorbic acid were comparatively identical, revealing a relative inaccuracy in the analyte's determination of roughly ± 5% Tolerance limit expressed in **Table 4.1**. Therefore, XOs/PoPD@g-C₃N₄/ITO is considered a suitable biosensor for Xn recognition.

**Table 4.1:** Tolerance limit table for plausible endogenous analytes

| S.No. | Analytes | (Change in current response) Tolerance limit (%) |
|-------|----------|---------------------------------------------------|
| 1 | Ascorbic acid | ± 0.5 |
| 2 | Sodium benzoate | ± 1.3 |
| 3 | Glucose | ± 1.9 |
| 4 | Urea | ± 4.9 |
| 5 | Uric acid | ± 4.5 |

## 4.3 Conclusion

The current work uses a simple oxidative polymerization method to develop a stable binary PoPD@g-C$_3$N$_4$ nanocomposite. Numerous spectroscopic and morphological methods have been employed to confirm that PoPD@g-C$_3$N$_4$ was successfully formed. It is promising to employ a PoPD@g-C$_3$N$_4$ electrode for the immobilization of XOs due to an increase in electron transfer values when compared to bare PoPD and g-C$_3$N$_4$ electrodes. With a LOD around 1 nM (S/N = 3), the noble XOs/PoPD@g-C$_3$N$_4$/ITO electrode successfully detected Xn in real fish samples. The created biosensing electrode also has an adequate level of stability, repeatability, and anti-interference properties. It also has a very low detection limit. As a result, a biosensor based on PoPD@g-C$_3$N$_4$ nanocomposite has shown to be an effective platform for Xn monitoring.

# References

1.  Wang, Z., F. Liao, S. Yang, and T. Guo, *A Novel Route Synthesis of Poly(ortho-phenylenediamine) Fluffy Microspheres Self-assembled from Nanospheres.* Fibers and Polymers, 2011. **12**.

2.  Rashidizadeh, A., H. Ghafuri, H.R.E. Zand, and N. Goodarzi, *Graphitic Carbon Nitride Nanosheets Covalently Functionalized with Biocompatible Vitamin B1: Synthesis, Characterization, and Its Superior Performance for Synthesis of Quinoxalines.* ACS Omega, 2019. **4**(7): p. 12544-12554.

3.  Fahimirad, B., A. Asghari, and M. Rajabi, *Magnetic graphitic carbon nitride nanoparticles covalently modified with an ethylenediamine for dispersive solid-phase extraction of lead(II) and cadmium(II) prior to their quantitation by FAAS.* Microchimica Acta, 2017. **184**.

4.  Elshafie, M., S.A. Younis, P.Serp, and E.A.M Gad, *Preparation characterization and non-isothermal decomposition kinetics of different carbon nitride sheets.* Egyptian Journal of Petroleum, 2019. **29**.

5.  Pandian, P., A. Manikandan, E. Manikandan, K. Pandian, M.K. Moodley, K. Roro, and K. Murugan, *Solid-State Synthesis of POPD@AgNPs Nanocomposites for Electrochemical Sensors.* Journal of Nanoscience and Nanotechnology, 2018. **18**: p. 3991-3999.

6.  Pareek, S. and J. Quamara, *Dielectric and optical properties of graphitic carbon nitride–titanium dioxide nanocomposite with enhanced charge seperation.* Journal of Materials Science, 2018. **53**.

7.  Chen, X., L. Liu, Y. Zhao, J. Zhang, D. Li, B. Hu, and X. Hai, *A Novel Metal-Free Polymer-Based POPD/g-$C_3N_4$ Photocatalyst with Enhanced Charge Carrier Separation for the Degradation of Tetracycline Hydrochloride.* 2017. **2**(29): p. 9256-9260.

8.    Laviron, E., *General expression of the linear potential sweep voltammogram in the case of diffusionless electrochemical systems.* Journal of Electroanalytical Chemistry and Interfacial Electrochemistry, 1979. **101**(1): p. 19-28.

9.    Elgrishi, N., K.J. Rountree, B.D. McCarthy, E.S. Rountree, T.T. Eisenhart, and J.L. Dempsey, *A Practical Beginner's Guide to Cyclic Voltammetry.* Journal of Chemical Education, 2018. **95**(2): p. 197-206.

# CHAPTER 5

# TIO$_2$ DOPED g-C$_3$N$_4$@POPD-BASED BIOSENSOR FOR XANTHINE DETECTION

## 5. Introduction

A stable binary nanocomposite composed of g-C$_3$N$_4$@PoPD-TiO$_2$ was successfully synthesized using oxidative polymerization method. The nanocomposite was used to fabricate biosensing electrodes to support the XOs enzyme. The modification of the electrode with g-C$_3$N$_4$ nanosheets, further enhanced by PoPD which proves to be a highly effective platform for immobilizing XOs. Many electrochemical biosensors for Xn detection often employ active metal catalysts to enhance the electroactive surface, improve charge-transfer efficiency, and provide better surface functionality for immobilizing enzymes. Therefore, the efficiency of various TiO$_2$ ratios on g-C$_3$N$_4$@PoPD-based electrodes has been examined and the results have been discussed in the chapter.
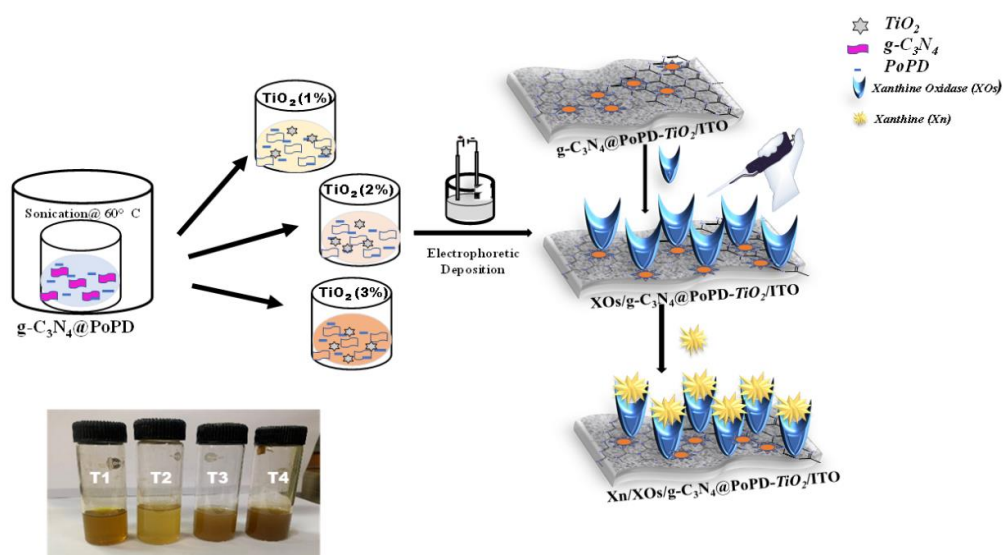


**Fig.5.1** Schematic representation of the developed g-C$_3$N$_4$ @PoPD-TiO$_2$ (1%, 2% and 3% ) based biosensor

## 5.1 Experimentation

### 5.1.1. Synthesis of g-C$_3$N$_4$

Graphitic carbon nitride (g-C$_3$N$_4$) was synthesized by thermally condensing melamine. In a typical procedure, 10g of melamine was mixed with a crucible with a lid. The crucible was then heated at a rate of 5°C min$^{-1}$ in the muffle furnace for 4 h to 550°C. The material was then collected, reduced to powder, and cooled to room temperature.

### 5.1.2. Synthesis of PoPD

In a 100 mL conical flask, 5 g of 1,2-phenylenediamine (o-PD) monomer was added to a mixture of ethanol and water (1:1 v/v, 25 mL) . 4 g of FeCl$_3$ was introduced into the reaction mixture to act as an oxidant. The solution underwent a noticeable colour change from transparent to brown, indicating the occurrence of polymerization. Throughout the process, the temperature was carefully maintained at 30°C, and the flask was subjected to sonication. The synthesized PoPD was then collected and thoroughly cleaned with distilled water/ethanol to get rid of any remaining impurities. The material was dehydrated in a vacuum oven for 72 h at 70°C to remove water and other contaminants.

### 5.1.3. One-pot synthesis of g-C$_3$N$_4$@PoPD nanohybrid with TiO$_2$ doping

The g-C$_3$N$_4$@PoPD nanocomposite was synthesized using a multistep procedure. Firstly, in 50 mL of deionized (DI) water 2.5 g of o-phenylenediamine (oPD) was dispersed and subjected to ultrasonication. After adding 1.5 g of g-C$_3$N$_4$ to the solution, the mixture was further ultrasonicated for half an hour. For the observation of the doping response, TiO$_2$ was successively added to three different beakers

containing the same g-C$_3$N$_4$@PoPD suspension at three different ratios i.e., 0.05 g (T1), 0.1 g (T2), and 0.5 g (T3). All solutions were then heated for 24h at 60°C with 1.75 g of FeCl$_3$. The mixtures were then allowed to cool, and the resulting product was rinsed with DI water. The obtained filtrate was vacuum dehydrated, and heated to 400°C.

### 5.1.4. Electrophoretic deposition (EPD)

All three synthesized ratios (T1,T2, and T3), PoPD/ITO and g-C$_3$N$_4$@PoPD/ITO nanohybrid, were electrophoretically deposited onto a hydrolyzed ITO electrode. The distance between the two electrodes was set to 0.5 cm apart. Prior to deposition, all five suspensions were sonicated in DI water to make a transparent solution followed by 10 mL of the solution was diluted with 5 mL of ethanol. The films were deposited for 15 seconds at a voltage of 12 V.

### 5.1.5. Fabrication of the biosensor

The fabricated electrodes were exposed to 0.1% glutaraldehyde and left for 2h at room temperature. The electrodes were then immobilized with XOs (20μL) and rinsed with PBS (100 mM, pH 7.4). **Fig.5.1** depicts the process for creating the electrode.

## 5.2 Results & discussion

### 5.2.1. Structural and morphological studies

The XRD patterns for the following substances are shown in **Fig.5.2 :**g-C$_3$N$_4$, PoPD, g-C$_3$N$_4$@PoPD/ITO, g-C$_3$N$_4$@PoPD-T1, g-C$_3$N$_4$@PoPD-T2, and g-C$_3$N$_4$@PoPD-T3. The g-C$_3$N$_4$ sheets diffraction pattern **(curve i)** shows a strong peak at $2\theta = 27.7°$, which is indexed to the (002) plane, while the PoPD polymer's diffraction pattern **(curve ii)** exhibits prominent peaks in the range of $2\theta = 10°–30°$, supporting the

polymer's crystallinity [1]. XRD of g-$C_3N_4$ **(curve i)** and g-$C_3N_4$@PoPD **(curve iii)**, shows one identical diffraction peak at 27.7° which is attributed to the distinctive (002) plane and the graphitic structure of g-$C_3N_4$. PoPD hasn't shown any peak in the g-$C_3N_4$@PoPD nanohybrid because of its misalignment.
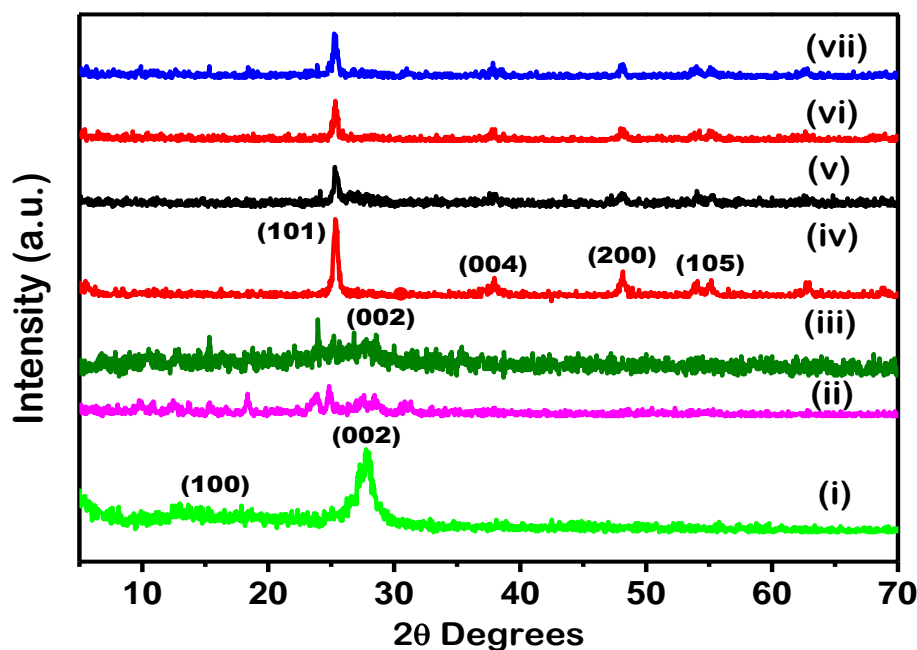


**Fig.5.2** XRD of **(i)** g-$C_3N_4$, **(ii)** PoPD, **(iii)** g-$C_3N_4$@PoPD, **(iv)** $TiO_2$ anatase, **(v)** g-$C_3N_4$@PoPD-$TiO_2$ (1%), **(vi)** g-$C_3N_4$@PoPD-$TiO_2$ (2%) and **(vii)** g-$C_3N_4$@PoPD-$TiO_2$ (3%)

However, the characteristic peaks at 25.5˚, 38.14˚, and 48.09˚ corresponded to the 101, 004, and 200 planes, respectively, confirming the anatase form of $TiO_2$ particles **(curve iv).** Additionally, the pattern for the g-$C_3N_4$@PoPD-T1/T2/T3 nanohybrids **(curve v, vi, vii)** was identical to that of $TiO_2$ **(curve iv)**. It did not reflect any typical peaks of the g-$C_3N_4$ & PoPD, which may be due to the highly aligned morphology of $TiO_2$ [2].
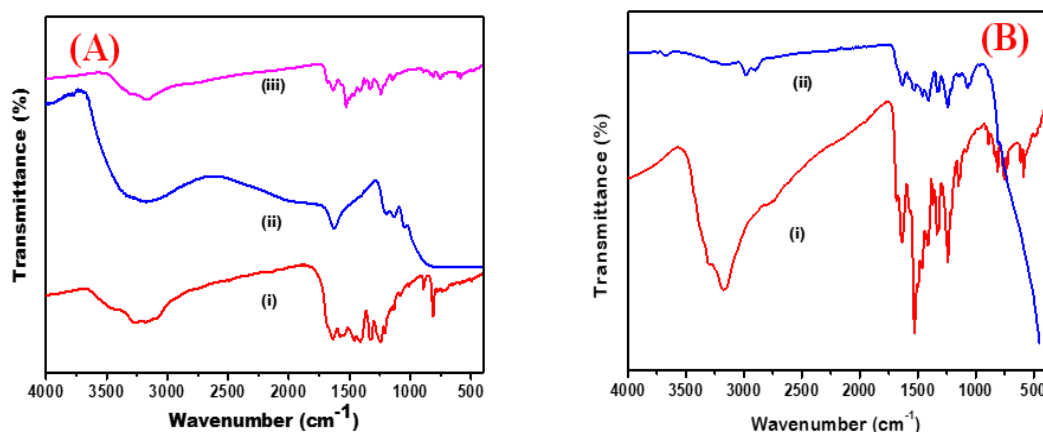
**Fig.5.3** FTIR spectra of **(A)** (i) PoPD, (ii) g-C$_3$N$_4$ and (iii) g-C$_3$N$_4$@PoPD; **(B)** (i) g-C$_3$N$_4$ @PoPD and (ii) g-C$_3$N$_4$@PoPD-TiO$_2$

The g-C$_3$N$_4$ nanosheet displays broad NH$_2$ or NH stretching peaks at 3164 cm$^{-1}$, aromatic C-N stretching peaks at 1245, 1324, and 1404 cm$^{-1}$, a sharp rise at 808 cm$^{-1}$ due to the vibration of tri-s-triazine units, and C = N stretching peaks at 1575 and 1642 cm$^{-1}$ **(Fig.5.3 (A))**. The N-H stretching vibration peak was visible in the homopolymer PoPD's IR spectrum at 3143 cm$^{-1}$, while C=C and C-N stretching vibration peaks were visible at 1626 and 1561 cm$^{-1}$ for the quinoid and benzenoid rings, respectively. Compared with PoPD, the FTIR peaks in the g-C$_3$N$_4$@PoPD nanocomposite are marginally shifted to a higher or lower wavenumber **(Fig.5.3 (B))**. The stretching vibration of g-C$_3$N$_4$ is attributed to several distinctive solid peaks in the 1700–1200 cm$^{-1}$ region. However, the triazine units are responsible for the distinctive peaks at 820 and 884 cm$^{-1}$. g-C$_3$N$_4$@PoPD exhibits the majority of the distinctive vibrational peaks of g-C$_3$N$_4$, demonstrating the presence of a g-C$_3$N$_4$ nanosheet in the composite [3, 4].
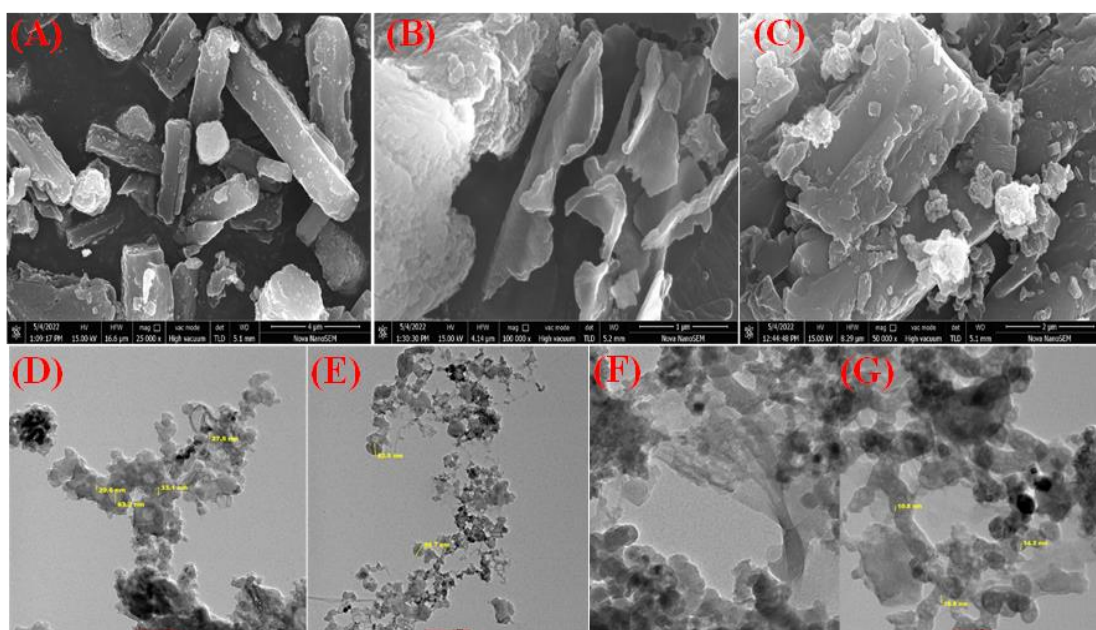
**Fig.5.4** SEM images of **(A)** PoPD; **(B)** g-C₃N₄; **(C)** g-C₃N₄@PoPD and TEM images

of **(D)** PoPD; **(E)** g-C₃N₄ ; **(F)** g-C₃N₄@PoPD and **(G)** g-C₃N₄@PoPD-T1

**Fig.5.4** displays the FE-SEM images of the PoPD/ITO, g-C$_3$N$_4$/ITO, and PoPD@g-C$_3$N$_4$/ITO electrodes. The FE-SEM images of PoPD@g-C$_3$N$_4$/ITO shows a clear difference in morphology before and after the impregnation, demonstrating the adsorption of g-C$_3$N$_4$ on PoPD. And TEM results show that all the particles are in nano-ranged size even after composite formation.

### 5.2.2.Electrochemical analysis for the fabricated electrodes

**Fig.5.5 (A)**, shows the result of electrochemical impedance spectroscopy of PoPD/ITO, g-C$_3$N$_4$@PoPD/ITO, g-C$_3$N$_4$@PoPD-T2/ITO, g-C$_3$N$_4$@PoPD-T3/ITO and g-C$_3$N$_4$@PoPD-T1/ITO electrodes (PBS having 5 mM of $[Fe(CN)_6]^{3-/4}$ . The estimated R$_{ct}$ was 411.53 Ω for the *PoPD* electrode **(curve i),** while it turned out to be 146.68 Ω, 218.98  Ω, 333.97 Ω and 108.55 Ω for the g-C$_3$N$_4$@PoPD **(curve ii),** g-C$_3$N$_4$@PoPD-

T2 **(curve iii)**, g-C$_3$N$_4$@PoPD-T3 **(curve iv)** and g-C$_3$N$_4$@PoPD-T1 **(curve v)** electrodes, respectively. The semicircular Nyquist plot's substantially reduced diameter demonstrates the g-C$_3$N$_4$@PoPD-T1 **(curve v)** electrode's decreased the electron transfer resistance and higher interfacial charge transfer. The outcome demonstrates that 1wt% of TiO$_2$ is compatible with the g-C$_3$N$_4$@PoPD system and benefits the separation and transfer of photogenerated charge carriers [5].
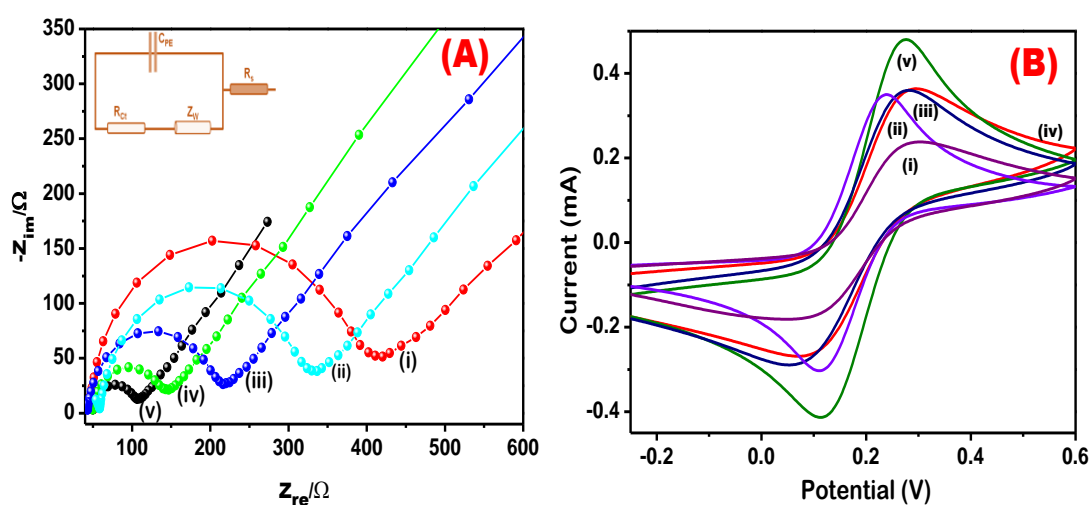


**Fig.5.5 (A)** Nyquist diagram for (i) PoPD, (ii) g-C$_3$N$_4$@PoPD, (iii) g-C$_3$N$_4$@PoPD-T2, (iv) g-C$_3$N$_4$@PoPD-T3 and (v) g-C$_3$N$_4$@ PoPD-T1 electrode; **(B)** CV studies of (i) PoPD, (ii) g-C$_3$N$_4$@PoPD, (iii) g-C$_3$N$_4$@g-C$_3$N$_4$@PoPD-T2, (iv) g-C$_3$N$_4$@PoPD-T3 and (v) g-C$_3$N$_4$@ PoPD-T1 electrode

Based on the estimated R$_{ct}$ values, electron-transfer kinetics have been used to study electrochemical electrode processes. Compared with g-C$_3$N$_4$@PoPD (17.50 $\times 10^{-5}$ A cm$^{-2}$), g-C$_3$N$_4$@PoPD-T1 electrode has a larger i$_o$ value (23.65 $\times$ 10$^{-5}$ A cm$^{-2}$) than the latter. Additionally, for the g-C$_3$N$_4$@PoPD, g-C$_3$N$_4$@PoPD-T1 electrodes, the values of K$_{app}$ were 1.44 $\times$ 10$^{-6}$ cm s$^{-1}$ and 1.95$\times$10$^{-6}$ cm s$^{-1}$, respectively. The synergistic interaction between g-

$C_3N_4$@PoPD and $TiO_2$, improves conductivity and electron transfer, consequently, the values of $i_o$ and $K_{app}$ for the g-$C_3N_4$@PoPD-T1 electrode have increased.

**Fig.5.5 (B)** displays CV results for the (i) PoPD/ITO, (ii) g-$C_3N_4$@ PoPD/ITO, (iii) g-$C_3N_4$@PoPD-T2/ITO, (iv) g-$C_3N_4$@PoPD-T3/ITO and (v) g-$C_3N_4$@PoPD-T1/ITO electrodes in PBS buffer. The g-$C_3N_4$@PoPD-T1/ITO electrode showed a distinct pair of redox peaks with a higher peak current (curve (v); 0.48 mA) in comparison to other electrodes (PoPD/ITO; 0.23mA), (g-$C_3N_4$@PoPD/ITO; 0.34mA), (g-$C_3N_4$@PoPD-T2/ITO; 0.36mA), and g-$C_3N_4$@PoPD-T3/ITO; 0.37mA). The increased peak current of g-$C_3N_4$@PoPD-T1/ITO, indicates that the $TiO_2$ and g-$C_3N_4$@PoPD exhibit a beneficial synergy to produce more redox sites for the probe and improves the electron transport. The electroactive surface areas of the g-$C_3N_4$@PoPD-T1/ITO electrode was calculated using the Randles-Sevcik equation **(Eq.2.6).** The g-$C_3N_4$@PoPD-T1/ITO demonstrates a notably larger active surface area of 0.999 cm$^2$, in contrast to 0.998 cm$^2$ observed for g-$C_3N_4$@PoPD/ITO. This increased electroactive surface area is anticipated to provide significant advantages for electroanalysis.

The performance of the g-$C_3N_4$@PoPD-T1/ITO **(Fig.5.6 (A))** was examined by varying the scan rate (10 to 150 mV/s). An upward shift in the peak potential causes the oxidation peak current to rise linearly. Equations **(5.1)** and **(5.2)**, which represent the surface adsorption-controlled process kinetics for the g-$C_3N_4$@PoPD-T1/ITO electrode, illustrate that both the anodic peak current ($I_{pa}$) and the cathodic peak current ($I_{pc}$) increase linearly with increasing scan rate **Fig.5.6 (B))** [6, 7].

$$Ipa(\mu A) = 56.3 \times 10^{-3} + 63.7 \times 10^{-3}\sqrt{v}\left(\frac{mV}{s}\right); R = 0.9978 \qquad \textbf{(5.1)}$$

$$Ipc(\mu A) = -100.2 \times 10^{-3} - 45.41 \times 10^{-3}\sqrt{v}\left(\frac{mV}{s}\right); R = 0.9945 \qquad \textbf{(5.2)}$$

he natural logarithm of the scan rate (ln υ) and the anodic and cathodic peak potentials ($E_{pa}$ & $E_{pc}$) both displayed a linear relationship. **Fig.5.6 (C)** shows the relevance of the linear regression equations, **Eqs.(5.3) & (5.4)**.

$$Epa(V) = 0.033\ln(v) + 0.196 \, ; R = 0.94524 \tag{5.3}$$

$$Epc(V) = -0.053\,ln(v) + 0.176; R = -0.99612 \tag{5.4}$$
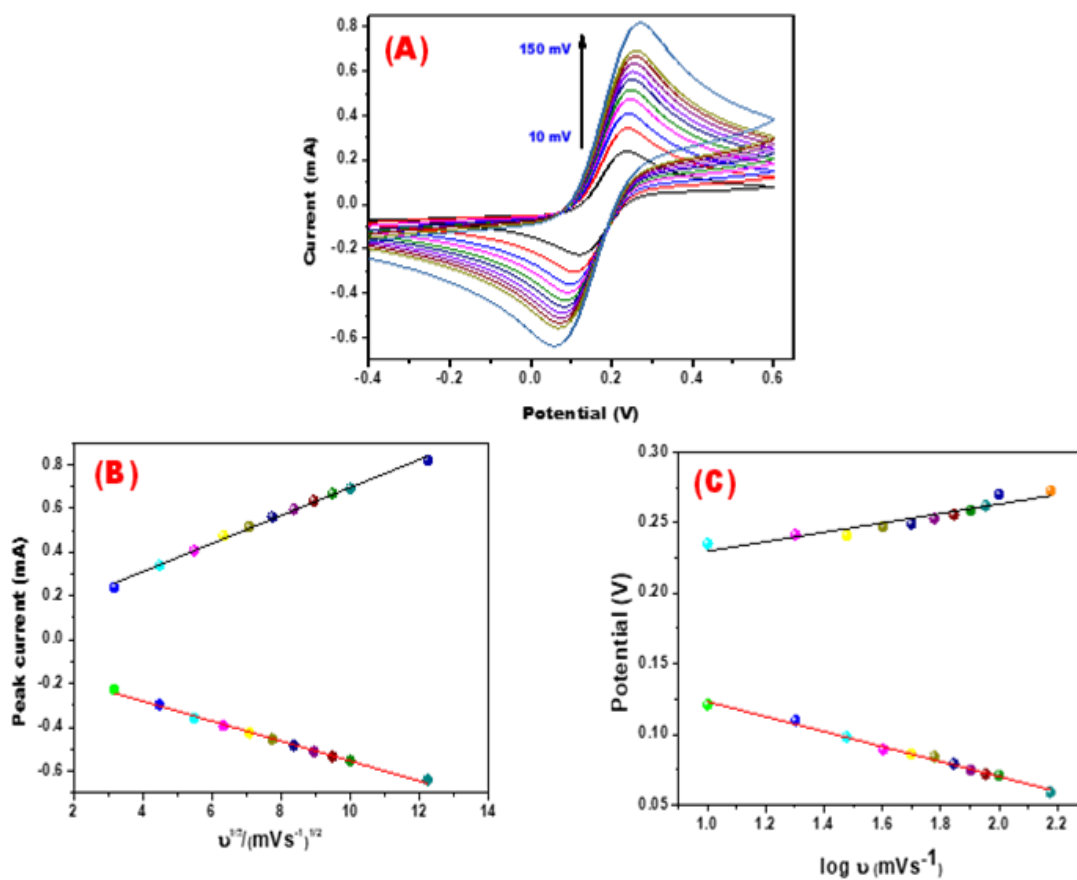


**Fig.5.6 (A)** Cyclic voltammogram of g-$C_3N_4$@PoPD-T1 /ITO at different scan rates (10-150mV); **(B)** The plots illustrating Ipa, Ipc against the square root of the scan rate, and **(C)** potential plotted against the logarithm of the scan rate, were generated with varying scan rates for the g-$C_3N_4$@PoPD-T1 /ITO electrode.

The charge transfer coefficient (α) and the heterogeneous electron transfer coefficient ($K_s$) of the g-C$_3$N$_4$@PoPD-T1/ITO electrode was calculated as 0.9067 and 0.03463s$^{-1}$, respectively, using Laviron's equation at a scan rate (υ) of 50 mV/s **(Eq. 2.5).**

### 5.2.3. Electrochemical biosensing response of XOs/g-C₃N₄@PoPD-T1/ITO electrode
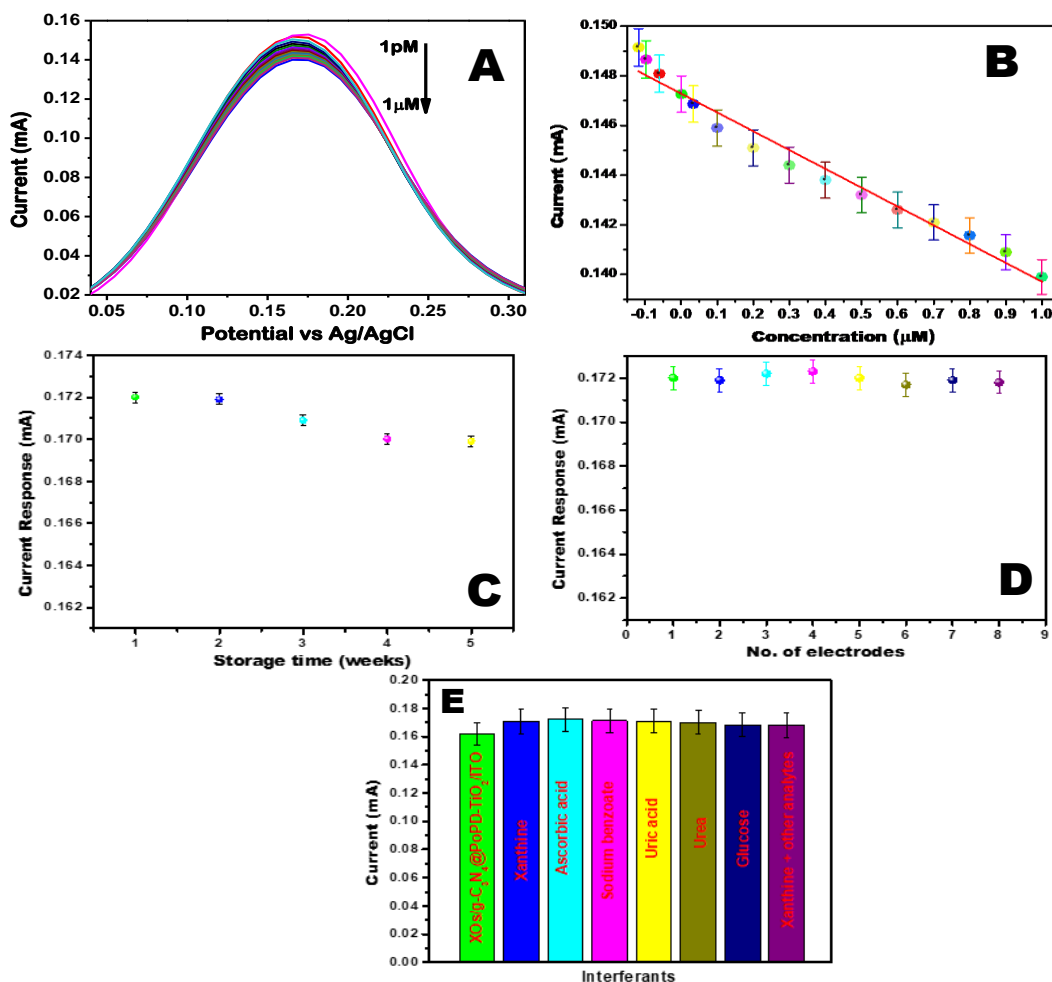


**Fig.5.7 (A)** Biosensing response of the XOs/g-C$_3$N$_4$@PoPD-T1/ITO electrode with increasing concentration of Xn (1pM-1µM); **(B)** Calibration plot displaying a linear correlation between the current and the concentration of Xn; **(C)** Shelf-life tests of the sensor up to five weeks; **(D)** Reproducibility study at nine modified electrodes and **(E)** Interference studies of the XOs/g-C$_3$N$_4$@PoPD-TiO$_2$/ITO electrodes with other analytes

**Fig.5.7 (A)** shows the variable Xn concentrations (1μM-1pM) used for electrochemical biosensing response investigation for the XOs/g-C$_3$N$_4$@PoPD-T1/ITO electrode. The peak current response linearly decreased from 1pM to 1μM **(Fig.5.7 (B))**, supporting the efficient functioning and strong electrocatalytic properties of the PoPD@g-C$_3$N$_4$@PoPD-T1 nanocomposite for Xn detection. The regression equation: **y = 7.575 ×10$^{-3}$ x + 0.147** (y = peak current and x = concentration of Xn) having R$^2$ = **0.9705**, has sensitivity around **7575.09 mA μM$^{-1}$ cm$^{-2}$**. The LOD was determined to be 0.1 pM for the developed g-C$_3$N$_4$@PoPD-T1/ITO nanocomposite-based sensor.

### 5.2.4. Validation of the biosensor with real sample

Using DPV, the developed XOs/g-C$_3$N$_4$@PoPD-T1-based biosensor has been examined for Xn samples from real fish meat [8]. The DPV analysis demonstrates that the peak current continuously increases as Xn concentration rises from 0.01-1μM. These outcomes comparably match to those of the synthetic Xn samples, showing that the developed biosensor has the lowest LOD for detecting Xn in fish meat samples.

### 5.2.5 Shelf life, reproducibility and specificity

Five same electrodes were prepared to monitor the shelf life of XOs/g-C$_3$N$_4$@PoPD-T1 against Xn (1 μM). The result shows that the biosensor is stable at 4°C in a dry state for at least 5 weeks. Compared to the initial electrode's current response, it only lost 0.2 μA current (**Fig. 5.7 (C)**).

Five parallel fabricated electrodes were examined the resulting electrochemical sensor's repeatability. The newly constructed electrochemical sensor showed remarkable repeatability, with a 92–95% recovery rate. (**Fig.5.7 (D)**)

The biosensor's interference test was carried out by exposing the XOs/g-$C_3N_4$@PoPD-T1/ITO electrode to a range of interfering analytes, 10 folds greater in concentration than Xn, including ascorbic acid, urea, uric acid, sodium benzoate, and glucose. Every analyte was shown to have a distinct current response, demonstrating the biosensor's selectivity for Xn detection **(Fig.5.7 (E)).** Additionally, a specificity test was performed to confirm that, Xn maintained its specificity even when mixed with interfering analytes.

In this work we have synthesized three stable ternary g-$C_3N_4$@PoPD-$TiO_2$ nanocomposites with (1%, 2%, and 3% of $TiO_2$ content) using a simple oxidative polymerization method. Various characterization

## 5.3. Conclusion

Techniques validate the successful formation of all ratios of g-$C_3N_4$@PoPD-$TiO_2$. An improved electron transfer value **(0.9131)** of g-$C_3N_4$@PoPD-$TiO_2$ with 1% $TiO_2$ makes it a promising electrode for biosensing studies. With a **0.1pM** (n = 3) detection limit, the fabricated electrode successfully detected Xn in real fish samples. The designed biosensing electrode has a sensitivity of (**7575.09 mA $\mu M^{-1}$ cm$^{-2}$**) and a very low detection range **(1pM-1µM),** acceptable stability **(5 weeks),** reproducibility **(92-95%),** and anti-interference characteristic. As a result, a biosensor based on g-$C_3N_4$@PoPD-$TiO_2$ nanocomposite with 1% $TiO_2$ was shown to be an effective platform for Xn monitoring.

# References

1.  Wang, Z., F. Liao, S. Yang, and T. Guo, *A Novel Route Synthesis of Poly(ortho-phenylenediamine) Fluffy Microspheres Self-assembled from Nanospheres.* Fibers and Polymers, 2011. **12**.

2.  Rashidizadeh, A., H. Ghafuri, H.R.E. Zand, and N. Goodarzi, *Graphitic Carbon Nitride Nanosheets Covalently Functionalized with Biocompatible Vitamin B1: Synthesis, Characterization, and Its Superior Performance for Synthesis of Quinoxalines.* ACS Omega, 2019. **4**(7): p. 12544-12554.

3.  Fahimirad, B., A. Asghari, and M. Rajabi, *Magnetic graphitic carbon nitride nanoparticles covalently modif ied with an ethylenediamine for dispersive solid-phase extraction of lead(II) and cadmium(II) prior to their quantitation by FAAS.* Microchimica Acta, 2017. **184**.

4.  Elshafie, M., S.A. Younis, P.Serp, and E.A.M Gad, *Preparation characterization and non-isothermal decomposition kinetics of different carbon nitride sheets.* Egyptian Journal of Petroleum, 2019. **29**.

5.  Chen, X., L. Liu, Y. Zhao, J. Zhang, D. Li, B. Hu, and X. Hai, *A Novel Metal-Free Polymer-Based POPD/g-C3N4 Photocatalyst with Enhanced Charge Carrier Separation for the Degradation of Tetracycline Hydrochloride.* 2017. **2**(29): p. 9256-9260.

6.  Laviron, E., *General expression of the linear potential sweep voltammogram in the case of diffusionless electrochemical systems.* Journal of Electroanalytical Chemistry and Interfacial Electrochemistry, 1979. **101**(1): p. 19-28.

7.  Elgrishi, N., K.J. Rountree, B.D. McCarthy, E.S. Rountree, T.T. Eisenhart, and J.L. Dempsey, *A Practical Beginner's Guide to Cyclic Voltammetry.* Journal of Chemical Education, 2018. **95**(2): p. 197-206.

8.  Thakur, D., C.M. Pandey, and D. Kumar, *Highly Sensitive Enzymatic Biosensor Based on Polyaniline-Wrapped Titanium Dioxide Nanohybrid for Fish Freshness Detection.* Applied Biochemistry and Biotechnology, 2022. **194**.

# CHAPTER 6

# SUMMARY AND PROSPECTS

## 6.1. Summary

In this thesis, several efforts have been made to fabricate an electrochemical fish freshness biosensor using XOs immobilized on CPs modified nanomaterials for quantitative estimation of Xn. The synthesis, characterization, and application of CP-based nanocomposites in fabricating efficient electrochemical biosensors for sensitive and specific detection Xn have been discussed. CP-modified nanomaterials show excellent physiochemical and electrical properties, cost-effectiveness and efficient electron transfer ability, offering a direct electrical readout for detecting biological analytes with high sensitivity and selectivity. They provide better structural and functional properties such as a high aspect ratio, enhanced mechanical strength, and electrical properties.

For the fabrication of biosensors, a thin layer of CP and its nanocomposite has been electrophoretically deposited onto the ITO electrode to offer a homogeneous, inexpensive, uniformly deposited, and controllable thickness film. The novel composite has been adopted to fabricate the biosensor with improved performance for detecting fish freshness in buffer and real samples. The present study revealed the electrical, structural, morphological, compositional, and electrochemical characteristics of conducting polymers, their nanocomposites with $TiO_2$, and their potential in biosensing applications. Fish freshness indication has been detected using a highly sensitive label-free electrochemical biosensor. The nanocomposite, which exhibits outstanding electrochemical characteristics, selectivity, and functions as a

suitable sensing layer, was created using a sustainable method.

**Chapter 3** describes the fabrication of an electrochemical enzymatic biosensor for Xn detection using PANI@TiO$_2$ nanohybrid. The synthesized nanostructured PANI@TiO$_2$ nanohybrid proved to be an efficient conducting platform for biosensing due to its redox behavior and the ability to mediate the reactive site and electrode surface via biomolecule. The improved electron transfer kinetics has been shown with an electron-transfer coefficient (0.9040) and a diffusion coefficient (9.11 x 10$^{-11}$ cm$^2$ s$^{-1}$). Further, this fabricated biosensor results in high sensitivity (0.415 µA M$^{-1}$ with R$^2$ = 0.9942) and low detection limit **(0.1µM)** against **(0.001-1 mM)** concentration range. The biosensor's functionality has been tested with a real sample taken from Rohu fish, and the results confirm that it can detect Xn in fish meat.

In **Chapter 4,** stable binary PoPD@g-C$_3$N$_4$ nanocomposite has been synthesized via a simple oxidative polymerization technique has been reported. An increase in electron transfer values (0.9105) for PoPD@g-C$_3$N$_4$ electrodes compared to bare PoPD and g-C$_3$N$_4$ makes it a promising material for immobilizing XOs. The fabricated XOs/PoPD@g-C$_3$N$_4$/ITO electrode successfully detected Xn **(0.001-1 µM)** in real fish samples with a detection limit of **1 nM** (S/N = 3). In addition, the developed biosensing electrode offers suitable sensitivity (5.798 µAM$^{-1}$ with R$^2$ = 0.9217 ), low detection limit (0.001 nM), acceptable stability (4 weeks), and reproducibility (RSD = 5.9 % ). Consequently, PoPD@g-C$_3$N$_4$ nanocomposite-based biosensor proves to be a viable platform for Xn monitoring.

Efforts also have been made to develop an electrochemical biosensor -based on g-C$_3$N$_4$@PoPD-TiO$_2$ nanocomposite and the results are presented in **Chapter 5**.

Different ratios of $TiO_2$ nanoparticles have been assessed to synthesize the g-$C_3N_4$@PoPD-$TiO_2$ nanocomposite. To create an incredibly sensitive electrochemical immunosensor to detect Xn in fish meat, the g-$C_3N_4$@PoPD-$TiO_2$ nanocomposite was electrophoretically deposited onto an ITO-coated glass substrate. Electrochemical studies reveal that depositing a 1% $TiO_2$ content g-$C_3N_4$@PoPD-$TiO_2$ nanocomposite onto an ITO electrode results in a comparatively greater surface area and enhanced electrochemical characteristics **(α = 0.9131).** With a detection limit of **0.1 pM** (S/N=3), the electrode's biosensing response exhibits linearity from 1pM to 1μM. The biosensor was 90–95% repeatable and stable for 5 weeks and it has been successfully validated for the measurement of Xn in real fish samples.

**Table 6.1:** Comparison of the different sensing parameters of the fabricated biosensors

| Matrix | Linear range | LOD | Charge transfer constant | Active surface area | Sensitivity | Shelf Life (weeks) |
|---|---|---|---|---|---|---|
| PANI@$TiO_2$/ITO | 1 – 100 μM | 0.1μM | 0.9010 | 0.24 | 0.415μA | 5 |
| PoPD@g-$C_3N_4$/ITO | 0.001-1μM | 1 nM | 0.9105 | 0.997 | 5.798μA | 4 |
| g-$C_3N_4$@PoPD-$TiO_2$/ITO | 1pM-1μM | 0.1pM | 0.9131 | 0.999 | 7.575μA | 5 |

The different biosensing parameters of all the fabricated biosensors are compared, specifically for Xn detection and it was observed that the g-$C_3N_4$@PoPD-$TiO_2$/ITO (1% $TiO_2$) based biosensor shows an excellent response to Xn with a low limit of detection **(0.1 pM)** and detects the presence of Xn in fish meat samples. The created biosensing electrode also has a very low detection range **(1pM-1μM),** acceptable stability **(5 weeks),** reproducibility **(90-95%),** and anti-interference characteristic.

Doubtlessly, the proposed g-C$_3$N$_4$@PoPD-TiO$_2$/ITO biosensor can be a reliable analytical tool for detecting Xn in commercial fish and meat samples.

## 6.2. Future Scope

Enhancing the sensitivity and selectivity of biosensors based on conducting polymers is likely to be a research priority. This could involve creating new conducting polymers with specific components for recognition or altering the surfaces of the polymer to improve their ability to interact with the target molecules. Future biosensors may incorporate several conducting polymers with various recognizing capabilities. This would make it possible to simultaneously detect several target analytes, making these sensors useful in complex sample analysis. Conducting polymer-based sensors may undergo additional development for point-of-care diagnostics, just like other forms of biosensors. Healthcare workers may be able to make quick judgments thanks to these systems' quick response times, simplicity of use, and potential interaction with mobile equipment. Flexible and wearable devices could incorporate conducting polymer-based biosensors, enabling continuous real-time monitoring of biomarkers. These gadgets might have uses in sports, healthcare, and wellness. Conducting polymer-based biosensors could join connected networks with the Internet of Things (IoT) growth and transmit real-time data for analysis and decision-making. Future developments in biosensor technology may concentrate on increasing sensitivity and selectivity and the ability to detect numerous fish freshness biomarkers with electrochemistry. Using biosensors based on nanotechnology to assess the freshness of meat is proving itself superior to conventional techniques. Due to their extraordinary sensitivity and accuracy, these sensors can distinguish between

different purine derivatives and detect incredibly small amounts of contaminants. The monitoring of meat products can be improved with greater efficiency because of their quick response, which results in only a few minutes or seconds. These portable, user-friendly biosensors, which make use of nanotechnology, are especially suited for real-time assessments in contexts like food processing plants.

Although the addition of these sensors has the potential to change how we evaluate the freshness of meat completely, it is crucial to be aware of the challenges or restrictions that might exist. The expense of acquiring and maintaining these sensors, which may be more than that of conventional methods, is a challenge. The potential consequences on employment must also be taken into consideration, since the widespread deployment of these sensors might conceivably result in job displacement within specific industries. In essence, global advances in meat freshness detection using biosensors based on nanotechnology are imminent.

# PUBLICATIONS

1. **Deeksha Thakur**, C.M. Pandey, and D. Kumar, "Highly Sensitive Enzymatic Biosensor Based on Polyaniline-Wrapped Titanium Dioxide Nanohybrid for Fish Freshness Detection", *Applied Biochemistry and Biotechnology*, 2022. 194 (8): p. 3765-3778. Impact factor: 3.1

2. **Deeksha Thakur**, C.M. Pandey, and D. Kumar, "Graphitic Carbon Nitride-Wrapped Metal-free PoPD-Based Biosensor for Xanthine Detection" , *ACS Omega*, 2023. 8(2): p. 2328-2336. Impact Factor: 4.1

3. Geetu Paul, Sakshi Verma, Owais Jalil, **Deeksha Thakur**, C.M. Pandey, D. Kumar, "PEDOT:PSS-grafted graphene oxide-titanium dioxide nanohybrid-based conducting paper for glucose detection", *Journal of Polymers for Advanced Technologies,* 2021. 32(4): p. 1774-1782. Impact Factor: 3.3

4. Palak Garg, **Deeksha Thakur,** Sakshi Verma, Owais Jalil, C.M. Pandey, D. Kumar, "Biosynthesized rGO@ZnO-based ultrasensitive electrochemical immunosensor for bovine serum albumin detection", *Journal of Applied Electrochemistry*, 2023. p. 1572-8838. Impact Factor: 2.9

5. Sakshi Verma, **Deeksha Thakur**, C.M. Pandey, D. Kumar, "Recent Prospects of Carbonaceous Nanomaterials-Based Laccase Biosensor for Electrochemical Detection of Phenolic Compounds ", *Biosensors*, 2023. 13(3): p. 2079-6374. Impact Factor: 6.6

6.  Prateek Sharma, **Deeksha Thakur**, D. Kumar "Novel Enzymatic Biosensor Utilizing $MoS_2/MoO_3$ Nanohybrid for Electrochemical Detection of Xanthine in Fish Meat ", ***ACS Omega***, 2023. 8(35): p. 31962–31971. Impact Factor: **4.1**

7.  Prateek Sharma, **Deeksha Thakur**, D. Kumar**, Om Prakash Yadav** "Unveiling Xanthine Presence in Rohu Fish Using $Ag^+$ -Doped $MoS_2$ Nanosheets Through Electrochemical Analysis", ***Applied Biochemistry and Biotechnology***, 2024. Impact factor: 3.1

8.  Contributed in a **Book Chapter: Quantum dots-based nanocomposites** as **biosensor** in a book entitled "*Quantum dots-based nanocomposites : Design, Fabrication and Emerging Applications*" published by Springer.

9.  **Deeksha Thakur**, C.M. Pandey, D. Kumar", $TiO_2$ doped $g\text{-}C_3N_4$@PoPD nanohybrid based biosensor for Xanthine detection. **(To be submitted)**

10. **Deeksha Thakur**, Sakshi Verma, C.M. Pandey, D. Kumar, " Mini Review : Conducting polymer-based Xanthine detection". **(Manuscript under preparation)**

# CONFERENCES

1. Presented Poster at 2$^{nd}$ International Conference on "**Recent Trends in Environment Sustainable Development**" held on 17$^{th}$ and 19$^{th}$ October 2019 at Vivekananda Global University, Jaipur, India on " Electrochemical Detection of Xanthine Based on Polyaniline-TiO$_2$ Nanocomposite" .

2. Attended a Virtual International Conference on "**Advanced Materials Behaviour & Characterization**" held from 18$^{th}$ to 23$^{rd}$ July 2020 at Mattest Research Academy, Chennai, India.

3. Presented Poster at Virtual International Conference on "**Surface Chemistry**" held on 27$^{th}$ and 28$^{th}$ August 2020 at Annamalai University, Annamalai Nagar, Tamilnadu, India on "Electrochemical Detection of Xanthine Based on Polyaniline-TiO$_2$ Nanocomposite".

4. Attended a Virtual International Conference on "**Innovations in Biotechnology and Life Sciences**" held from 18$^{th}$ to 20$^{th}$ Dec 2020 at Delhi Technological University , Delhi, India.

5. Attended a One Day Virtual Workshop on "**Accelerators/Incubation – Opportunities for Students & Faculties- Early-Stage Entrepreneurs**" held on 19$^{th}$ June 2021 at the Department of Applied Chemistry, Delhi Technological University , Delhi, India .

6. Attended a One Day National Seminar on "**Recent Advancement in Semiconductor Devices and Materials**" RASDM-2023 held in the Department

of Applied Physics, Delhi Technological University , Delhi, India on 30th Jan 2023.

7.  Attended a One Day National Seminar on " **Implementation of NEP-2020 in special reference to Innovation & Entrepreneurship**" held in the Department of Applied Physics, Delhi Technological University , Delhi, India on 24th Feb 2023.

8.  Attended an International Conference on "**Chemical & Allied Science and their Applications**" organized by the Department of Applied Chemistry, Delhi Technological University , Delhi, India on 20th Jan 2023 .

9.  Attended a  One Day National Seminar "I**mplementation of NEP-2020 in special reference to innovation & entrepreneurship**" held on 24th Feb, 2023 organized by the Applied Physics Department, Delhi Technological University , Delhi, India.

**Dr. Deeksha**
**9873488716**
thakur.diksha2@gmail.com
deeksha_2k18phdac01@dtu.ac.in
https://scholar.google.com/citations?hl=en&user=nadGkF4AAAAJ

PhD in Chemistry from Department of Applied Chemistry, Delhi Technological University. Research interest includes Polymer synthesis, Composites and blends, Nanocomposites synthesis, Sensors and Conducting Polymer based Biosensors with expertise in the synthesis, design, formulation and characterization of materials properties, as well as coordinating testing and development. Adapt to developing new applications and products, generating intellectual properties and providing technical solutions. Skilled in instrument monitoring and analytical method performance.

## EDUCATION

- 2018- 2024, Philosophy of Doctorate (Ph.D.) Applied Chemistry , DTU, Delhi

- 2014-2016, Master of science (M.Sc.) Polymer science , MLSU ,Udaipur, India, Percentage-81/100

- 2011-2014, Bachelor of science (B.Sc. Hons.) Polymer science, DU, Delhi, India, Percentage-69/100

- 2010-2011, Higher Secondary School, (Science & Math) CBSE, KV JNU, Delhi, India,Percentage-74/100

- 2009-2010, Secondary School, CBSE, KV JNU , Delhi, India, Percentage-72/100

## PROFESSIONAL EXPERIENCE

- 16th Oct 23 – Present, as Assistant Professor in KCCITM , Greater Noida, U.P. (Applied Sciences).

- 12th May – 31 July 2023 as Assistant Professor in HMRITM , Alipur, New Delhi (Applied Sciences).

- 5th Nov 17 – 5th Jan 2018  as executive in just polymers solutions at Rajender Nagar, New Delhi.

- 12th April - July 2017 as faculty of material science in career avenue at Jia Sarai, New Delhi.

## RESEARCH EXPERIENCE

- Citation -66 ; h-index- 4 ; i10-index – 3
- Published 7 research paper and 1 Book chapter

## INSTRUMENTAL SKILLS

- Potentiostat/galvanostat: Cyclic Voltammetry, square wave Voltammetry, Chronoamperometry; Electrochemical impedance Spectroscopy, X-ray diffractometer, Fourier transform infrared and UV-visible spectrophotometer

## ACHIEVEMENTS & AWARDS

- Gold Medallist in M.Sc. MLSU , UDAIPUR, INDIA – 2017.
- Awarded as DST INSPIRE Fellowship -2018.
- Awarded with Research Excellence award at DTU in 2022, 2023 and 2024.